EXTENSIONS OF INDEPENDENT COMPONENT ANALYSIS TO ANALYZE FUNCTIONAL CONNECTIVITY AND NEURAL SPIKE TRAIN DATA

Kevin M. Donovan

A dissertation submitted to the faculty of the University of North Carolina at Chapel Hill in partial fulfillment of the requirements for the degree of Doctor of Philosophy in the Department of Biostatistics in the Gillings School of Global Public Health.

Chapel Hill
2021

Approved by:

Young K. Truong

Yun Li

Michael G. Hudgens

Mark Shen

Jose Rodriguez-Romaguera

ABSTRACT

Kevin M. Donovan: Extensions of Independent Component Analysis to Analyze Functional Connectivity and Neural Spike Train Data
(Under the direction of Young K. Truong)

In the first chapter, we purpose a three matrix independent components analysis (ICA) model which distinctly identifies within-network connectivity, between-network connectivity, and the dynamic activation of the networks over time. This model limits the use of parametric model assumptions and avoids the use of bivariate correlations to measure connectivity, allowing more complex networks to be identified. The estimation process is supervised by specifying frequency characteristics that are of interest in the extracted components, making this model suitable for task-based designs where the task sequence is characterized by a harmonic process (e.g. block designs). We show in simulation studies how our method can extract all three matrices accurately, even when outliers are present (which is often the case with imaging data) while more conventional ICA models fail to do so. The proposed model is then used to analyze connectivity using data from a task-based experiment used to simulate motor response (hand and foot movement) from the a single subject in the Midnight Scan Club dataset.

In the second chapter, we develop an extension to this connectivity model which is unsupervised, removing the need to specify temporal characteristics of interest a priori. This is done by adapting a regularized singular value decomposition method which results in sparse spatial components and smoothed temporal components using the discrete wavelet transform. We establish the extension's ability to accurately estimate the three latent matrices which compose the data, even when there is substantial spatial noise and when the temporal components are harmonic processes with changing frequencies over time. The proposed model is then used to analyze

connectivity using data from a resting state experiment, consisting of imaging data on a single subject from the ABIDE dataset.

In the third chapter, we develop an extension to ICA which models integer-valued components, estimated using a nonparametric, spline-based model of the conditional intensity function. This conditional intensity function estimate is then used to predict the latent sources and then estimate the mixing matrix using maximum likelihood. We examine the method's performance through simulation studies and compare the method to conventional ICA models which are not designed for integer-valued or autocorrelated latent sources.

ACKNOWLEDGEMENTS

I would like to gratefully acknowledge my advisor, Young Troung, for his guidance and support along with my doctoral committee, Michael Hudgens, Yun Li, Mark Shen, and Jose Rodriguez-Romaguera. I would also like to thank my colleagues at the Carolina Institute for Developmental Disabilities, from which I learned a tremendous amount and received invaluable support throughout much of my graduate career. Lastly, I would like to thank my friends and family for their continued support across my educational career. This work was supported by NIH Grant 5R01HD055741-14.

TABLE OF CONTENTS

LIST OF FIGURES

LIST OF ABBREVIATIONS

ICA	Independent Component Analysis
fMRI	Functional Magnetic Resonance imaging
BOLD	Blood oxygenation-level-dependent
EEG	Electroencephalography
MEG	Magnetoencephalography
SNR	Signal to noise
PCA	Principal component analysis
SVD	Singular Value Decomposition
sSVD	Supervised Singular Value Decomposition
cICA	Colored Independent Component Analysis
AR	Autoregressive
scICA	Spatial Colored Independent Component Analysis
sSVD-cICA	Proposed task-based connectivity model
DFT	Discrete Fourier Transform
DWT	Discrete Wavelet Transform
PSVD	Penalized Singular Value Decomposition
PSVD-cICA	Proposed wavelet-based connectivity model
NMF	Non-negative Matrix Factorization
CNMF	Constrained Non-negative Matrix Factorization
HEFT	Hazard Estimation with Flexible Tails

CHAPTER 1: ANALYZING FUNCTION CONNECTIVITY FROM TASK-BASED STUDIES USING INDEPENDENT COMPONENT ANALYSIS

1.1 Introduction

A main area of current research in neuroscience is around the concept of *functional connectivity*. Functional connectivity refers to the temporal correlations between neurophysiological events [Friston, 1994]. That is, two brain regions are connected functionally if their neurological activity are associated with one another in relation to a physiological event. Functional magnetic resonance imaging (fMRI) indirectly measures neurological activity based on changes in blood oxygenation over time at each location of the brain; these changes are referred to as the blood-oxygenation-level-dependent (BOLD) signal [Rogers et al., 2007]. This allows fMRI to indirectly measure activity of the brain over the duration of an experiment with high spatial specificity. When combined with the timing of regional BOLD activity in the brain and the timing of the physiological activity/study task, the data can be used to identify functionally-connected regions.

Task-based experimental designs allow the researcher to stimulate specific physiological events of interest during specific time windows. This design may allow the association between brain activity and the corresponding behavioral outcome to be more clearly identified, facilitating the interpretation of the connectivity results [Buckner et al., 2013]. From this design, it may be of interest to estimate changes in connectivity as the task changes over the duration of the experiment, referred to as dynamic functional connectivity [Hutchison et al., 2013]. The temporal resolution of fMRI data acquisition facilitates the analysis of these dynamic features of the brain. Doing so requires methodology which can extract this connectivity signal from the noisy fMRI data. We present a model to estimate these connectivity features from spatio-temporal data,

when a priori information is known on the temporal patterns of interest. This information, for example based on the task sequence, can then be leveraged to more precisely estimate connectivity compared to standard methods. Section 1.2 provides a literature review on pre-processing and connectivity methods for neural imaging data analysis, Section 1.3 describes the proposed method for analyzing task-based connectivity, Section 1.5 provides results from applying the proposed method to actual task-based fMRI data, and Section 1.6 concluded with limitations and discussion.

1.2 Literature Review

1.2.1 Neural Imaging Analysis and Pre-Processing

In general, neuroimaging data is measured at discrete points in time and physical space. Imaging can be done in various modalities, with common non-invasive ones being magnetic resonance imaging (MRI) and electroencephalography (EEG). Each has its own strengths and weaknesses which need to be considered in tandem with the scientific questions of interest, experimental design, and analytic methods used [He et al., 2011]. This is particularly important for functional connectivity, as the spatial nature of the concept requires sufficient spatial resolution while dynamic connectivity requires sufficient temporal resolution to accurately identify the neurological dynamics of interest. Functional MRI is often used for these purposes due to its very high spatial resolution and adequate (though not the best) temporal resolution [He et al., 2011].

Data acquired from these imaging modalities contain a combination of information which is relevant to the scientific question of interest (*signal*) and additional information which is not relevant (*noise*). Thus, maximizing the ratio of signal to noise (SNR) is important, generally defined as the ratio of the mean signal over time and the standard deviation of noise over time [Welvaert and Rosseel, 2013]. Fluctuations in the signal over the course of an experiment can be small in magnitude with noise being a significant portion of the data [Rogers et al., 2007]. As a result, maximizing the SNR is critical in terms of determining these fluctuations from the observed data [Parrish et al., 2000]. This is further compounded by the indirect nature of imaging

modalities such as fMRI and EEG in measuring underlying brain activity. While spatially and temporally isolated neural activity is of scientific interest, fMRI and EEG are not able to provide direct measurements. For fMRI, while the BOLD signal is thought to be correlated with neural activity, it is not a perfect surrogate given the time lag between the BOLD signal and underlying activity [He et al., 2011]. For EEG, neural activity can be lost before it reaches the sensors due to physiological complications such as volume conduction, as well as crosstalk (same activity being identified by multuple sensors) [He et al., 2011].

SNR is related to the mechanical properties of the imaging modality being used, the study design, and the statistical analysis [Petersson et al., 1999]. As a result, it can be manipulated to create more informative analyses. This ratio is complicated by the multi-dimensional property of neuroimaging data in the spatial and temporal domains, which each domain having its own amount of signal and noise [Petersson et al., 1999]. Ambiguities also exist in terms of defining this ratio due to the many modalites available and their very heterogeneous nature. For example, defining SNR for fMRI data is still an ongoing discussion in the literature [Welvaert and Rosseel, 2013].

Various statistical approaches have been used to address the high degree of noise in imaging data. Many of these approaches are referred to as a part of the pre-processing stage, during which the data is prepared for eventual analysis. Different approaches have been developed to maximize SNR temporally and spatially. Some sources of noise have a well understood frequency range (generally very high frequency sources are noise), which is used in combination with bandpass filtering to eliminate these sources from the observed data [Friston et al., 1996, Weissenbacher et al., 2009, Power et al., 2012, Satterthwaite et al., 2013]. Linear regression using covariates which reflect these noise sources of interest to remove them from the signal is also commonly used [Friston et al., 1996, Johnstone et al., 2006]. Spatial filtering is also used, specifically kernel smoothing (Gaussian kernal for example) to reduce noise between locations in close proximity of each other to more accurately reflect a continuous spatial signal in the data [Friston et al., 1996, Van Veen et al., 1997, He et al., 2011]. Kernel methods smooth the observed data by using

averages of "nearby" points, which the weights and distances of the points determined by the chosen kernel function [Triantafyllou et al., 2006].

Dimension reduction methods using matrix factorization have also been used for pre-processing of imaging data due to the high dimensional nature of neural imaging data. Principal component analysis (PCA) is often used as a pre-processing step with fMRI data due to the high spatial and temporal dimensions of the data, making inference computationally unstable and noisy [LaConte et al., 2003, Xie et al., 2009, Churchill et al., 2012, Smith et al., 2014]. PCA allows the data to be transformed into a reduced set of components which contain most of the signal in the data, based on the estimated covariance matrix or another square matrix obtained using data decomposition methods such as singular value decomposition (SVD) [LaConte et al., 2003]. However, PCA requires the number of components in the set to be selected manually such that the noise-influenced components are removed. This can lead to portions of the signal being removed as well or large amounts of noise being left in the data [LaConte et al., 2003]. The dimension-reduced data also may be difficult to interpret compared to the original set of variables.

Along with traditional PCA, various forms of supervised factorization methods have been developed, which allow information about hypothesized components of interest to be included in the decomposition [Bai et al., 2008, Barshan et al., 2011, Li et al., 2016]. In theory, this should allow a more accurate identification of these components in the data, improving the signal detection in the dimension-reduced set. The information provided could result in more interpretable components, based on temporal frequencies of interest, experiment design and other covariates. This is particularly of interest with neural imaging data due to the known attributes of many forms of neurological activity, as well as the temporal nature of experimental design [Bai et al., 2008]. Extensions to these methods have also been developed which use more data-driven and less supervised approaches Zhang et al. [2013], Hong and Lian [2013].

Independent component analysis (ICA) [Churchill et al., 2012, Warnick et al., 2018] is also used for dimension reduction. ICA has been used to identify common noise components such as eye blinking by examining the frequencies present in the predicted temporal components (tempo-

ral ICA) or the spatial location of activity of the predicted components (spatial ICA) [Xue et al., 2006, Bai et al., 2008, Pruim et al., 2015]. Similar to PCA, the purpose of using ICA for dimension reduction is to identify noise components in the data as latent variables and then remove these isolated components.

While both PCA and ICA are matrix factorization methods, PCA tries to find an orthogonal transformation of a set of components with maximum variance, with components ranked in order of variability. ICA tries to find a linear transformation of a set of components which are independent and non-Gaussian. ICA and PCA (or SVD) are often used in tandem due to the high dimension of imaging data. PCA/SVD is used first as a dimension reduction tool and then ICA is used as a tool to identify latent groups temporal or spatially [Hyvärinen and Oja, 2000, Romero, 2011, Chawla, 2011].

When applying ICA on imaging data, a common pre-processing method used is whitening. Whitening entails a linear transformation of the observed data resulting in each variable having zero correlation with the others (data is ”white”). This results in an orthogonal mixing matrix in the ICA model, improving the computational stability of the estimation process [Hyvärinen and Oja, 2000].

1.2.2 Functional Connectivity

Functional connectivity is often measured by the correlations between a set of spatial locations in the brain across time, with these correlations sometimes conceptualized using a graph theory approach [Wang et al., 2010, Joel et al., 2011]. Locations are represent by vertices on the graph which are connected by edges; these edges represent functional connectivity. Weights are attached to these edges which represent the degree of connectivity, with various methods used to define and then estimate these weights. Some measure of correlation (Pearson for example) is often used for continuous weights, with a binary measure sometimes used instead by thresholding continuous measures (0 implies no connectivity, 1 implies connectivity) [Rubinov and Sporns, 2010, Kaiser, 2011].

The spatial locations are often referred to as *nodes*. The locations from a fMRI scan are comprised of individual voxels, single units of measure representing equal-size cubes. Each voxel represents a fine-grain measure of activity in three-dimensional space. Thus, fMRI data is comprised of a time series of BOLD signals for each voxel. With fMRI data, the nodes are often either defined at the voxel-level directly or by decomposing the voxel-level data into a smaller set of components due to the high spatial dimension [van den Heuvel et al., 2008, van den Heuvel and Pol, 2010]. These components are often referred to as regions of interest (ROIs) [Rogers et al., 2007]. The set of nodes can be selected a priori, using a data-driven approach, or a combination of both [Joel et al., 2011, Marrelec and Fransson, 2011, Sohn et al., 2015]. These nodes can also be constructed on a whole sample level, on a more individualized level per subject, or based on some grouping variable (diagnosis for example) [Abou Elseoud et al., 2011, Sohn et al., 2015]. After deciding on a set of nodes, their correlation (or some other measure of association) across time can then be calculated from their observed time series [Fox and Raichle, 2007]. This is sometimes referred to as a *seed-based* approach [Joel et al., 2011].

Using a seed-based approach has a number of limitations. Since the connectivity is only assessed at selected ROIs and bivariate correlations are used for estimation, it is difficult to assess more complex connectivity structures. This can result in connectivity patterns within the brain going undetected in the data analysis [Joel et al., 2011]. The method for node selection can also lead to shortcomings in the analysis. If ROIs are selected a priori, connectivity between regions whose composition differs from those selected may be undetectable [van den Heuvel and Pol, 2010]. Specifying the same set of nodes for population or group-level data does not account for individual variation in regional functional connectivity. Unless the voxels are used as the nodes, without a data-driven approach these individual-level differences are difficult to take into account in the analysis [Sohn et al., 2015]. However, due to the high spatial dimension of fMRI data, using voxels-level analyses makes identifying and testing macro-level connectivity difficult due to the large number of comparisons (diminishing power) and large variance in neural activity at the voxel-level.

Parametric modeling techniques such as structural equation modeling (SEM) can be used to reflect more complex relationships between voxels beyond bivariate correlations, but these techniques suffer from possible model misspecification [Mclntosh and Gonzalez-Lima, 1994, Rogers et al., 2007]. Misspecification is particularly concerning in this context due to the high dimensional, complex nature of connectivity as well as high amount of noise present in imaging data. This can result in a large number of model parameters to estimate unless the dimension of the data is reduced. As a result, a set of ROIs is usually created to serve as potential locations of connectivity, which may cause connectivity patterns present in a different set of ROIs to go undetected [van den Heuvel and Pol, 2010, Guàrdia-Olmos et al., 2018].

Dynamic causal modeling (DCM) is another parametric modeling approach used to analyze functional connectivity [Friston et al., 2003, Ramnani et al., 2004]. DCM is similar to SEM, in that it is a parametric modeling of the observed data as a function of latent constructs. DCM represents the underlying brain activity as latent constructs, with each construct representing a specific spatial region. It allows interactions in activity between these regions to be modeled dynamically over time, compared to traditional SEM where they are modeled statically. More specifically, for l brain regions with neural activity denoted by $z = (z_1, \ldots, z_l)$, future neural activity is modeled using $\dot{z} = F(z, u, \theta)$ where $F(.)$ is a non-linear function and u are inputs which exert changes on the neural activity (ex. experiment stimulus). Then connectivity is generally represented by the change in the system when neural activity z changes, that is by $A = \frac{\partial F}{\partial z}$. DCM is highly parametric with a large number of functions and parameters which require defining and estimating respectively. Bayesian methods are used to conduct inference on parameter θ using the computed posterior distribution, adding the complication of choosing an appropriate prior [Friston et al., 2003].

Granger causality (GC) is another method used to analyze functional connectivity by leveraging the temporal nature of imaging data. Similar to SEM and DMC, GC is used to assess directional relationships of connectivity by comparing the timing of activity across the brain regions during the experiment. GC is based on the idea that causes temporally precede their effects. GC

is commonly assessed using autoregressive models with the ROI/voxel-specific time series, with the location's previous activity as well as previous activity from other locations as covariates [Granger, 1969, Seth et al., 2015]. Thus, GC defines connectivity by one location's ability to predict activity in other at a future time. Generalizations have since been developed, including nonparametric extensions [Seth et al., 2015]. However, due to the frequent use of parametric modeling, GC is subject to model misspecficiation, potentially introducing bias. Furthermore, this definition of connectivity simply as a relationship manifesting in the prediction of the observed data does not reflect the indirect relationship between imaging data and actual neural activity. As a result, it does not directly model the physiological properties of connectivity (compared to DCM for example), which is generally of most scientific interest [Seth et al., 2015]. This is particularly concerning in fMRI data where there is a known temporal lag between the underlying neural activity and corresponding observed BOLD signal.

Common data-driven approaches include PCA [Rogers et al., 2007, Zhong et al., 2009, Leonardi et al., 2013], clustering methods [Deen et al., 2010, Liu et al., 2012], and ICA [van de Ven et al., 2004, Warnick et al., 2018]. Methods such as k-means and hierarchical clustering have been used to group regional associations in neural activity measured using bivariate Pearson correlation across time, and linear modeling of each region's time series as the outcome and the other regions as the covariates. With linear modeling, the corresponding regression parameter estimates can then be analyzed using a clustering algorithm [Deen et al., 2010]. Hierarchical clustering begins by regarding each region as a separate cluster. A distance metric is then computed for each pair of regions (for example Pearson correlation). The pair with the lowest distance is then clustered together, and the process repeats until one cluster is formed (the entire data). Intercluster (the distance between two clusters two pairs of regions belong to) is also calculated when they merge into new clusters. A final set of clusters is then selected based on a chosen metric [Liu et al., 2012].

ICA is a matrix factorization method also used to analyze functional connectivity. ICA models an observed data matrix $\boldsymbol{X}$ as a product of two matrices; one a matrix of weights (often de-

noted by $\boldsymbol{A}$, the *mixing matrix*) and the another a matrix containing the realizations of the latent variables as its rows (often denoted by $\boldsymbol{S}$) [Bordier et al., 2010]. That is, $\boldsymbol{X} = \boldsymbol{AS}$, modeling the observed data as a linear combination (mixing) of latent variable realizations. It is further assumed that these latent variables (and thus the rows of $\boldsymbol{S}$) are independent and non-normally distributed. These latent variables are thus multivariate with entries corresponding to levels of activation in the imaged locations (*spatial ICA*) or at the recorded time points (*temporal ICA*) depending on the dimension of $\boldsymbol{X}$. As a result, ICA is sometimes interpreted as a clustering method, with the latent variables serving as the clusters [Joel et al., 2011]. In spatial ICA, these variables are often interpreted as latent spatial networks in the brain, with the entries of S as the degree to which each spatial location contributes to the network. In temporal ICA, the latent variables represent networks in neural activity with respect to time.

Since the rows of $\boldsymbol{S}$ are considered independent, they are not useful for assessing functional connectivity through correlation-based analyses. As a result, estimated correlations from $\boldsymbol{A}$ between independent components are generally used instead [Allen et al., 2012, Marusak et al., 2017, Warnick et al., 2018]. However, $\boldsymbol{A}$ is considered a matrix of fixed constants to be estimated and not random quantities despite this use of correlation [Bordier et al., 2010]. Generally, this distinction has not been considered when using ICA to assess functional connectivity. In that sense, ICA provides a relatively simple and flexible model of connectivity while allowing non-linear relationships, with $\boldsymbol{S}$ representing within-network connectivity and $\boldsymbol{A}$ between-network connectivity. ICA is computationally stable with high-dimensional data and thus can be used to analyze neural activity at a high spatial resolution without requiring a large amount of a priori dimension reduction [Hyvärinen and Oja, 2000]. Thus, nodes at the voxel-level can be used directly, though some form of dimension reduction is still sometimes used (such as PCA) [Hyvärinen and Oja, 2000, Romero, 2011, Chawla, 2011]. Data-driven ROIs can be conceptualized from ICA based on the networks from the latent sources in $\boldsymbol{S}$ [Allen et al., 2012, Marusak et al., 2017, Warnick et al., 2018].

Beyond the risk of mis-specification with parametric approaches, the benefit of a latent variable method such as ICA is it's ability to reflect the indirect acquisition of neural activity by modalities such as MRI and EEG [Ramsey et al., 2010]. ICA models the observed data as a function of unobserved latent variables, which reflects how imaging modalities are a noisy, imperfect measurement of underlying neural activity in the brain [Beckmann and Smith, 2004]. This underlying neural activity can be thought of as a latent variable, as is common in measurement model theory [Bollen, 1989]. Thus, applying models which reflect the relationship between the observed measurement and physiological response (such as a hemodynamic reponse function in fMRI data) is not necessary to identify underlying neural activity, which is the target of scientific interest. This removes the need to apply parametric models which assume a structure for thsi relationship, which may be misspecified [Beckmann and Smith, 2004, Calhoun and Adali, 2006]. Furthermore, ICA (and similar clustering methods) is not limited to uncovering bivariate relationships like correlation is, relfecting the multivariate nature of connectivity [Smith et al., 2011].

While these methods have mostly been used for assessing static connectivity over time, functional connectivity which changes over time or in response to stimuli is also of interest. The traditional approaches to connectivity such as calculating ROI-specific correlations across time or assessing Granger Causality treat the node's response at each time point as a random sample from the same distribution. As a result, possible changes in connectivity across time cannot be defined or estimated. In response, methods have been developed to define and measure *dynamic functional connectivity* [Friston et al., 2003, Leonardi et al., 2013, Koush et al., 2013, Xu and Lindquist, 2015, Shakil et al., 2016, Warnick et al., 2018]. These methods partition the time scale of the data by grouping time points, and allows the connectivity structures between each group to differ while staying constant within each group of time points. This is an example of local stationarity [Dahlhaus, 2012].

When imaging data is acquired from a task-based experiment, dynamic connectivity can be assessed by estimating the difference in connectivity before and after task onset. DCM can be used in this way, although continuous changes across the entire time scale cannot be modeled

and analyzed as the input changing the neural activity is considered discrete [Friston et al., 2003, Koush et al., 2013, Shakil et al., 2016]. Many methods for analyzing dynamic connectivity on a continuous time scale use a sliding window approach in combination with procedures applied to static connectivity [Chang and Glover, 2010, Allen et al., 2012, Lindquist et al., 2014, Shakil et al., 2016]. Sliding-window correlation analysis entails creating a length of time to serve as the "window" followed by computing correlations for the voxel time-series within this window of time. This window is then continually shifted forward in time and the correlations are again computed until the end of the time series are reached. This method has a number of potential shortcomings and complications, including choosing the window length and using a binary method of weighting observations (all within have same weight, all outside do not contribute). Furthermore the use of windowing can result in abrupt changes in connectivity to go unseen [Lindquist et al., 2014]. Another framework partitions the time course into sets of intervals such that connectivity is static within these intervals but differs between them. This is commonly referred to as assuming *local stationarity* [Dahlhaus, 2012]. These partitions can be set a priori (for example based on the experimental design) or data driven. Connectivity can be then estimated within each interval using standard methods, and then compared between them using a chosen metric or modeling approach [Xu and Lindquist, 2015, Warnick et al., 2018].

Frequency-based analyses are also used to assess dynamic connectivity, particularly based on coherence [Sun et al., 2004, Chang and Glover, 2010, Srinivasan et al., 2007, Catarino et al., 2013, Euán et al., 2019]. Coherence is measure of correlation between two time series based on their frequencies instead of their observed realizations [Gardner, 1992]. It assesses which frequencies are associated between the two series. Various frequencies have been characterized in neural activity as being associated with specific physiological phenomenon. This makes coherence (and frequencies in general) an intuitive way of assessing connectivity [Buzsáki and Draguhn, 2004, Stam, 2000, Wu et al., 2008, Lee et al., 2013a]. These methods generally assess the frequency information in the observed data. However, due to the large amount of noise present in imaging data as well as the indirect measurement used by many modalities, this may

prevent the underlying physiological relationships from being revealed [Mclntosh and Gonzalez-Lima, 1994, Friston et al., 2003, Ramnani et al., 2004, Seth et al., 2015].

ICA has also been used to analyze dynamic connectivity [Kiviniemi et al., 2011, Chen et al., 2013, Allen et al., 2012, Marusak et al., 2017, Warnick et al., 2018]. Typically, this involves a sliding window approach using ICA instead of, or in combination with, correlation analyses [Kiviniemi et al., 2011, Chen et al., 2013, Allen et al., 2012, Marusak et al., 2017]. Warnick et al. [2018] developed a Bayesian method for applying ICA with a hidden Markov model to assess dynamic connectivity which does not require a sliding window approach. However, it has potential shortcomings such as the subjectivity of the chosen priors, and the extensive use of modeling assumptions through the priors and use of a hidden Markov model for the changing connectivity. Furthermore, they apply this Bayesian model not to the observed imaging data but to the ICA-determined ROIs, which were determined using an ICA fitting procedure which does not account for within-component correlation. The modeling and computational complexity is also quite high due to the large number of prior distributions required for the various model components, creating the risk of a large degree of model misspecification.

1.3 Proposed Methods

1.3.1 Stochastic Processes

A univariate stochastic process $S(t)$ is a random variable defined as a function of t (time for example), taking a single value at each t. Denote the multivariate stochastic process $S(t) = (S_1(t), \ldots, S_U(t))$ for $t = 0, \pm 1, \pm 2, \ldots$ where $S_j(t)$ is mean zero and has covariance function $c_{S_j S_j}(u) = \text{Cov}(S_j(t), S_j(u+t))$ for all t and $j = 1, \ldots, U$. That is, $S(t)$ is (weakly) stationary. Assuming $\sum_{u=-\infty}^{\infty} |c_{S_j S_k}(u)| < \infty$ for all $j, k = 1 \ldots, U$, the U by U spectral density matrix of $S(t)$ can be defined as

$$\boldsymbol{f_{SS}}(r) = [f_{S_j,S_k}(r)]_{j,k=1,\ldots,U}$$
$$\text{where } f_{S_j,S_k}(r) = \frac{1}{2\pi}\sum_{u=-\infty}^{\infty} c_{S_jS_k}(u)\text{exp}(-iru) \text{ for } r \in \mathbb{R}$$

where r denotes a frequency and i denotes the complex i. Both the marginal spectral densities of $S_j(t)$, (f_{S_j,S_j}) for $j = 1, \ldots, U$, and bivariate joint spectral densities of $S_j(t), S_k(t)$ (f_{S_j,S_k}) for $j \neq k$, are contained in $\boldsymbol{f_{SS}}(r)$. These describe the processes' realized values with respect to their frequencies, as well as how these realized frequencies are associated. This is separate from the usual densities which directly describe the occurrence of the proccesses' realized values.

Suppose T realizations are observed, denoted by $S(t)$ for $0, 1, \ldots, T-1$ and consider the set of frequencies denoted by $r_k = 2\pi k/T$ for $k = 0, \ldots, T-1$. The discrete Fourier transform (DFT) of $S(t)$ for $t = 0, \ldots, T-1$ is defined by

$$\boldsymbol{\phi}(r_k, S) = (\phi(r_k, S_1), \ldots, \phi(r_k, S_U))^T = \sum_{t=0}^{T-1} S(t)\text{exp}(-ir_kt)$$

with the raw multivariate periodogram defined by the squared modulus of the DFT, denoted by

$$\hat{\boldsymbol{f}}(r_k, S) = |\boldsymbol{\phi}(r_k, S)|^2 = \frac{1}{2\pi T}\boldsymbol{\phi}(r_k, S)[\boldsymbol{\phi}^*(r_k, S)]^T$$

is U by U where * denotes the complex conjugate. The periodogram serves as an estimate of the spectral density, though improved estimates have been developed such as the windowed periodogram [Brillinger, 2001].

The DFT can be used to derive a log likelihood with respect to the frequency domain for (weakly) stationary processes. Suppose $r_k \to \lambda_k$ for $1 \leq k \leq K$, with $-\infty < \lambda_k < \infty$, as $T \to \infty$. Then $\phi(r_k, S_j)$ for $1 \leq k \leq K$ are asymptotically Normal and independent. If $S_j(t)$ are assumed to be independent for $j = 1, \ldots, U$, $\phi(r_k, S_j)$ are asymptotically Normal and independent for $1 \leq k \leq K$ and $j = 1, \ldots, U$ [Brillinger, 2001]. The asymptotic independence

follows from the asymptotic Normality with an asymptotic covariance of 0 across r_k. Thus, the autocorrelation and dependence within a given process present in the time domain converges to 0 with respect to the frequency domain. From this result, it can be shown that $\hat{f}_{S_j,S_j}(r_k) \xrightarrow{d} f_{S_j,S_j}(r_k)\chi^2(2)/2$ independently for $k = 0, \ldots, T-1$ and, if $S_j(t)$ are assumed to be independent, for $j = 1, \ldots, U$ [Brillinger, 2001].

From the above results and assuming independent processes, we can define a log likelihood for the processes in the frequency domain, defined as

$$L(\hat{\boldsymbol{f}}, \boldsymbol{f}; S) = -\frac{1}{2}\sum_{j=1}^{U}\sum_{k=0}^{T-1}\frac{\hat{f}_{S_j,S_j}(r_k)}{f_{S_j,S_j}(r_k)} + \ln[f_{S_j,S_j}(r_k)] \tag{1.1}$$

where $\hat{\boldsymbol{f}}$ and $\boldsymbol{f}$ denote the matrices of periodograms and spectral density functions respectively. This likelihood is known as the Whittle likelihood [Whittle, 1951] with its asymptotic properties discussed in Dzhaparidze [1986].

1.3.2 Discrete Fourier Transform

A brief summary of the DFT is provided here, to motivate the later use of the wavelet transform. Please see Sundararajan [2001] for further details. Let $S(t)$ be a univariate stochastic process for $-\infty < t < \infty$. Suppose this process is only observed at a countable set of points; that is, we only consider $\{S(n) : n = 0, \pm 1, \pm 2, \ldots\}$, a discrete signal which we denote by $S(n)$. A discrete sinusoidal waveform is defined by $S(n)$ such that $S(n) = A\cos(\omega n + \theta)$ where $A > 0$ denotes the amplitude, ω denotes the frequency and θ denotes the phase shift. This process is oscillatory; it cycles between $-A$ and A across n at a rate defined by ω. This wave can also be expressed as $S(n) = C\cos(\omega n) + D\sin(\omega n)$ where $C = A\cos(\theta)$ and $D = -A\sin(\theta)$, referred to as its *rectangular form*. A third representation is the *complex sinusoid*, defined by $S(n) = A\exp[i(\omega n + \theta)]$ where i denotes the complex number such that $i^2 = -1$. This formulation can be seen by using Euler's identity, which states $\exp(ix) = \cos(x) + i\sin(x)$ for any real

number x and multiplying the identity by $A\exp(i\theta)$ to generate a complex sinusoid with arbitrary amplitude and phase shift.

Since the signal repeats at the same rate over the entire time course, only the amplitude, frequency, and phase shift are required to define it. Compared to it's realization in the temporal domain, this set of three parameters is a much smaller representation. Using these parameters, with the frequency considered the "independent" variable, defines the frequency or *spectral representation* of the signal $S(n)$. We now consider the case where the signal is a sum of distinct sinusoidal waves. That is

$$\begin{aligned} S(n) &= A_1\text{cos}(\omega_1 n + \theta_1) + A_2\text{cos}(\omega_2 n + \theta_2) + \ldots + A_J\text{cos}(\omega_J n + \theta) \\ &= \sum_{j=1}^{J} A_j\text{cos}(\omega_j n + \theta_j) \\ &= \sum_{j=1}^{J} A_j \exp[i(\omega_j n + \theta_j)] \end{aligned}$$

where integer $J > 0$. This is the signal in the time domain, though again we could uniquely identify it using the set of amplitudes, frequencies, and phase shifts, that is by the set $\{(A_j, \omega_j, \theta_j) : j = 1, \ldots, J\}$ or transforming the signal to its representation in the frequency domain. Assuming the signal is observed on $n = 0, \ldots, N-1$, of length N, this can be done using the *discrete Fourier transform* (DFT), given by

$$\phi(r_k, S) = \sum_{n=0}^{N-1} S(n)\text{exp}(-ir_k n) \tag{1.2}$$

where $r_k = 2\pi k/N$ for $k = 0, \ldots, N-1$, denote the *Fourier frequencies*. The set of DFT coefficients $\{\phi(r_k, S) : k = 0, \ldots, N-1\}$ are complex numbers whose real and complex quantities contain the power and phase coefficients for the frequency component in the signal $S(n)$ identified by frequency r_k. *Power* is used to denote the degree to which frequency r_k is present in the signal.

1.3.3 Supervised Singular Value Decomposition

In neural imaging studies, there will often be frequencies which are a priori expected to be in the data or are of particular scientific interest. These frequencies could be based on the experimental design (for example, the timing of a stimulus) or known characteristics of physiological phenomena (for example breathing and the heartbeat) [Buzsáki and Draguhn, 2004, Stam, 2000, Wu et al., 2008, Lee et al., 2013a]. As a result, when conducting dimension reduction on the data, these frequencies could be used to better remove the noise and extract the signal through a supervised algothrim. Bai et al. [2008] developed an extension to SVD, called *supervised SVD*, which allows the specification of frequencies of interest to identify when performing the decomposition. Thus, the other frequencies not specified can be removed from reconstructing the data after the decomposition. This especially useful for imaging studies due to the high dimension, large amount of noise, and temporal nature of the data and study design.

For M by N data matrix $\boldsymbol{X}$ such that rank$(\boldsymbol{X}) = R \leq \min(M, N)$, the SVD is $\boldsymbol{X} = \boldsymbol{V}\boldsymbol{D}\boldsymbol{U}^T$ where M by R matrix $\boldsymbol{V}$ and N by R matrix $\boldsymbol{U}$ are orthogonal, denoted as the *left* and *right singular vectors* respectively and $\boldsymbol{D}$ is the R by R diagnonal matrix of positive ($R > 0$) singular values. Denote the columns of V by $\boldsymbol{V} = [v_1, \ldots, v_R]$ and $\boldsymbol{U} = [u_1, \ldots, u_R]$ respectively and the non-zero values of $\boldsymbol{D}$ by $\boldsymbol{D} = \text{diag}[d_1, \ldots, d_R]$. For simplicity, consider the rank 1 approximation $(R = 1)$. Supervised SVD specifies a periodic form for the columns of U, that is

$$u(t_i) = a\text{sin}(2\pi\omega t_i + \phi) = a\text{cos}(\phi)\text{sin}(2\pi\omega t_i) + a\text{sin}(\phi)\text{cos}(2\pi\omega t_i)$$

where a is the amplitude, ω is the frequency and ϕ is the phase. Let $\psi = [a\text{cos}(\phi), a\text{sin}(\phi)]$ and $\boldsymbol{B} = (b_1, b_2)$ where $b_1 = [\text{sin}(2\pi\omega t_1), \ldots, \text{sin}(2\pi\omega t_N)]^T$ and $b_2 = [\text{cos}(2\pi\omega t_1), \ldots, \text{cos}(2\pi\omega t_N)]^T$. Thus, $u = \boldsymbol{B}\psi$. That is, u is spanned by b_1 and b_2. Thus, the usual rank 1 SVD estimation procedure is altered from

$$\min_{\boldsymbol{v},\boldsymbol{u}} ||\boldsymbol{X} - \boldsymbol{v}\boldsymbol{u}^T||^2 \tag{1.3}$$

to

$$\min_{\boldsymbol{v},\boldsymbol{B}} ||\boldsymbol{X} - \boldsymbol{v}\boldsymbol{u}^T||^2 \text{ s.t. } \boldsymbol{u} = \boldsymbol{B}\boldsymbol{\psi}$$

where $||.||^2$ denotes the squared Frobenius norm [Bai et al., 2008]. This use of the sinusoidal basis set for u forces the temporal portion of the decomposition to be formulated based on these periodic functions, creating a supervised process. This process can then be iterated to obtain the general rank R approximation using frequencies $(\omega_1, ...\omega_R)$.

1.3.4 Colored ICA for Continuous Components

Let $\boldsymbol{X}$ denote the V by T matrix of voxel-specific time-series of fMRI BOLD signals, where V is the number of voxels and T is the number of time points. ICA models the observed data as a linear combination of U latent variables (*independent components*) (ICs) which are assumed to be independent. More specifically, ICA decomposes the observed data matrix into a product of two matrices; one of which is a matrix of weights and the other is a matrix of realizations from the set of U independent latent variables. ICA comes in two forms, spatial ICA and temporal ICA [Bordier et al., 2010]. *Temporal ICA* corresponds to the decomposition

$$\boldsymbol{X} = \boldsymbol{A}\boldsymbol{S} \tag{1.4}$$

where $\boldsymbol{A}$ is a V by U matrix of weights and $\boldsymbol{S}$ is a U by T matrix of realizations from the latent variables. That is, the i^{th} row of $\boldsymbol{S}$ represents the time series for the i^{th} independent component. *Spatial ICA* corresponds to the decomposition $\boldsymbol{X^T} = \dot{\boldsymbol{A}}\dot{\boldsymbol{S}}$ where $\dot{\boldsymbol{A}}$ is a T by U matrix of weights and $\dot{\boldsymbol{S}}$ is a U by V matrix of realizations. In this scenario, the i^{th} row of $\dot{\boldsymbol{S}}$ represents the spatial process for the i^{th} independent component. Traditionally, ICA does not have a "noise" component. That is, the observed data is assumed to perfectly correspond to the linear combination of latent variables. However this model has been generalized to include an additive noise component [Beckmann and Smith, 2004] or embed noise directory within $\boldsymbol{S}$ [Lee et al., 2011]. With the ICs being independent, the correlation in the observed data is reflected in the within-IC

dependence (spatial or temporal dependence) and the contribution of the same ICs to multiple observations through mixing from $\boldsymbol{A}$.

Various methods have been created to fit the ICA model to data to estimate $\boldsymbol{A}$ and predict $\boldsymbol{S}$ [Hyvärinen and Oja, 1997, Hyvärinen and Oja, 2000, Beckmann and Smith, 2004, Lee et al., 2011]. Generally, $\boldsymbol{A}$ is assumed to be a nonsingular, square matrix with $\boldsymbol{W} = \boldsymbol{A^{-1}}$. First, $\boldsymbol{W}$ is estimated with $\boldsymbol{S}$ then predicted using the relation $\boldsymbol{S} = \boldsymbol{WX}$ [Hyvärinen and Oja, 2000]. Traditionally, ICA has some limitations with indentifiability of the ICs. ICs are assumed to be non-Gaussian (for the mixing matrix to be identifiable), and the scaling and ordering of the ICs are not identifiable. That is, given permutation matrix P, for a given ICA model $\boldsymbol{X} = \boldsymbol{AS} = \boldsymbol{APP^{-1}S}$ since permutation matrices are nonsingular. The model cannot distinguish between mixing matrices $\boldsymbol{AP}$ and $\boldsymbol{A}$ and between IC matrices $\boldsymbol{P^{-1}S}$ and $\boldsymbol{S}$. The scaling ambiguity is similar [Hyvärinen and Oja, 2000]. These fitting methods such as FastICA do not account for within-component dependence, relying on the marginal density functions of the univariate outcomes comprising each multivariate IC [Hyvärinen and Oja, 2000]. Since these ICs are generally across time or space, this assumption of the within-components joint densities being equivalent to the product of the marginals is likely incorrect. Furthermore, the information in the within-component dependence from the joint density may reflect connectivity within the brain [Lee et al., 2011].

Lee et al. [2011] develop an ICA fitting method which models the within-component dependence when fitting a temporal ICA model, referred to as *colored ICA*. Instead of using the density of the IC realizations, the authors use the density of the ICs in the frequency domain. Since the components are independent from one other, the spectral density matrix at frequency r is $\boldsymbol{f_{SS}}(r) = \text{diag}(f_{S_1,S_1}(r), \ldots, f_{S_U,S_U}(r))$ with each component's non-zero spectral density function reflecting the within-component dependence from autocorrelation. Recall the Whittle likelihood defined in Equation 1.1. From the ICA model, the likelihood is

$$L(\boldsymbol{W}, \boldsymbol{f}; \boldsymbol{X}) = -\frac{1}{2}\sum_{j=1}^{U}\sum_{k=0}^{T-1}\frac{2\pi {e_j}^T \boldsymbol{W}\hat{f}(r_k, \boldsymbol{X})\boldsymbol{W}^T e_j}{f_{S_j,S_j}(r_k)} + \ln[f_{S_j,S_j}(r_k)]$$

where $e_j = (0, \ldots, 0, 1, 0, \ldots, 0)^T$ with the jth entry being 1. The authors then consider modeling the ICs as stationary autoregressive (AR) and AR with moving average (ARMA) processes which have known, parametric forms for their spectral densities. For example in the ARMA(p,q) case, it is assumed that source j at time t satisfies

$$\Phi_j(B)S_j(t) = \Theta_j(B)\epsilon_j(t) \tag{1.5}$$

where B is the backshift operator, $\Theta_j(z) = 1 - \theta_{j,1}z - \ldots - \theta_{j,p_j}z^{p_j}$, $\Phi_j(z) = 1 - \phi_{j,1}z - \ldots - \phi_{j,p_j}z^{p_j}$, and $\epsilon_j(t) \sim N(0, {\sigma_j}^2)$ independent and identically distributed (i.i.d) for $t = 1, \ldots, T$. The noise component is reflected by $\epsilon_j(t)$, allowing stochastic deviation from the ICA model to be reflected in $\boldsymbol{S}$. This implies $f_{S_j,S_j}(r_k) = \frac{{\sigma_j}^2}{2\pi}\frac{|\Theta_j(e^{-ir})|^2}{|\Phi_j(e^{-ir})|^2}$, defining the Whittle likelihood in equation 1.5 [Brockwell et al., 1991].

Finally, $\boldsymbol{W}$ and the spectral denstiy parameters are estimated using a penalized optimization approach with the negative Whittle likelihood. Then $\boldsymbol{S}$ can be estimated using the relation above [Lee et al., 2011]. Thus, unlike other ICA fitting methods which assume a possibly erroneous within-component independence and fail to estimate the autocorrelation properies for the ICs, this autocorrelation is taken into account.

While this method reflects a temporal colored ICA model, Shen [2015] developed a spatial colored ICA model. They again use the Whittle likelihood defined in Equation 1.1 with the spatial spectral periodogram and density functions. For the spectral density, a spectral ARMA model is assumed, with the estimation process again done using a similar constrained optimization procedure as was done in the temporal ICA case. Again, this fitting procedure procedure preserves and conducts inference on the autocorrelation within the ICs, in the spatial domain in this case, while making a general distribution assumption (ARMA). It is important to note that the distributional assumptions of both colored ICA methods could be further minimized using a nonparametric estimation approach to modeling $f_{S_j,S_j}(r_k)$, such as a spline-based method.

1.3.5 Modeling Connectivity

Let $\boldsymbol{X}$ denote the T by V matrix of voxel-specific time-series of fMRI BOLD signals. In this section, we assume $\boldsymbol{X}$ represents fMRI data, however any spatio-temporal data matrix for which connectivity is of interest may be substituted (for example, EEG data). Assume $\boldsymbol{X}$ can be represented by

$$\boldsymbol{X} = \boldsymbol{U}\boldsymbol{A}\boldsymbol{S}$$

where $\boldsymbol{U} = [U_1, \ldots, U_R]$ is a T by R matrix with columns composed of temporal realizations, $\boldsymbol{A}$ is a R by R matrix and $\boldsymbol{S} = [S_1, \ldots, S_R]^T$ is a matrix with rows composed of spatial realizations with $S_i \perp S_j$ for $i, j = 1, \ldots, R$ and $i \neq j$. Denote the tth entry of U_i by $U_i(t)$ and assume $U_i(t) = a_i \text{sin}(2\pi\omega_i t + \phi_i) + \epsilon_i(t)$ for $i = 1, \ldots, T$ where $\epsilon_i(t)$ is non-Gaussian with $\text{E}[\epsilon_i(t)] = 0$ and $\text{Cov}[\epsilon_i(t)\epsilon_i(t')] = 0$ for $t \neq t'$ and $\text{Cov}[\epsilon_i(t), \epsilon_j(t')] = 0$ for $t, t' = 1, \ldots, T$ and $i, j = 1, \ldots, R$ except where $i = j$ and $t = t'$. From the ICA model in Equation 1.4, $\boldsymbol{A}$ is the mixing matrix and $\boldsymbol{S}$ is the matrix of IC realizations, in this case spatial.

Thus, we decompose the data matrix into separate temporal, mixing, and spatial components respectively. Traditionally, $\boldsymbol{U}$ and $\boldsymbol{A}$ would only be modeled as a product; the two components separately be not identifiable. This separation allows the weighting of the ICs' realizations by time and the between-component weighting to be separately identified, creating a more complete reflection of connectivity then traditional ICA. Through $\boldsymbol{U}$ we explicitly model the dynamic neural connectivity across time, temporally modeling the mixing of the ICs through $\boldsymbol{A}$. Between-network connectivity is modeled through $\boldsymbol{A}$. Finally, through the ICs in $\boldsymbol{S}$, within-network connectivity is modeled, with these components reflecting latent neural activity networks without the need for additional parametric modeling (such as a hemodynamic response function). Locations with high levels of activity in a given IC reflect locations with neural activity which are associated, with the autocorrelation in a given IC reflected in its spectral density [Lee et al., 2011].

The fitting procedure is now detailed. From above, $\boldsymbol{X}^T = \boldsymbol{S}^T\boldsymbol{A}^T\boldsymbol{U}^T$. The supervised SVD decomposition of $\boldsymbol{X}^T$ is $\boldsymbol{X}^T = \boldsymbol{V}^*\boldsymbol{D}^*\boldsymbol{U}^{*T}$. From Supervised SVD, $\boldsymbol{U}^{*T}$ contains the basis

vectors spanning the temporal dimension of the data, denoted by $\boldsymbol{U}^T$. Thus, $\boldsymbol{U}^{*T}$ estimates the "signal" portion of $\boldsymbol{U}$, that is the $\boldsymbol{U}$ with the noise component removed, assuming the columns of $\boldsymbol{U}$ are realizations of a harmonic process. Denote $\boldsymbol{Y}^* = (\boldsymbol{V}^*\boldsymbol{D}^*)^T$. Fitting spatial colored ICA, the estimated decomposition of $\boldsymbol{Y}^*$ is $\hat{\boldsymbol{Y}}^* = \hat{\boldsymbol{A}}^*\hat{\boldsymbol{S}}^*$. These $\hat{\boldsymbol{A}}^*$ and $\hat{\boldsymbol{S}}^*$ serve as estimators of $\boldsymbol{A}$ and $\boldsymbol{S}$ respectively.

The use of supervised SVD to identify the temporal components in the observed data also is used to remove components which have frequencies different from those specified a priori (noise components for example). This step is a similar to bandpass filtering, in which components present in the data with frequencies inside a specified range are retained with the rest removed. However, since bandpass filtering is done on the entire observed dataset, due to the mixing from $\boldsymbol{S}$, frequencies observed in the data may differ from those present in the columns of $\boldsymbol{U}$. This would result in the removal of components which may be of interest. The use of supervised SVD directly estimates the temporal components in $\boldsymbol{U}$, avoiding this problem, which can be seen in the simulation results in Section 1.4.

While frequencies can be used to identify distinct temporal components of interest, some task designs may have tasks which cycle at similar frequencies but are differentiated by their phase. Recall the periodic form defined in Section 1.3.3, defined as a sine wave with amplitude a, frequency ω, and phase ϕ. When two components of the same frequency are of interest, supervised SVD can struggle to identify the separate components by default (see Section 1.4). Instead, the phase parameter can also be specified to inform the algorithm based on scientific background or the task sequence. The supervised SVD method can then restructured to

$$\min_{\boldsymbol{v},\boldsymbol{B}} ||\boldsymbol{X} - \boldsymbol{v}\boldsymbol{u}^T||^2 \text{ s.t. } \boldsymbol{u} = \boldsymbol{B}\boldsymbol{\psi}$$

where $B = (b_1, \ldots, b_N)$ with $b_i = \cos(\phi)\sin(2\pi\omega t_i) + \sin(\phi)\cos(2\pi\omega t_i)$ for $i = 1, \ldots, N$ and $\psi = a$, with ω and ϕ specified. For the estimation of this rank 1 model and modeling remaining components, the same processed described in Section 1.3.3 can be used.

1.4 Simulated Data Analysis

To assess the accuracy of the decomposition method proposed in Section 1.3.5, we applied it to simulated spatio-temporal data. To illustrate functional connectivity which can be more easily physiologically interpreted, we considered a task-based experimental design. Note that due to the supervised nature of the proposed method, it is best suited to task-based designs then resting state study designs in order to more easily identify a priori temporal components likely to be present. This can be done with resting state designs as well based on previous studies and scientific knowledge, but is generally less clear.

A simulated data matrix was generated with spatial and temporal dimensions to mimic standard imaging data (for example fMRI and EEG). The generated data reflected a blocked experiment where subjects switch between two different stimuli with a stimulus-free rest block in between. The two stimuli were designed to stimulate right and left pointer finger tapping respectively. The stimuli were administered during separate blocks of time, each block with a 40 sample duration. The rest blocks were also 40 samples long. The total duration of the experiment was 480 samples, with a rest block at the start followed by a right finger stimulus block. This resulted in three right finger blocks, three left finger blocks, and six rest blocks.

Denote the T by V observed data by $\boldsymbol{X}$. The temporal components of the data are contained in the columns of $\boldsymbol{U} = [U_1, \ldots, U_R]$ where $R = 5$. For $i = 1, \ldots, 5, U_i = [U_i(1), \ldots, U_i(T)]^T$ where $T = 480$, representing the large temporal dimension generally present in imaging data. The first and second components, $\boldsymbol{U_1}$ and $\boldsymbol{U_2}$, represented the time course specified by the task sequence for the right and left finger stimulus respectively. These were modeled as noise-free step functions, with

$$U_1(t) = \begin{cases} 1 & 41 \leq t \leq 80, 201 \leq t \leq 240, 361 \leq t \leq 400 \\ 0 & \text{else} \end{cases}$$

and

$$U_2(t) = \begin{cases} 1 & 121 \leq t \leq 160, 281 \leq t \leq 320, 441 \leq t \leq 480 \\ 0 & \text{else} \end{cases}$$

for $t = 1, \ldots, T$. While these were not necessarily harmonic processes they are periodic and thus can be approximated using sinusoidal waves. Using a smoothed periodogram to estimate the corresponding frequency resulted in a single peak at $\omega_1 = \omega_2 = 0.0125$.

The third and fourth components were considered to be a mixture of signal and noise, with $U_i(t) = a_i \text{sin}(2\pi\omega_i t + \phi_i) + \epsilon_i(t)$ with $a_i = 0.5, \phi_i = 0$ for $i = 3, 4$ and $\omega = (\omega_3, \omega_4) = (0.4, 0.3)$. The amplitude of 0.5 was chosen to reflect the task temporal component (with an peak of 1) dominating the others. The noise component $\epsilon_i(t)$ was generated i.i.d from the Uniform[-0.1, 0.1] distribution for all $t = 1, \ldots, 480$. These components represented the temporal attributes of underlying physiological processes such as breathing and heartbeat, which are generally not of interest scientifically but contribute to the neurological activity observed in the data. Finally, the fifth temporal component $U_5(t)$, was considered pure noise, generated i.i.d from the Uniform[-0.1, 0.1] distribution for all $t = 1, \ldots, 480$. These temporal components from one of the simulations are visualized in Figure 1.1, including (from top to bottom) a smoothed periodogram of the component's realizations, the signal portion of the component, and the component's realizations, for the first four components (as last is pure noise).

The spatial components form the independent components of the model and are contained in the rows of $\boldsymbol{S} = [S_1, \ldots, S_R]^T$ where $R = 5$. For $i = 1, \ldots, 5$, $S_i = [S_i(1), \ldots, S_i(V)]$ where $V = 400$, reflecting a two dimensional brain slice of 400 locations (20 by 20 pixil image) from an fMRI scan, representing the large spatial dimension generally present in imaging data. The first four spatial components were simulated noise-free, with elements set to 0 (inactive region) or 1 (active region). The fifth spatial component was considered pure noise, with $\epsilon_{S_5} = [\epsilon_{S_5}(1), \ldots, \epsilon_{S_5}(400)]^T$, where $\epsilon_{S_5}(v) \sim N(0, 0.1)$ i.i.d. for $v = 1, \ldots, 400$.

The first and second components, S_1 and S_2, represented the latent spatial maps for neural activity related to the right and left finger stimulus respectively. The third and fourth compo-

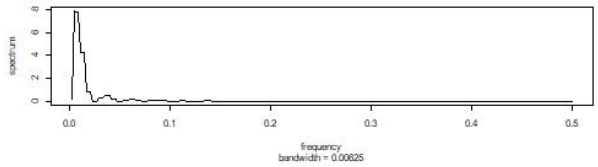

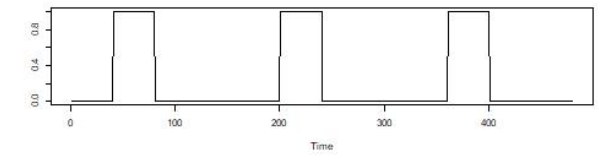

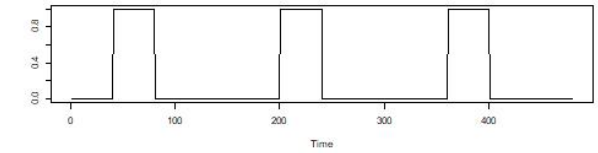

(a) Right Hand

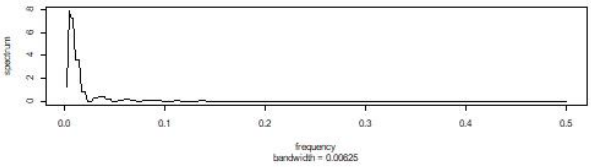

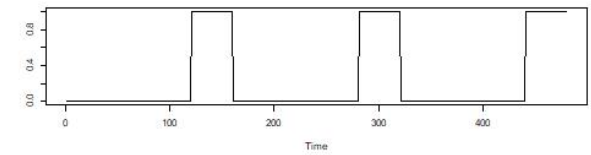

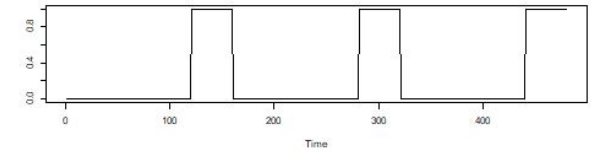

(b) Left Hand

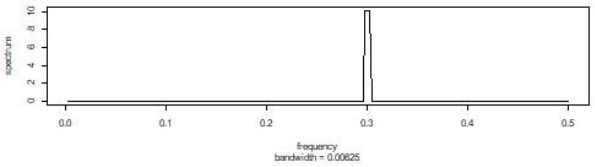

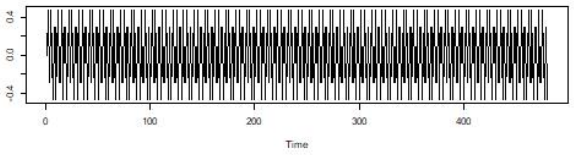

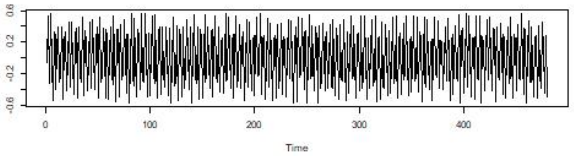

(c) Breathing

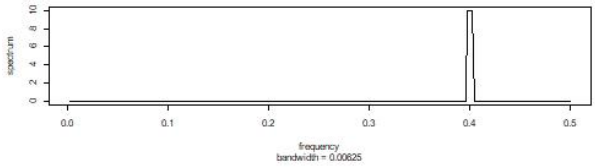

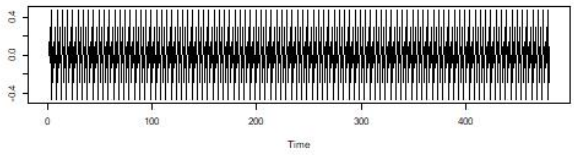

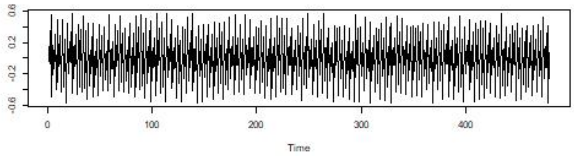

(d) Heartbeat

Figure 1.1: Simulated temporal components for finger tapping experiment.

nents, S_3 and S_4, represented the latent spatial maps for the two underlying physiological process (breathing and heartbeat). Figure 1.2 visualizes the realized values for each of the first four spatial components (fifth not shown), from one of the simulations.

Finally, 5 by 5 matrix $\boldsymbol{A}$ defines the mixing matrix for the components, which was set differently depending on which stimulus was active (right finger or left finger). These were set to model different components being activated depending on the stimulus present, creating two different matrices $\boldsymbol{A_{RS}}$ and $\boldsymbol{A_{LS}}$, which alternated as the mixing matrix through the experiment's duration. The matrices were defined as

$$\boldsymbol{A_{RS}} = \begin{pmatrix} 1 & 0 & 0 & 0 & 0 \\ 0 & 0 & 0 & 0 & 0 \\ 1 & 0 & 1 & 0 & 0 \\ 1 & 0 & 0 & 1 & 0 \\ 0 & 0 & 0 & 0 & 1 \end{pmatrix} \qquad \boldsymbol{A_{LS}} = \begin{pmatrix} 0 & 0 & 0 & 0 & 0 \\ 1 & 0 & 0 & 0 & 0 \\ 0 & 1 & 1 & 0 & 0 \\ 0 & 1 & 0 & 1 & 0 \\ 0 & 0 & 0 & 0 & 1 \end{pmatrix}$$

which resulted in the each hand's component being activated only during that hand's stimulus, along with the each hand's activation being associated with the two physiological processes. Finally, the noise component was activated independently of the others. The changing between these matrices during the experiment's duration, combined with the temporal components in $\boldsymbol{U}$, reflected the changing brain dynamics and dynamic connectivity in relation to the stimuli. The observed data $\boldsymbol{X}$ was then generated by

$$\boldsymbol{X} = \begin{cases} \boldsymbol{U A_{RS} S} & 1 \leq t \leq 80, 161 \leq t \leq 240, 321 \leq t \leq 400 \\ \boldsymbol{U A_{LS} S} & \text{else} \end{cases}$$

reflecting the switching between stimuli every 80 time points (40 for the rest block and 40 for the stimulus being active). This time course can also be visualized to better illustrate the experimental design with respect to stimulus onset, as shown in Figure 1.3. Color indicates stimulus type

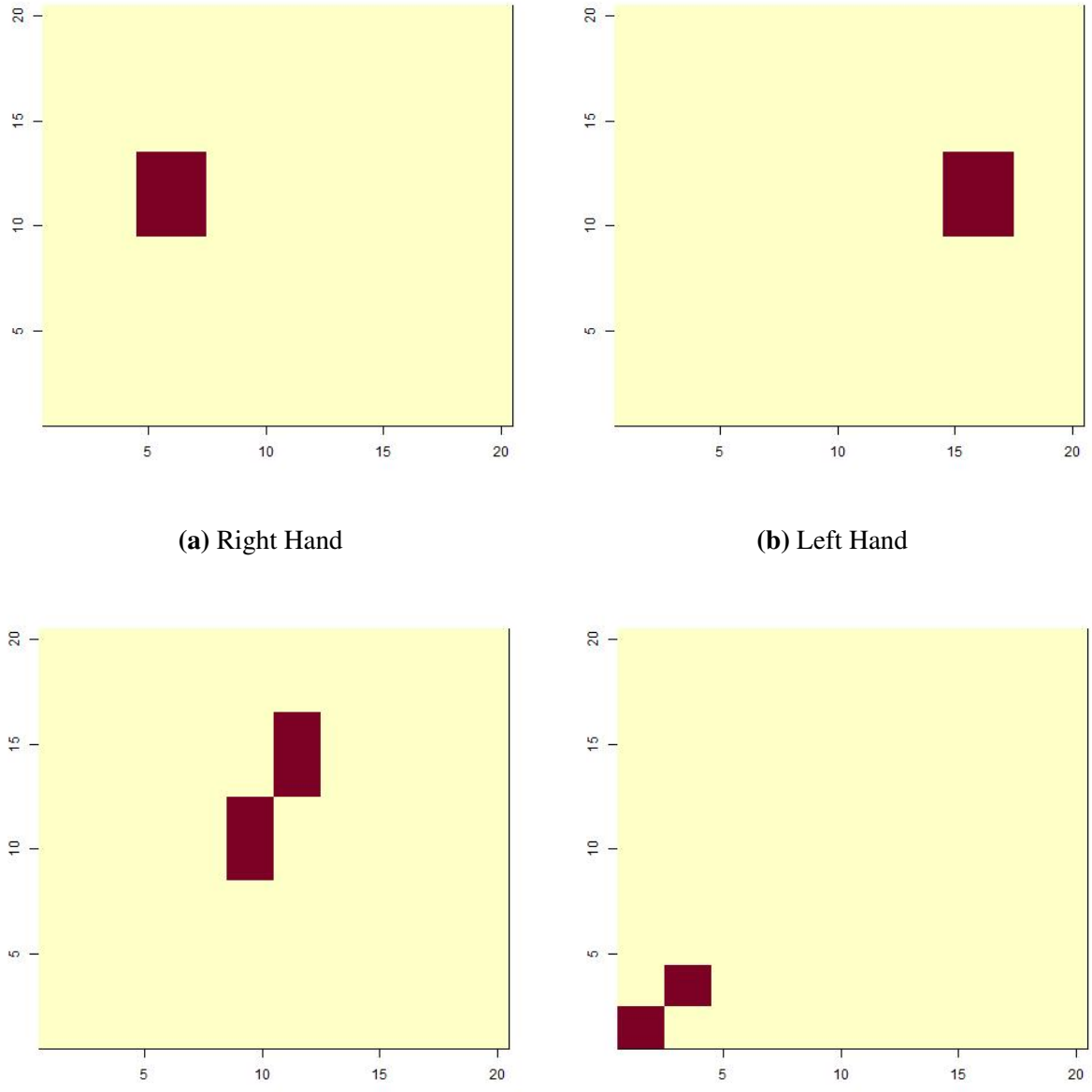

(a) Right Hand

(b) Left Hand

(c) Breathing

(d) Heartbeat

Figure 1.2: Simulated spatial components for finger tapping experiment.

(left or right hand), with “Inactive” denoting a period of rest and “active” denoting a stimulus being present.

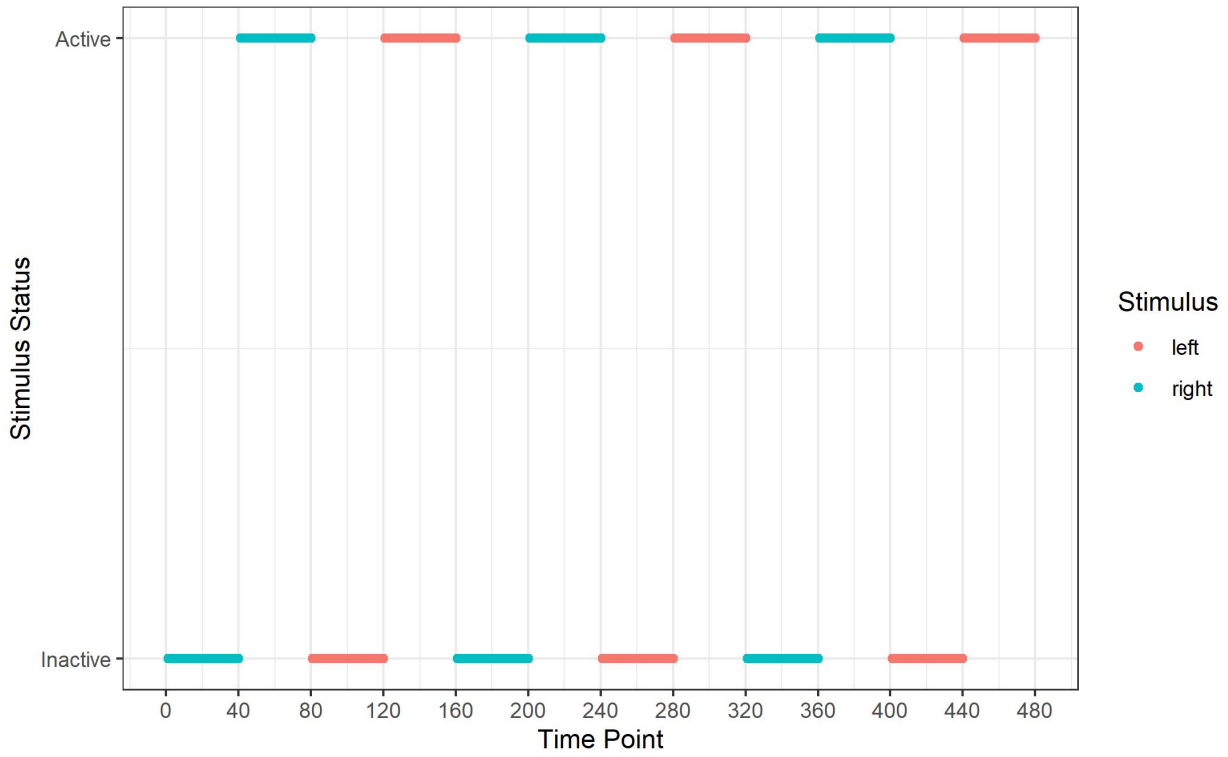

Figure 1.3: Time course of stimulus throughout stimulated experiment.

.

These mixing matrices and the previously detailed temporal components reflected dynamic neural activity features tied to the stimuli during the experiment. Through the stimuli, the changing brain dynamics can be associated with specific behavior, facilitating interpretation of the model. Connectivity is reflected in $\boldsymbol{U}$, $\boldsymbol{A}$, and $\boldsymbol{S}$, which each matrix containing a type of regional dependence. Regions tied to specific physiological phenomena are modeled using $\boldsymbol{S}$, denoting spatial “networks” or “within-network” connectivity. Mixing matrices $\boldsymbol{A_{RS}}$ and $\boldsymbol{A_{LS}}$ modeled associations between the regions tied to these phenomena or “between-region” connectivity. These associations shifted between the two hand-related regions as the stimulus shifted. For example, the third and fourth rows of $\boldsymbol{A_{RS}}$ indicated that the task response was spatially associated with breathing and heartbeat (and the same for $\boldsymbol{A_{LS}}$).

We evaluated the sSVD-cICA model based on its accuracy in estimating $\boldsymbol{U}$, $\boldsymbol{A_{RS}}$, $\boldsymbol{A_{LS}}$, and $\boldsymbol{S}$ from observed data $\boldsymbol{X}$. The following methods were also used for estimation to compare to the proposed method: 1) standard SVD followed by cICA, and 2) bandpass filtering, followed by standard SVD, followed by cICA. When bandpass filtering, we first used a standard filter with a rectangular window and a frequency range of $(\omega_{U_{min}}, \omega_{U_{max}})$, denoting the minimum and maximum frequencies of the non-noise components in $\boldsymbol{U}$. For the data described above, $\omega_{U_{min}} = 0.0125$ which denoted the task frequency and $\omega_{U_{max}} = \omega_3 = 0.4$. This filter was applied to each spatial location's time series data from $\boldsymbol{X}$ (columns of data matrix).

Using the time stamps tied to the right and left hand stimuli (see Figure 1.3), the observed data was split into two pieces. One dataset consisted of the time points tied to the right hand stimulus schedule (blue line in figure) and the other dataset consisted of the time points tied to the left hand stimulus schedule (red line in figure). Each set contained all of the spatial locations. In order to estimate $\boldsymbol{A_{RS}}$ and $\boldsymbol{A_{LS}}$, these two datasets were analyzed separately using the 3 considered methods described above. When using supervised SVD, the frequencies specified were ω_1, ω_3 and ω_4 to identify the task, heartbeat, and breathing components respectively. Correspondingly, when using standard SVD, three right and left singular vectors were specified.

Figure 1.4 displays the estimation results when using the three described methods with the simulated right-hand stimulus data. The plot consists of 12 cells in 4 rows and 3 columns. The first 3 rows index the 3 non-noise components while the fourth row displays the estimated mixing matrix $\boldsymbol{A_{RS}}$. For each of the entries in the first 3 rows, the estimated spatial component matrix is displayed on top along with the estimated temporal component's time course and raw periodogram in the bottom left and right respectively. The 3 columns indicate the method used to obtain the estimates. The proposed method is denoted in the figure by column label *sSVD-cICA*, the method using standard SVD with cICA is denoted by *SVD-cICA* and the use of bandpass filtering first is denoted by *BP-SVD-cICA*. While not shown here, the singular values for all SVD methods were uniformly high when specifying 3 components, indicating that sSVD and SVD identified the three components as being strongly present in the data.

However, only sSVD-cICA accurately estimated all three matrices. Spatially, all three methods were able to identify the separate components with a similar level of accuracy. Temporally, the use of sSVD was able to accurately identify the harmonic components of interest as indicated by the periodograms in the figure. However, other methods showed a higher degree of error in their estimation. For the task-based temporal component, both methods were unable to isolate the task-specific frequency component, instead returning a component with all three frequencies. For the other two temporal components, the dominant frequency was identified, though with some contamination from the other two frequencies (especially with the breathing-related component). Finally, the non-diagonal elements were not identified by these other methods. This was likely due to the contamination of the non-task related frequencies in the estimated task-based temporal component, instead of this association being identified in the mixing matrices. Figure 1.5 displays the results with the simulated left-hand stimulus data, which were very similar to the right-hand data results.

In data generated above, the noise components were all additive and constant across the time course. However, outliers which appear as spikes with high observed magnitudes, are inevitable in fMRI data due to complications such as problems with the MR scanners or abrupt subject movements [Bai et al., 2008]. To reflect this in the simulated data described above, we add randomly generated spikes to the temporal components in $\boldsymbol{U}$. First, 5 percent of the entries in $\boldsymbol{U}$ were choosen randomly. For these entries in the first 4 components of $\boldsymbol{U}$, the previous values were replaced by spikes generated from the Uniform[-7, -1] (first half of selected entries) or Uniform[1, 7] (second half of entries) distributions. For these entries in the last component, due to difference in scale compared to the first 4, the previous values were replaced by spikes generated from the Uniform[-6.5, -0.5] (first half of selected entries) or Uniform[0.5, 6.5] (second half of entries) distributions. These cutoff points were chosen based on 1.5 times the interquartile range (IQR) for the 1st 4 components and last component respectively, in order to follow the standard definition for an outlier. This data was then analyzed in the same fashion as before, using the

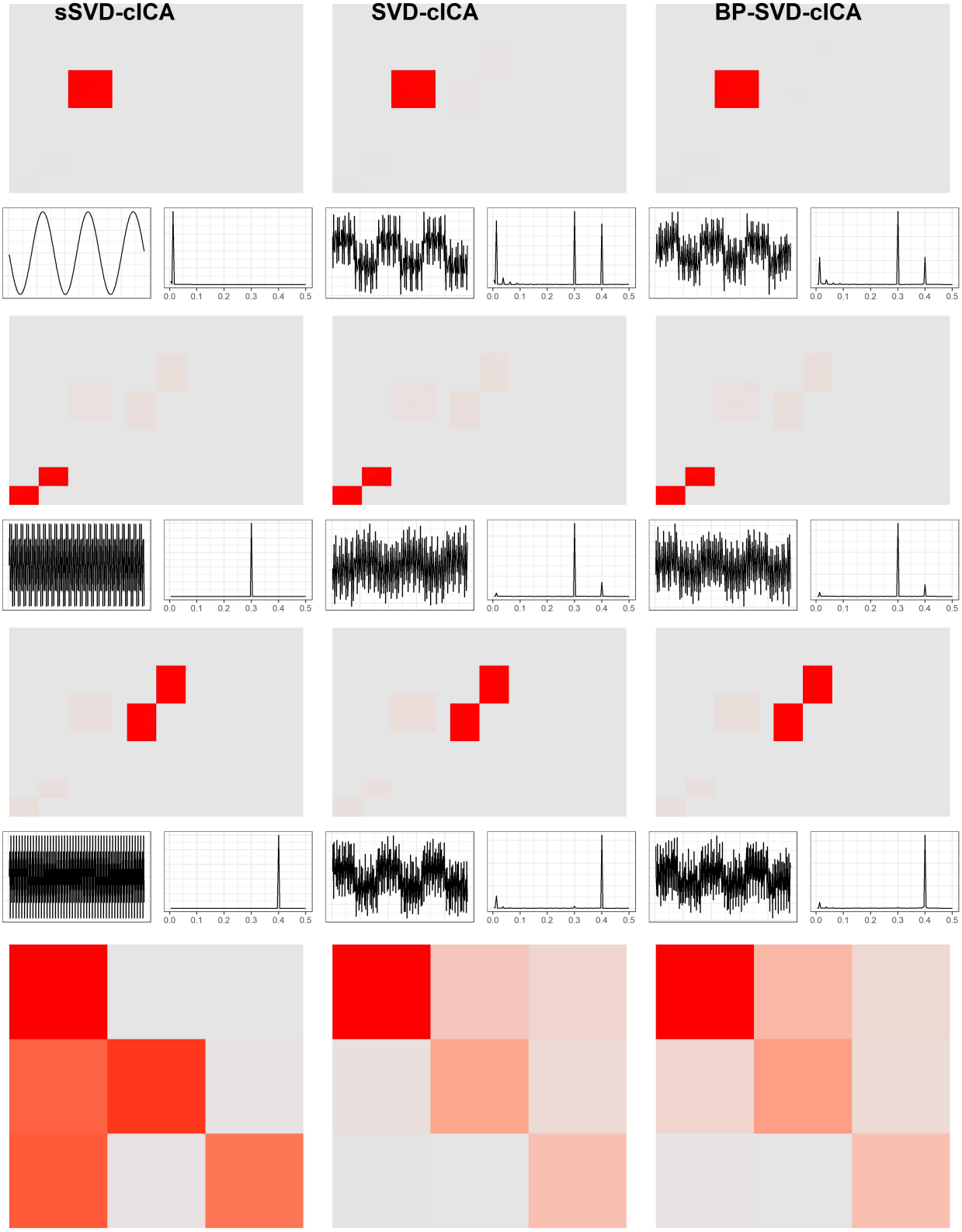

Figure 1.4: Estimation results from single right-hand stimulus time course simulated data.

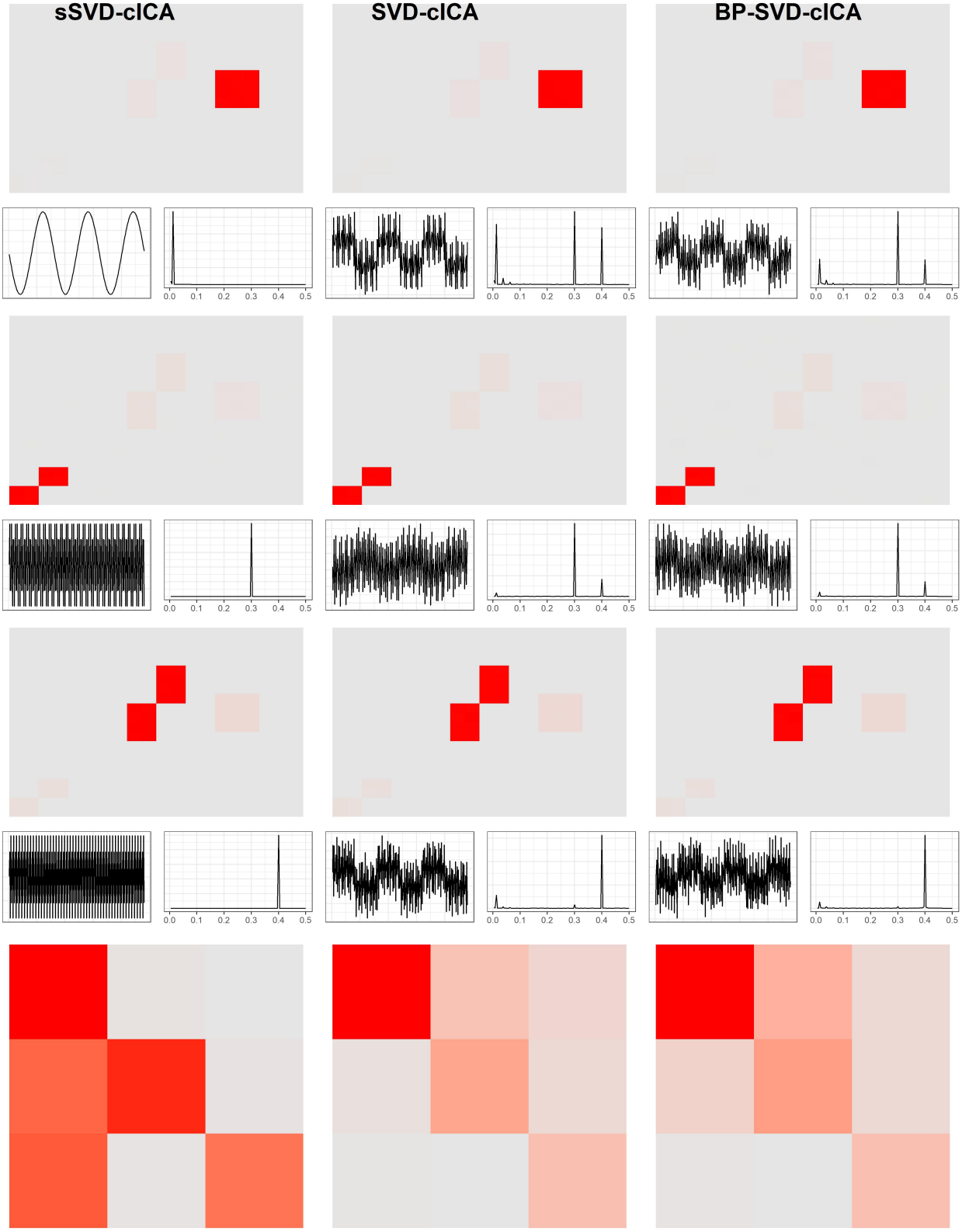

Figure 1.5: Estimation results from single left-hand stimulus time course simulated data.

same three chosen methods, with the goal of accurately estimating $\boldsymbol{U}$, $\boldsymbol{A_{RS}}$, $\boldsymbol{A_{LS}}$, and $\boldsymbol{S}$ despite the inclusion of the random spikes.

Figure 1.6 displays the estimation results when using the three described methods with the simulated right-hand stimulus data with spikes. While not shown here, the singular values for all SVD methods were again uniformly high when specifying 3 components, including that sSVD and SVD identified three components as being strongly present in the data. However, only sSVD-cICA accurately estimated all three matrices. Spatially, SVD-cICA and BP-SVD-ICA were able to identify the three regions as being active, however they were not separately identified for each component. Furthermore, one of the spatial components identified by these two methods was uninterpretable, essemtially pure noise. Temporally, the use of sSVD was able to accurately identify and then isolate the harmonic components of interest as indicated by the periodograms. This was not the case with the other methods, with elevated values in the periodogram throughout the frequency range despite only a single one being present in each temporal component. Finally, the mixing matrix values corresponding to 1 were showed high magnitudes (in absolute value) in the estimated matrix from sSVD-cICA. This was not the case with other two methods, as only the diagonal entries accurately returned a high magnitude. The magnitude of the top left entry (the task-related component) returned by sSVD-cICA had a lower magnitude compared to the estimates from the other two methods.

Figure 1.7 displays the results with the simulated left-hand stimulus data with spikes. The temporal and mixing matrix estimation results were very similar to those from the right-hand data. The proposed method accurately estimates both matrices (recall ICA is permutation/order invariant). The other two methods are unable to accurately identify the individual temporal components, as seen when observing the jagged periodogram from the estimated components. The exception was the task frequency as seen in the periodogram of the third returned component, though the component also contains a number of other frequencies as well. Spatially all three methods were able to accurately identify all three components, in contrast to the right-hand analysis where only the proposed method was able to do this. This was likely due to an unequal

distribution of the spikes between the left and right hand time points due to the results being from a single simulation. This distribution is especially important due to the sensitivity of traditional SVD to outliers [Bai et al., 2008].

To assess the statistical properties of the methods, we repeated this simulation analysis 1000 times for both the cases where spikes were included and where they were not included. Using the known time stamps, the left and right stimulus data were analyzed separately for each simulated dataset. The results for the simulated data without spikes were very similar to the simulated example above without spikes. Thus, for brevity, we focus on the simulated data with spikes, in which the methods showed greater differences in their performance. Due to the scaling invariance property of ICA, metrics need to be chosen which are on a standardized scale in order to compare the results across the simulations. The ordering invariance property of ICA also needs to be accounted for. For the temporal components, for each simulation and method used, absolute correlations were computed between each estimated component's and true component's periodogram. The estimated components were then paired with the true component based on the component with which it had the maximum absolute correlation. This ordering process was also done for the spatial components based on the realizations of the estimated and true components. Finally, for the mixing matrix estimates, the rows and columns were sorted so that the indices matched the re-ordered spatial components. To normalize the mixing matrix entries onto a scale between 0 and 1, the entries were transformed using the following:

$$\tilde{a}_{ij} = \frac{|a_{ij}| - \min(|a_{ij}|)}{\max(|a_{ij}|) - \min(|a_{ij}|)}$$

where a_{ij} indicates the mixing matrix entry at row i and column j. This puts the matrix entries all on the same scale across the simulations, and compares the entries to their minimum value (0) and maximum value (1).

These results are visualized in Figures 1.8-1.13 using boxplots of the absolute correlations for the temporal and spatial components, and of the normalized values for the estimated mix-

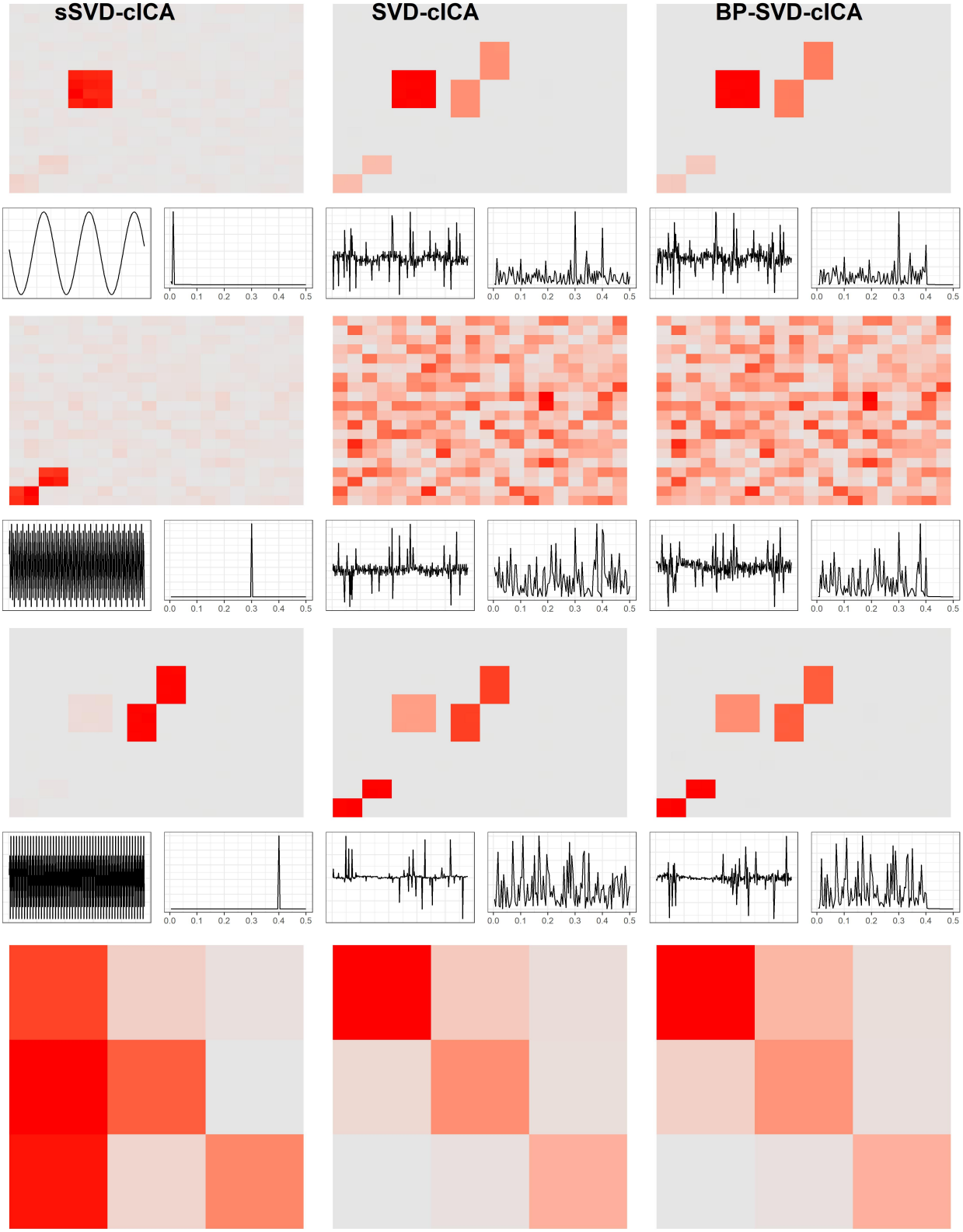

Figure 1.6: Estimation results from single right-hand stimulus time course simulated data with spikes.

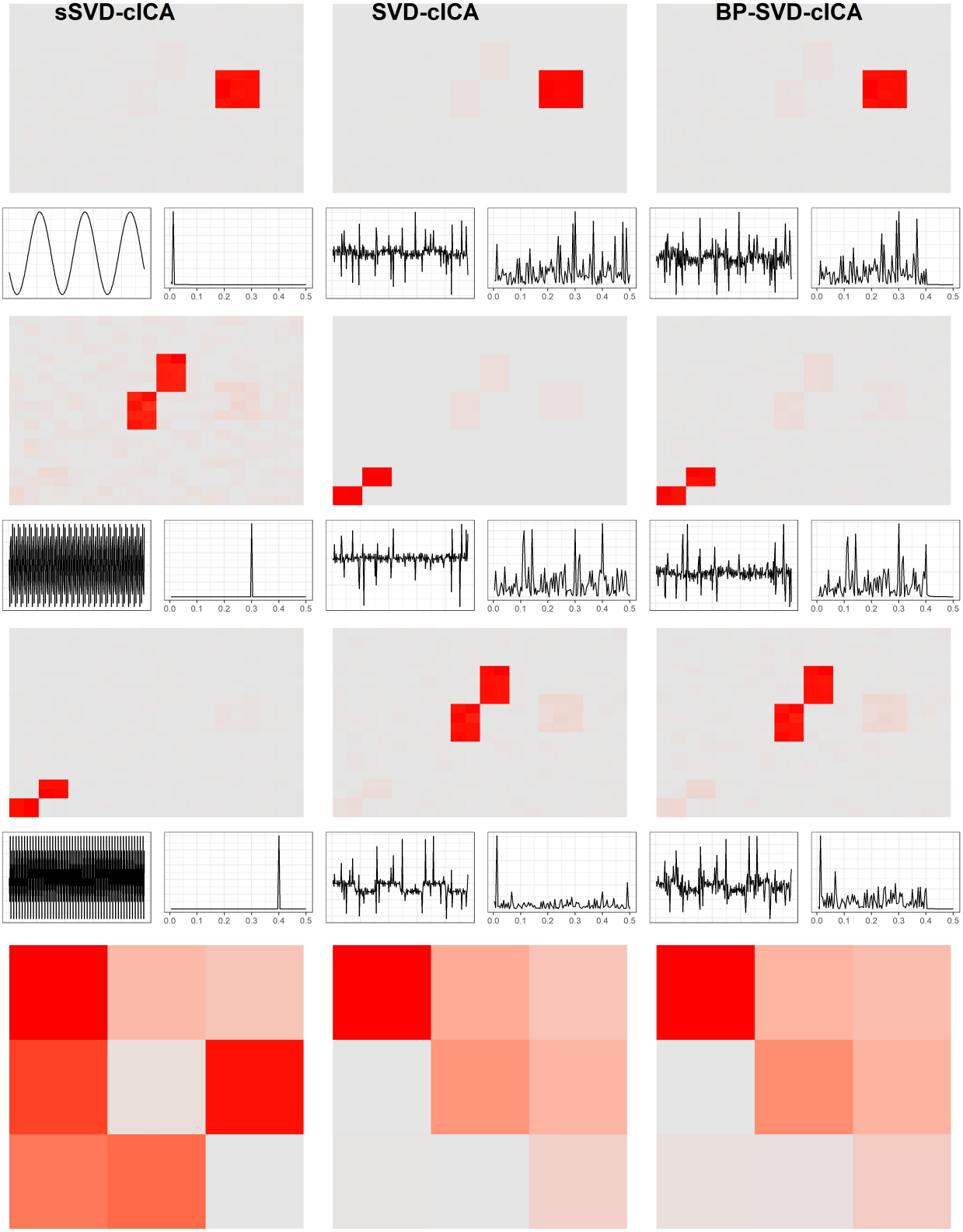

Figure 1.7: Estimation results from single left-hand stimulus time course simulated data with spikes.

ing matrices. The plot consists of 15 cells in 5 rows and 3 columns. The columns denote the estimated components and the rows indicate the true components. Boxplots of the absolute correlation between the periodograms between these components are provided in the respective cell, grouped by the method used to estimate the temporal component. Cells where the true and estimated component labels match are colored in red for the temporal and spatial component results. For the estimated mixing matrix results, entries equal to one in the true mixing matrix are colored in red. Boxplots for the standardized mixing matrix values for each of the considered methods are provided.

There were more noticeable differences in the examined methods when used in the data with spikes compared to without spikes. As expected from Bai et al. [2008], traditional SVD methods struggled to accurately identify the temporal components compared to the proposed method. Across the 1000 simulations, the median correlations between the estimated and true components were much lower for the traditional SVD methods compared to the proposed, and had noticeably higher variance. This higher variance was also noticeable when comparing the spatial component and mixing matrix estimation results between the methods.

Finally, modeling temporal components with different phases is now examined using the proposed methods in a simulation study. The spatial components were the same as the previous simulation studies. The temporal components were specified as $U_i(t) = \sin(2\pi\omega_i t + \phi_1) + \epsilon_{i,t}$ for $i = 1, \ldots, 4$ and $t = 1, \ldots, T$ with $\omega_1 = 0.1, \omega_2 = 0.2$, and $\omega_3 = \omega_4 = 0.025$. Term $\epsilon_{i,t}$ denotes additive noise generated from the Uniform[-0.5,0.5] distribution. The phases were defined by $\phi_1 = \phi_2 = \phi_4 = 0$ and $\phi_3 = \pi/3$. Note that certain phase combinations may not be identifiable, specifically if the phase equals $2k\pi$ for positive integer k. These temporal components are shown in Figure 1.14. As was done before, a fifth component $U_5(t)$ was simulated as $T = 480$ independent draws from the Uniform[-0.1,0.1] distribution as a pure noise component. The mixing matrix was similar to the hand-stimulus data from before, though only a single matrix was used unlike in that scenario, defined as

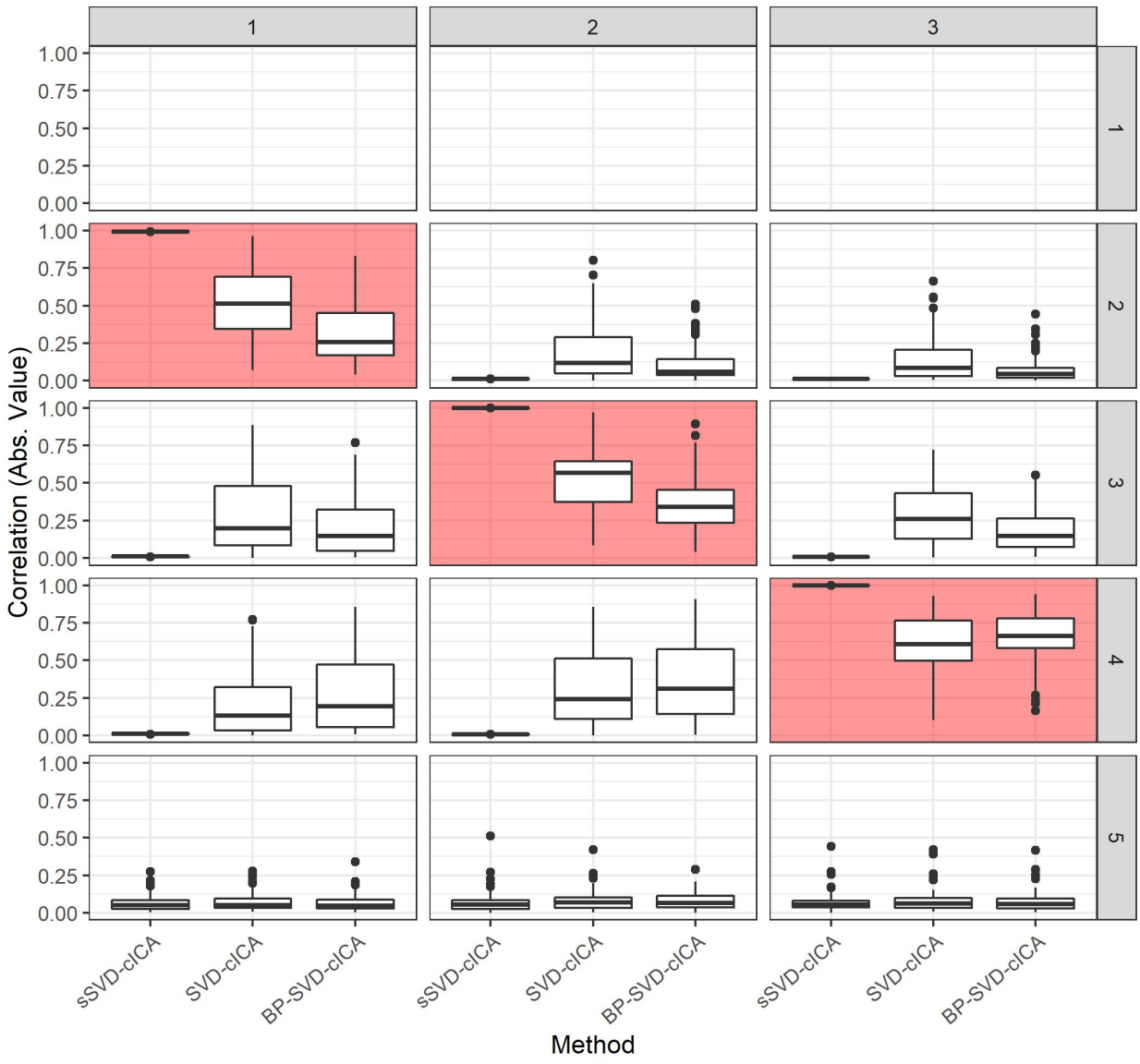

Figure 1.8: Temporal component results from the left-hand stimulus simulated data with spikes, across 1000 simulations.

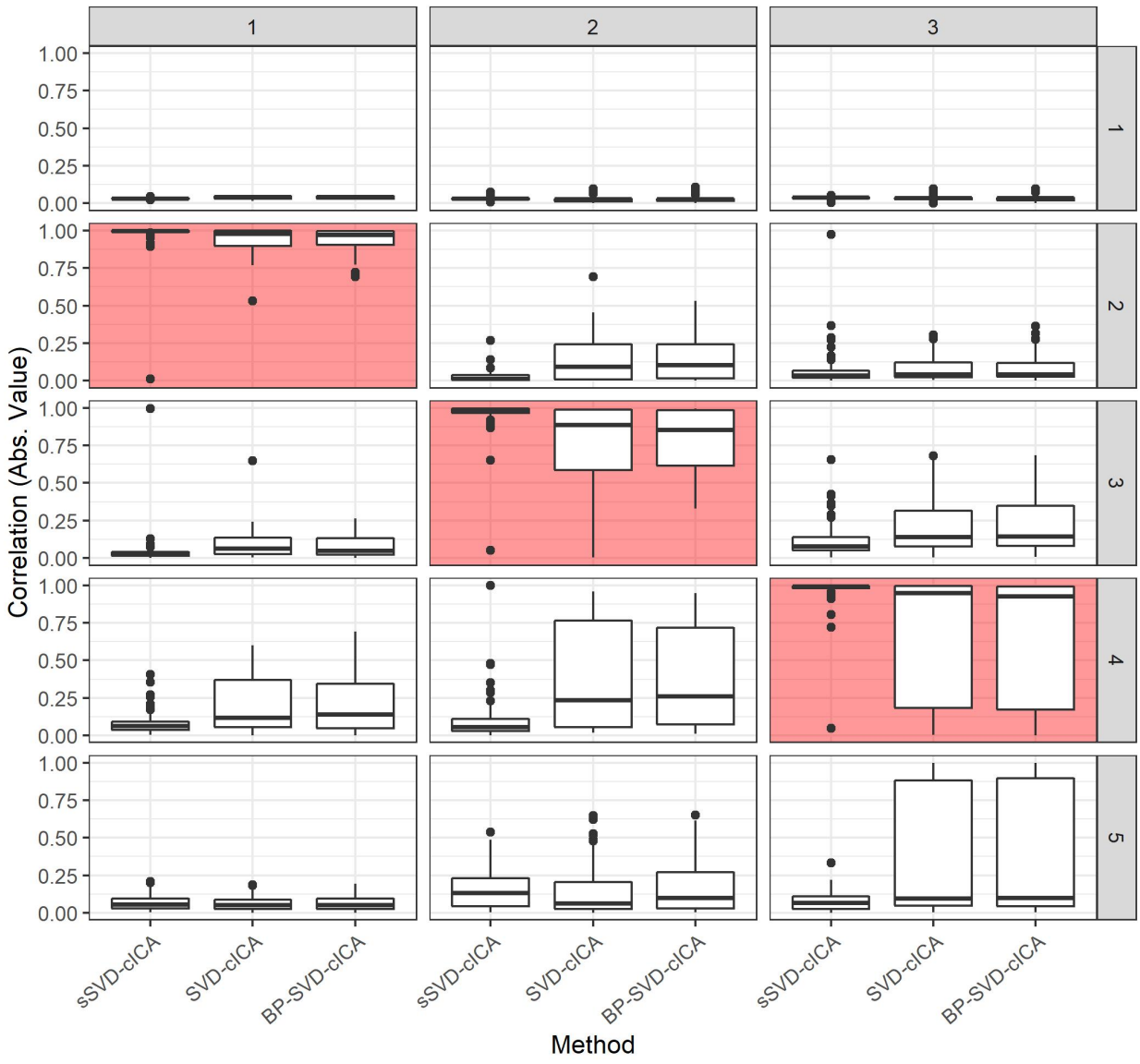

Figure 1.9: Spatial component results from the left-hand stimulus simulated data with spikes, across 1000 simulations.

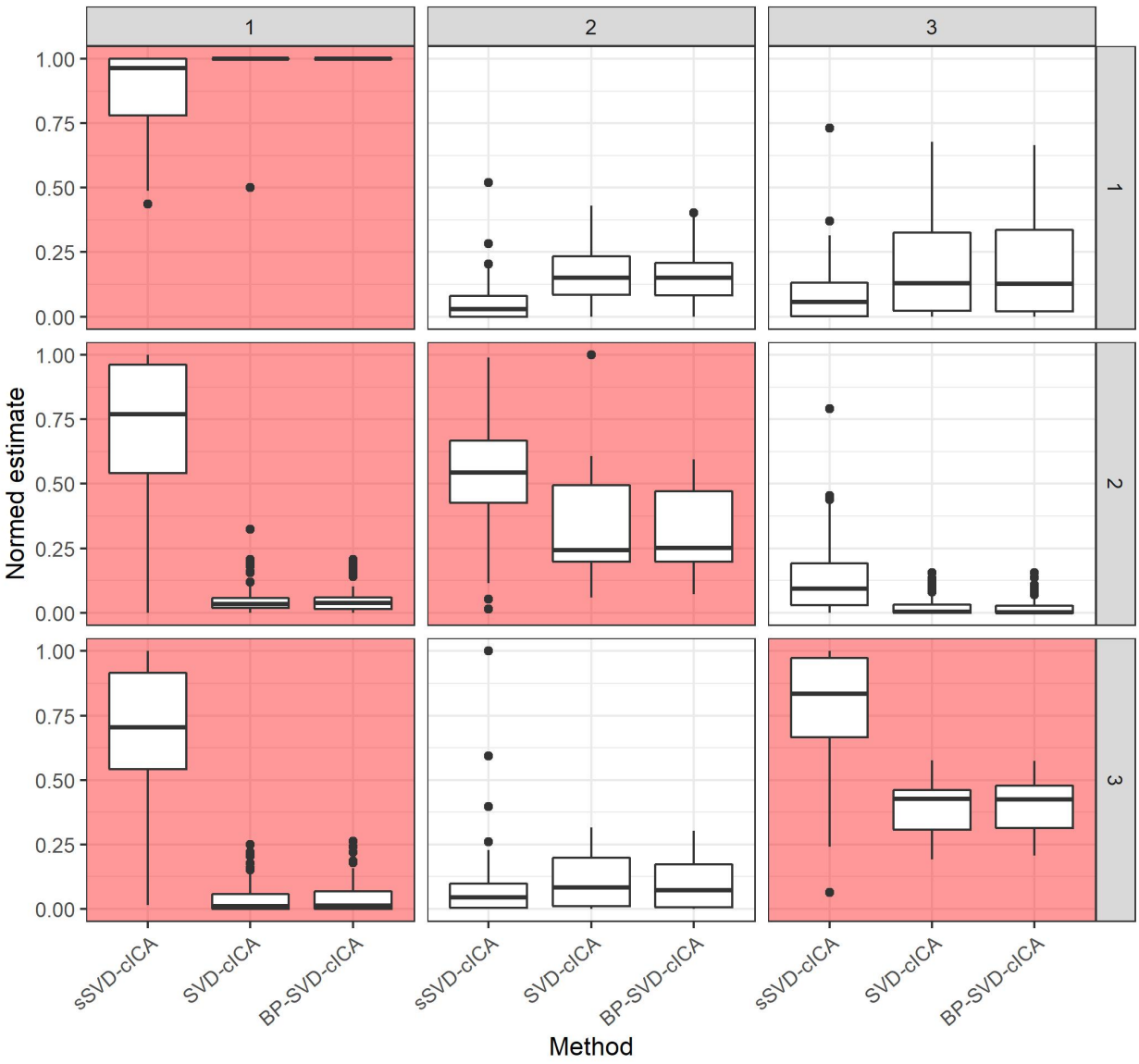

Figure 1.10: Mixing matrix results from the left-hand stimulus simulated data with spikes, across 1000 simulations.

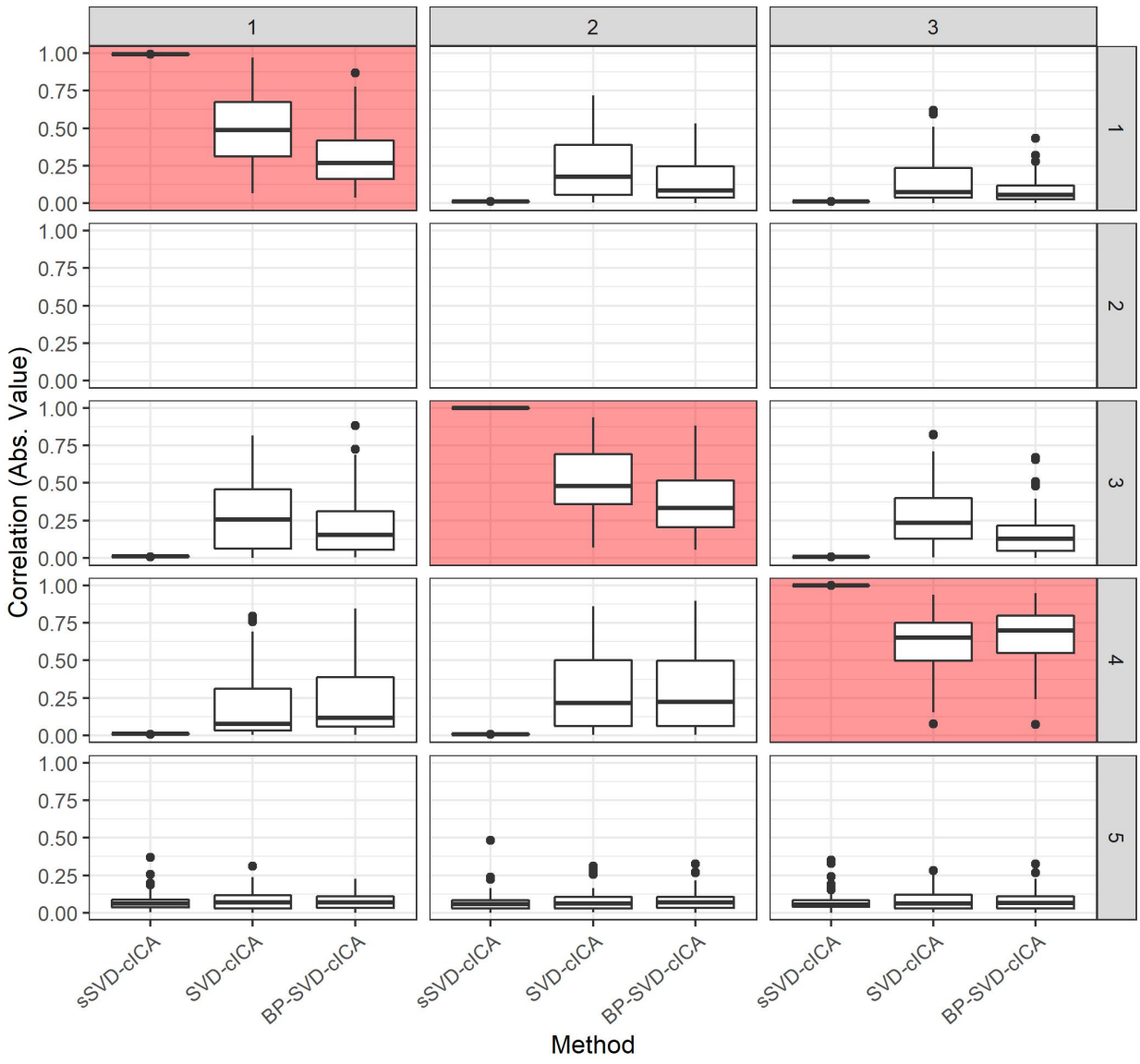

Figure 1.11: Temporal component results from the right-hand stimulus simulated data with spikes, across 1000 simulations.

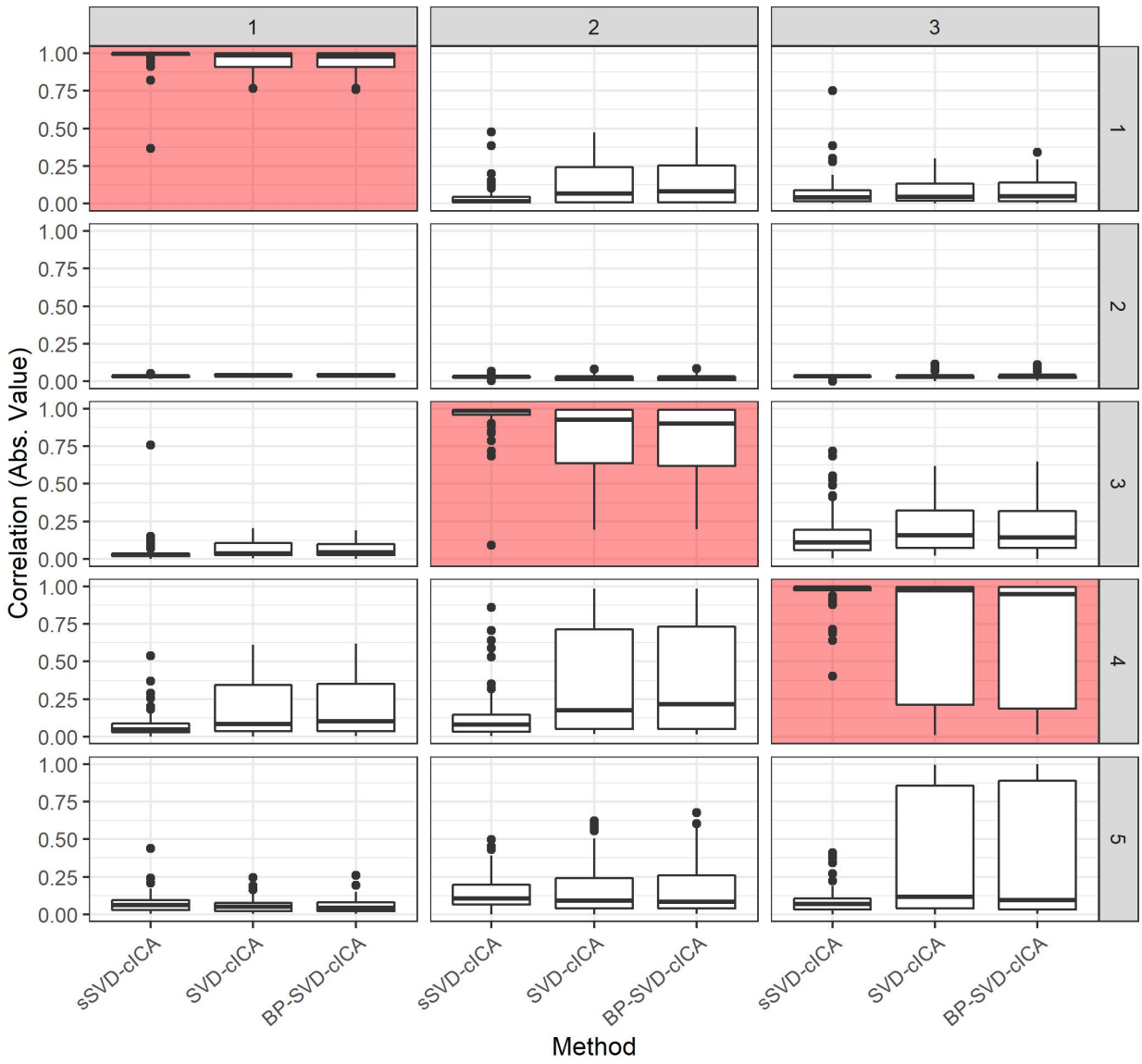

Figure 1.12: Spatial component results from from the right-hand stimulus simulated data with spikes, across 1000 simulations.

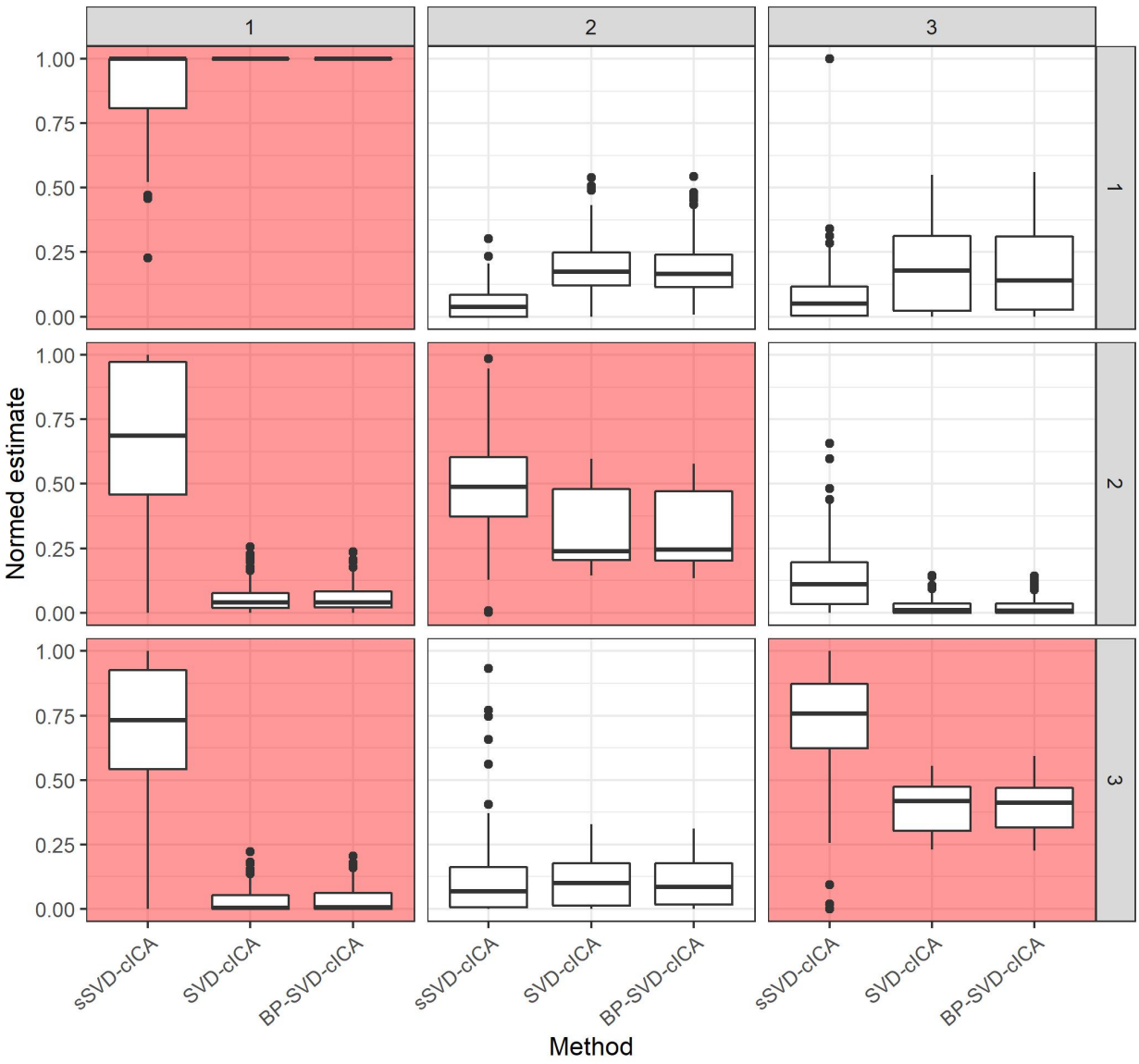

Figure 1.13: Mixing matrix results from from the right-hand stimulus simulated data with spikes, across 1000 simulations.

$$\boldsymbol{A} = \begin{pmatrix} 1 & 0 & 0 & 0 & 0 \\ 0 & 1 & 0 & 0 & 0 \\ 1 & 0 & 1 & 0 & 0 \\ 0 & 1 & 0 & 1 & 0 \\ 0 & 0 & 0 & 0 & 1 \end{pmatrix}$$

These simulated data were analyzed using the proposed methods with the phases specified using the chosen values above. The competing methods also used to analyze the simulated data were the sSVD method without specifying the phases as well as traditional SVD followed by ICA. Colored ICA was again used for all methods when ICA was conducted. Results from a single simulation are shown in Figure 1.15. The results were very similar to the previous simulation study results without spikes; all methods accurately estimated the spatial and temporal components but only the proposed method accurately estimated the mixing matrix. When adding spikes in the same fashion done before, we again see in Figure 1.16 that the proposed method which also specifies the phases was able to accurately estimate the temporal and spatial components as well as the mixing matrix, while the other methods were unable to accurately estimate the mixing matrix or separate the temporal components.

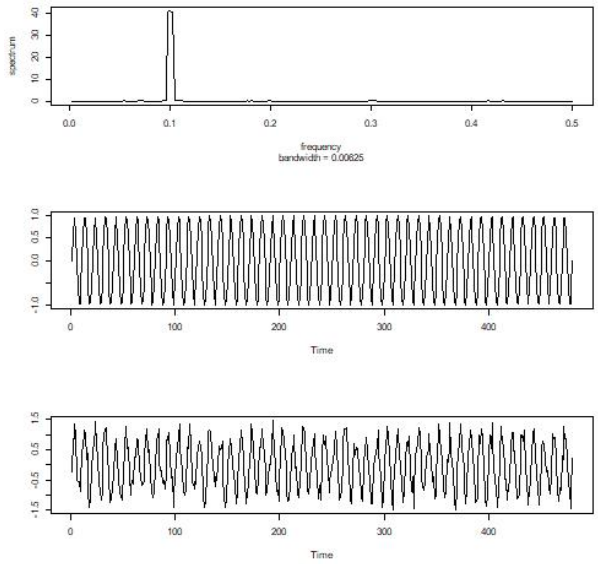

(a) First Component

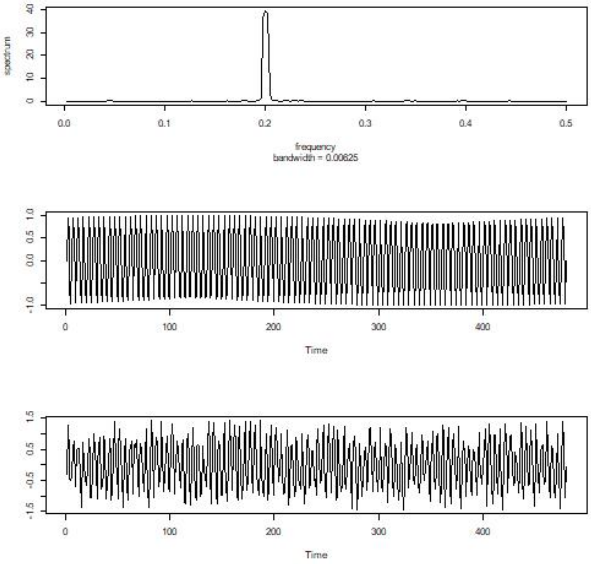

(b) Second Component

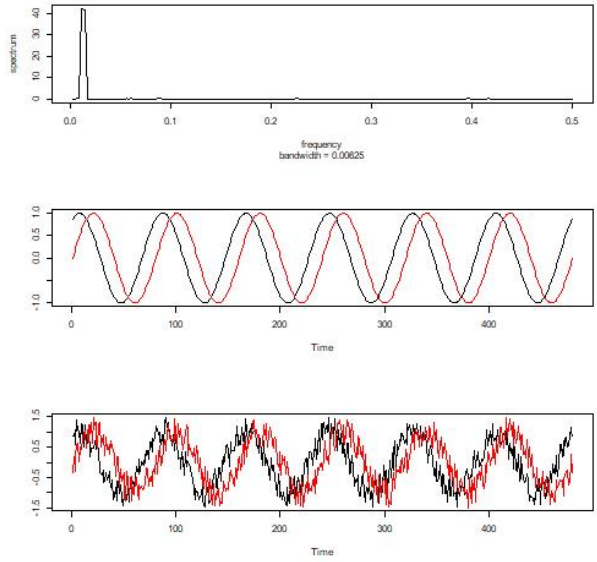

(c) Third and Fourth Component

Figure 1.14: Simulated temporal components for changing phase experiment.

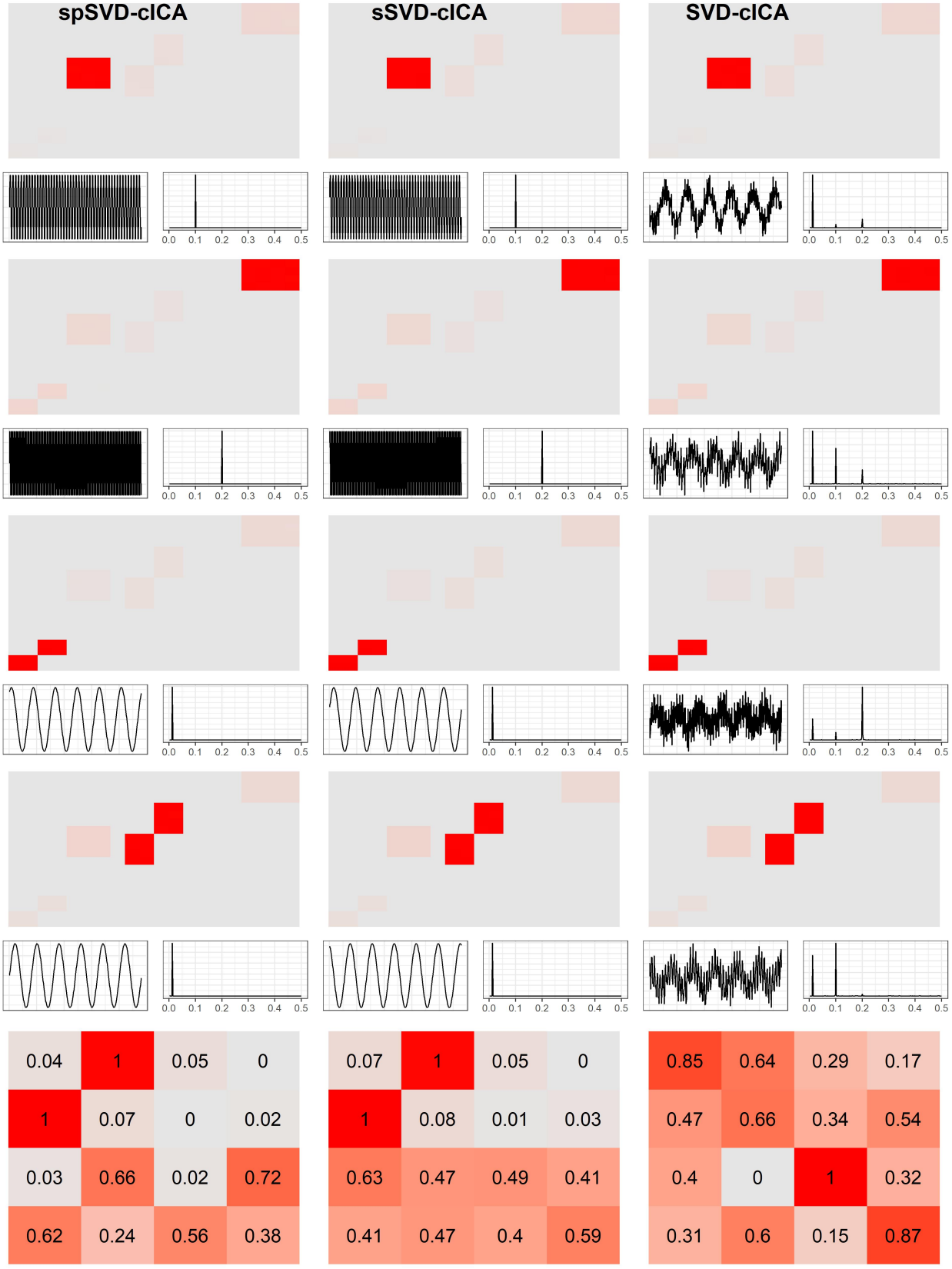

Figure 1.15: Estimation results from changing phase single simulated dataset without spikes.

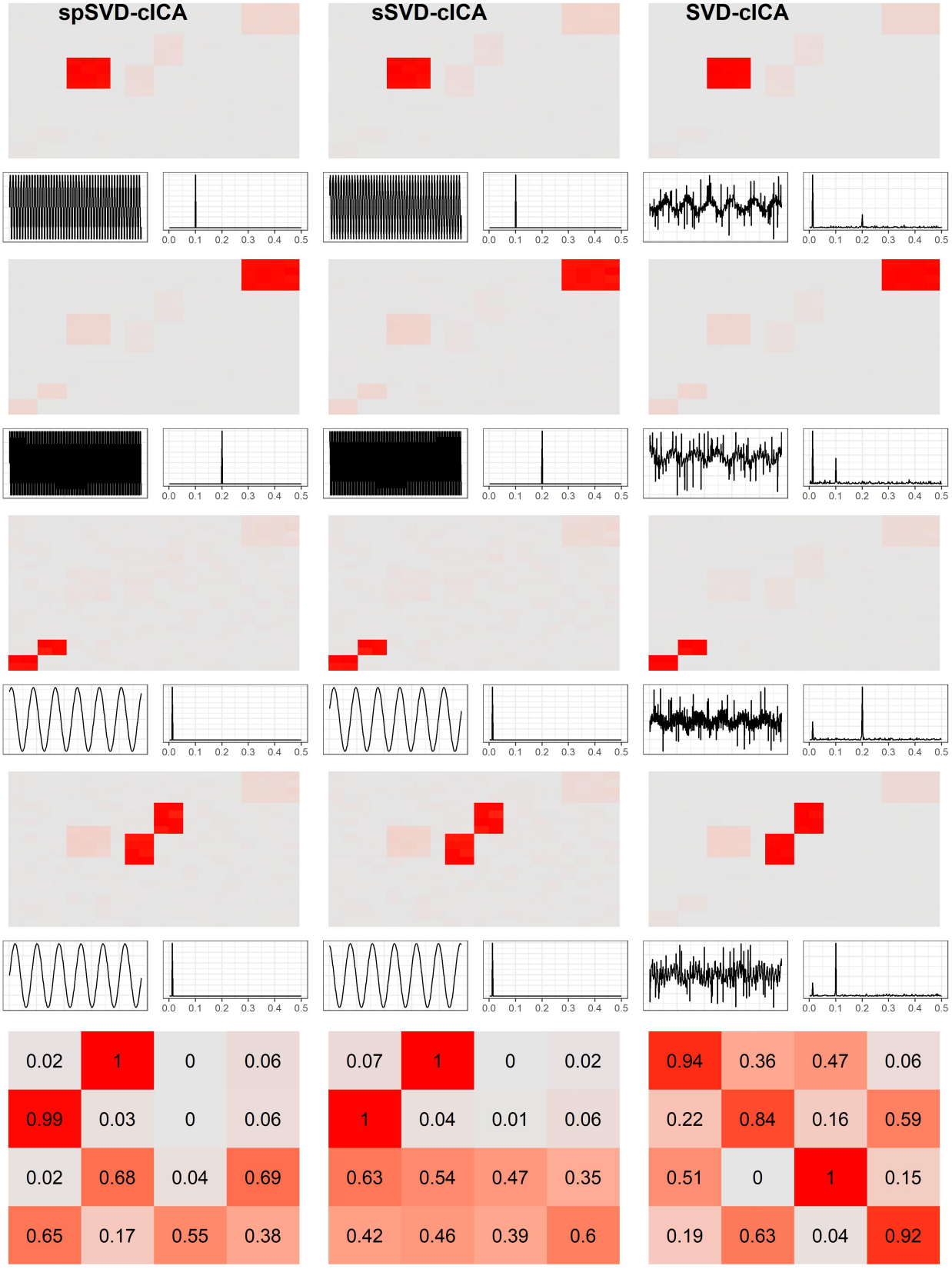

Figure 1.16: Estimation results from changing phase single simulated dataset with spikes.

1.5 Real Data Analysis

The proposed method was used to analyze actual task-based fMRI data from the Midnight Scanning Club (MSC) [Gordon et al., 2020]. The data consists of 3T MRI scans on 10 healthy controls, with 12 sessions done for each of the 10 subjects. These sessions consisted of a variety of study settings, including resting state and task-based. The task-based data was used in the analysis. The task sequence consisted of a block design, with each block denoting a certain stimulus given to the subject for a duration of 15.4 seconds. Rest blocks were interspersed within the task blocks, each of which also lasted 15.4 seconds. These stimuli consisted of a right hand, left hand, left foot, right foot, and tongue stimulus. fMRI data from the first run of the first task session from subject MSC01 was analyzed. The task sequence for this set of data are shown in Figure 1.17. More detail on the MSC data are provided in Gordon et al. [2017].

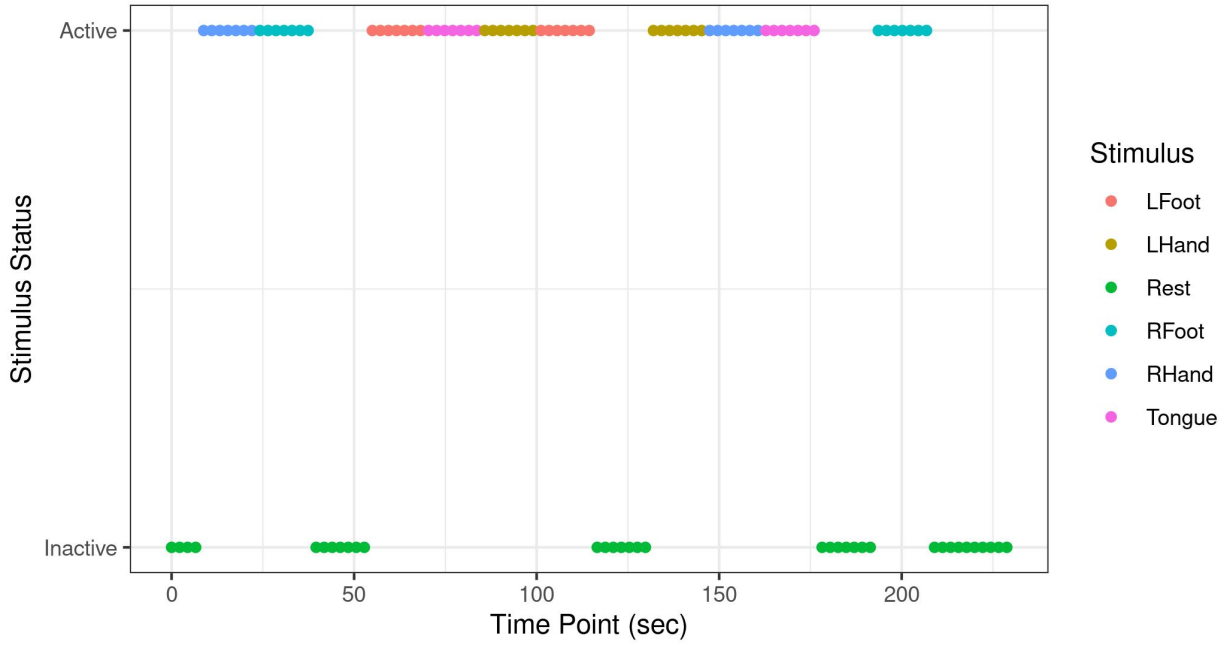

Figure 1.17: Time course of analyzed MSC task-based data.

.

The MSC data is included in a publicly available repository, with the task-based data included in a raw, unprocessed form. The unprocessed task-based data from MSC01 of interest was pre-processed using FSL software version 6.0.4 [Jenkinson et al., 2012]. The pre-processing

steps consisted of 1) motion correction using MCFLIRT, 2) BET brain extraction, 3) spatial smoothing using a Gaussian kernel function with a bandwidth of 5mm, and 4) default FSL high-pass filtering. Then, the fMRI image was registered to the FSL default MNI152 T1 2mm standard space. This was done for the complete fMRI spatio-temporal data for subject MSC01's first run of the first task sequence. To focus on a specific slice, ICA was done on this pre-processed data using MELODIC ICA in FSL. As the bilateral motor activity of primary interest was found in slice 15 in the Z-dimension, this slice from the pre-processed data was extracted to analyze with the proposed method.

In order to create temporal blocks which are approximately harmonic processes, the stimuli of interest were hand (left or right hand), foot (left or right foot) and tongue. The frequency and phase corresponding to these three blocks were estimated from the observed task sequences. The phase was required as all three components had approximately the same frequencies. The frequency for each component was chosen by finding the frequency which maximized the task sequence's raw periodogram. The phase was then estimated visually by matching the corresponding sine wave with the observed task sequence. The corresponding sine waves used to model the task sequences are shown in Figure 1.18.

Using the corresponding frequency and phase for each of the three sequences, the proposed model was fit to the pre-processed data. For comparison, the traditional SVD method used in the simulations (SVD then ICA on the temporal and the spatial SVD matrices) was also used. The estimated temporal and spatial components, as well as the mixing matrix are shown for the two methods are shown in Figures 1.19 and 1.20. The proposed method was able to identify the bilateral activity of interest for two separate components. The mixing matrix identifies spatial components 1 and 2 as having notable between-network connectivity based on the magnitude of the entry in column 1/2 and row 2/1. The traditional SVD method was able also identify bilateral activity, however it also provides less unique components, with components 1 and 3 being very similar and the bilateral activity contained largely in component 2 only. Looking at the temporal components, while components 1 and 2 appear to capture the low frequency task information,

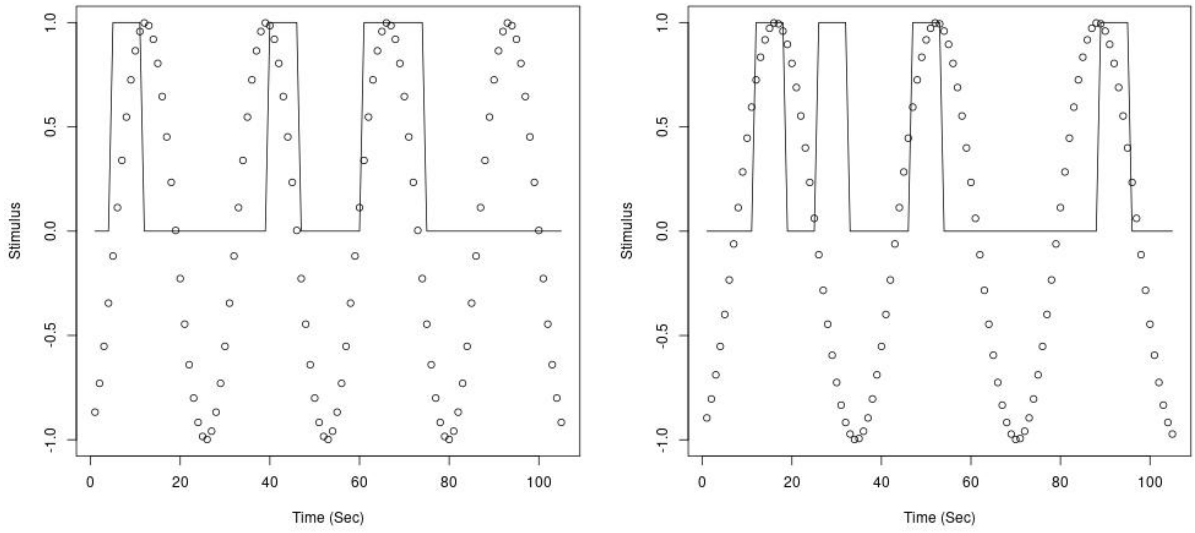

(a) Right Hand

(b) Left Hand

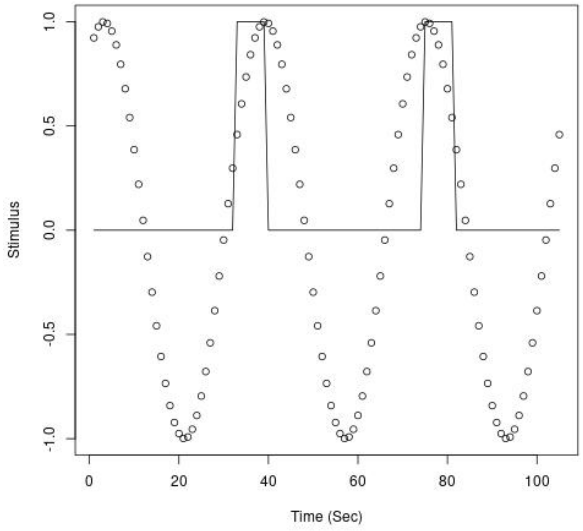

(c) Tongue

Figure 1.18: Sine waves and observed task sequences for each of the three stimulus types analyzed.

component three's interpretation is less clear, with a large amount of high frequency activity which does not reflect any of the task sequences.

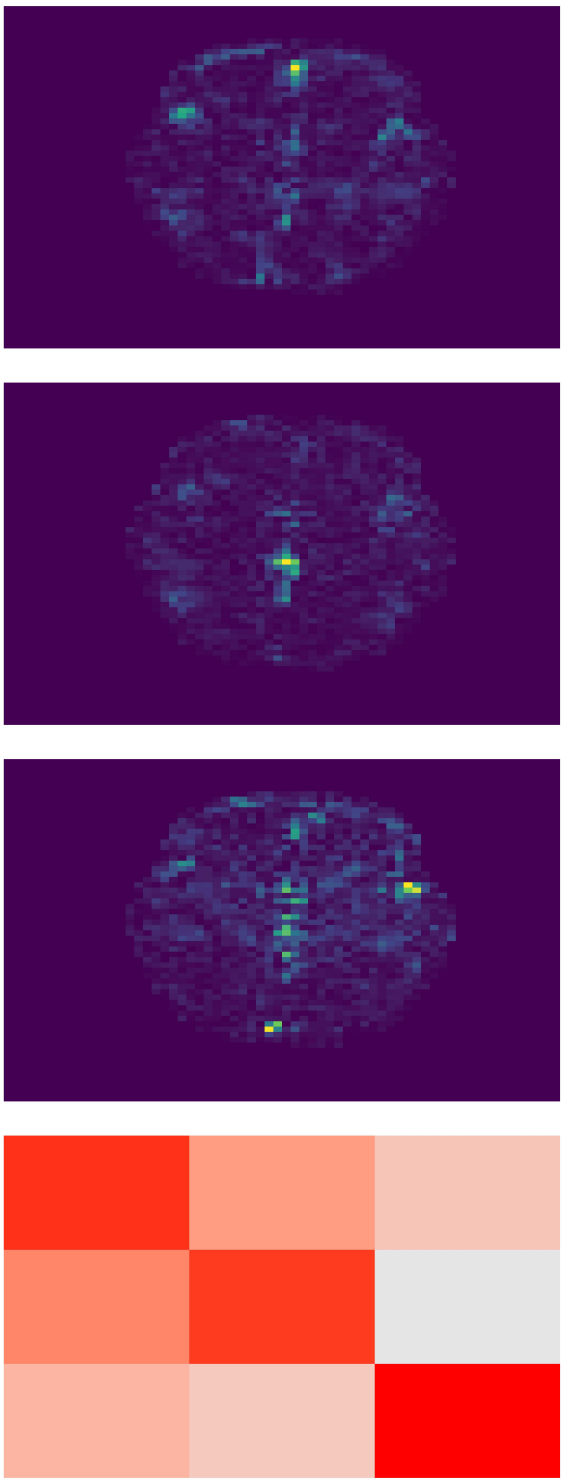

(a) Spatial and Mixing

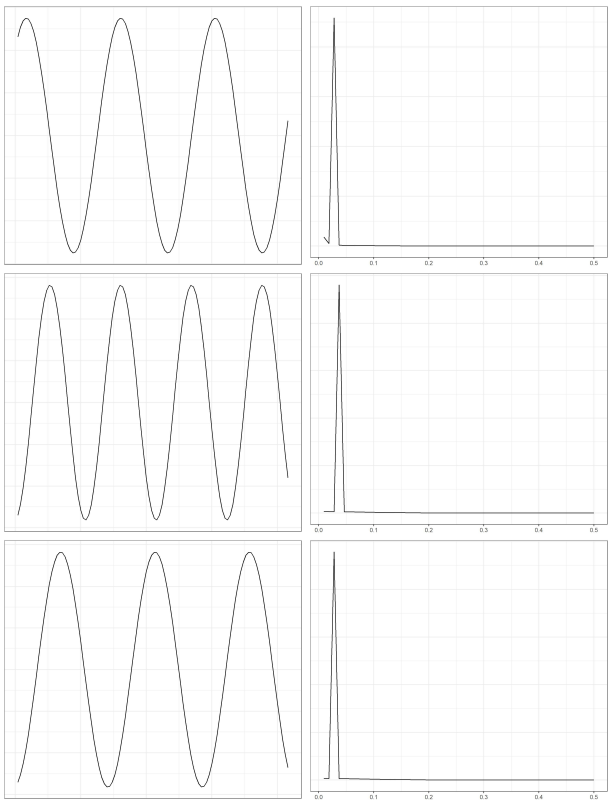

(b) Time

Figure 1.19: Estimated spatial components, mixing matrix, and temporal components from proposed sSVD-cICA method.

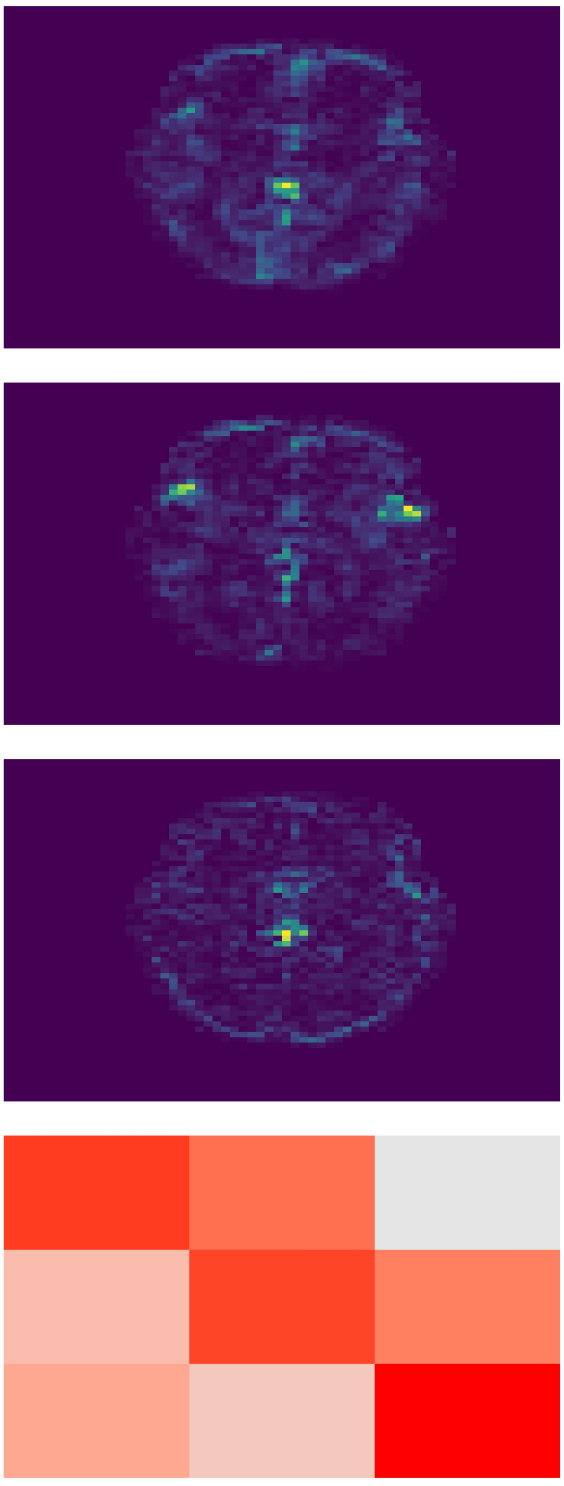

(a) Spatial and Mixing

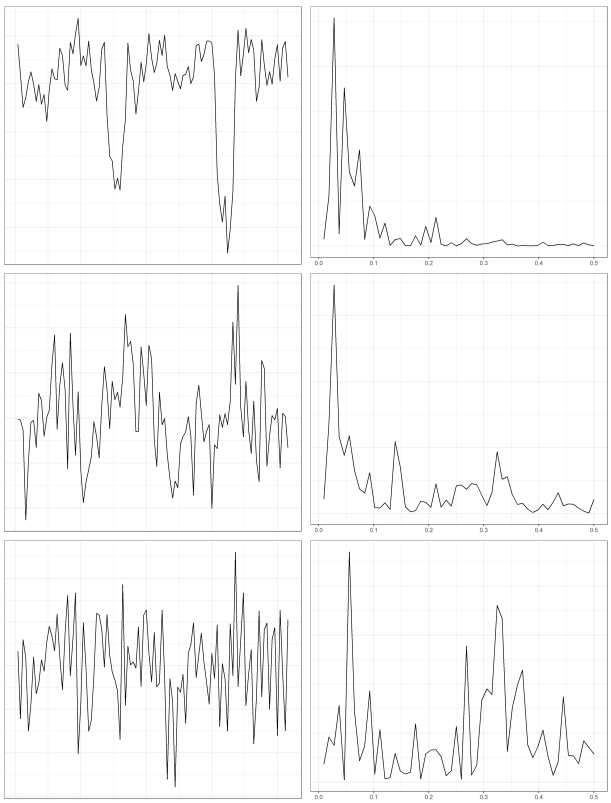

(b) Time

Figure 1.20: Estimated spatial components, mixing matrix, and temporal components from traditional SVD method.

1.6 Discussion

Functional connectivity is a central topic of interest in neuroscience research. When combined with a task-based study design, fMRI imaging can provide insight into which areas of the brain respond to specific stimuli, providing an avenue to assess connectivity. However, connectivity analyses are often limited, either due to the use of pairwise correlations or the use of parametric modeling which may be misspecified. In this work, a flexible model for analyzing function connectivity based on SVD and ICA was presented, where a priori information on the temporal aspects of the data is known. This temporal information is known by design in task-based studies, though it could also be estimated from the data in cases where it is not known (see Bai et al. [2008]). The method's utility was shown in a series of simulation studies which mimic task-based fMRI studies when compared to traditional methods based on SVD and ICA. Then, the method was used to analyze within and between network connectivity using single subject, task-based fMRI data.

There are number of limitations with this method. The main one is the requirement of a priori temporal information on the components of interest, and the use of a single-frequency harmonic process to model the desired temporal components of interest. This is a realistic model for a task-based design in which the stimuli change in blocks and is controlled by the researcher, however it is limiting for more complicated designs (event-based for example) or resting state. This single-frequency restriction could be relaxed using locally-stationary processes in which the frequency changes between specified time intervals [Cohen, 2014]. Modeling the temporal processes using wavelets is another possibility [Radunović, 2009]. Another limitation is that the mixing matrix is fixed across time, with the temporal dynamics of the brain represented by the temporal processes. Allowing this mixing matrix to change over time may better model the dynamics of brain activity. Finally, forcing the mixing matrix to be of full rank in order for it to be estimable is also limiting. Relaxing this restriction in some way may result in a more interpretable model of the between-component connectivity.

CHAPTER 2: ANALYZING CONNECTIVITY IN GENERAL EXPERIMENTAL DESIGNS

2.1 Introduction

Analyzing functional connectivity from neural imaging data is difficult, largely due to low signal to noise ratio (SNR) common in imaging modalities [Rogers et al., 2007, Welvaert and Rosseel, 2013]. Furthermore, connectivity is often dynamic over time and difficult to predict, complicating the design of a realistic and flexible statistical model [Hutchison et al., 2013, Glomb et al., 2017]. While task-based experimental designs can be used to help control this uncertainty in neurological response, more dynamic task designs require models which can capture important characteristics in the brain. Furthermore, study designs which use little to no task sequences, referred to as *resting state*, limit the a priori information available to guide the statistical model used in analysis [Biswal et al., 1995, Honey et al., 2009, Greicius et al., 2009, Fox and Greicius, 2010, Glomb et al., 2017].

In this paper, we develop a model for functional connectivity in general experimental designs (task-based, resting stat, etc.) which is easily interpretable and focuses on removing the temporal and spatial noise from the returned signals. This is done using a combination of a wavelet-based regularized singular value decomposition (SVD) and colored independent component analysis (ICA). The use of regularized SVD extracts the temporal and spatial signals in the data while smoothing them to reduce the noise in the estimation, while ICA is uses to de-mix the components present in the SVD-returned signals. Section 2.2 provides a literature review on connectivity and pre-processing methods used in general experimental designs, Section 2.3 describes the proposed model for connectivity, Section 2.4 provides results from simulation studies evaluat-

ing the proposed method, Section 2.5 provides results from an analysis of resting state data, and Section 2.6 concludes with limitations and discussion.

2.2 Literature Review

Imaging and analyzing brain activity while "at rest" is an important field of research in neuroscience. Studies designed around this goal are often referred to *resting state* studies, and aim to understand the "baseline" or "default" neural activity patterns and structure when the brain is not stimulated by a task. These studies have found evidence of spontaneous fluctuations and activity, broadening the understanding of brain function, with specific areas most active during this resting state [Lee et al., 2013b]. Examples include significant differences between adolescents with Autism Spectrum Disorder and controls in resting state brain activity [Paakki et al., 2010], as well as networks in the brain which are active in infants during sleep [Fransson et al., 2009]. Thus, the development of statistical methodology which are extract these signals of interest from the brain in resting state is of critical importance in neuroscience research.

Due to the lack of a task or stimulus to facilitate the interpretation of the observed brain activity, interpreting results from analyzing resting state data can be challenging. While tying specific regions to physiological responses can be done with task-based designs based on a chosen stimulus, resting state studies lack these external validators. As a result, resting state design can suffer from a large amount of noise and low SNR. This lack of an external stimulus can also make it difficult to determine if observed fluctuations in activity are measures of signal or simply spurious [Griffanti et al., 2016]. This is especially challenging since resting state activity is generally characterized by low frequency fluctuations in the fMRI BOLD signal, which is difficult to identify if buried by high-frequency noise and artifacts [Cole et al., 2010, Lee et al., 2013b, Murphy et al., 2013].

These complications are all present when analyzing functional connectivity in resting state imaging data. Functional connectivity refers to the temporal correlations between neurophysiological events [Friston, 1994], resulting in networks between spatial locations in the brain.

Connectivity analyses are common with resting state data, and have uncovered various spatially-localized brain networks such as the *default mode network* [Roy et al., 2009, Sheline and Raichle, 2013, Yan et al., 2018]. Along with broadening our understanding of the how the brain regulates baseline physiological phenomena, these networks have improved the prediction of various neurological conditions [Meszlényi et al., 2017a, Sripada et al., 2019, Kazeminejad and Sotero, 2019]. Thus, developing data-driven pre-processing and analytic methods for connectivity in resting state studies is critical to better extract these networks of interest from observed images.

Pre-processing methods for resting state connectivity data largely focus on removing artifacts, general de-noising to make signals more visible, and data decomposition models to facilitate interpretable representations of it's inherently high-dimensional nature. Algorithms have been developed to recognize specific types of artifacts commonly present in neural images, such as head motion, and then remove these. Such methods have been shown to substantially improve the analysis of resting state connectivity data [Satterthwaite et al., 2013, Muschelli et al., 2014, Patel et al., 2014]. Many methods to deal with the large amount of general noise present in resting state image data have also been developed, each with their own advantages and limitations [Parkes et al., 2018]. Finally, data decomposition-based methods such as SVD and ICA have shown great promise in creating more interpretable represents of the data, removing artifacts and noise-related components, and reducing the dimension of the image data to a more analytically manageable size [Worsley et al., 2005, Griffanti et al., 2014, Aoki et al., 2015, Parkes et al., 2018]. ICA-based methods are often used in connectivity analyses, due to their ability to de-compose the observed data in a set of temporal or spatial components with a corresponding mixing matrix. This mixing matrix models the noisy combination of these components which, in theory, characterize the observed data. Such components have been shown to match with hypothesized "networks" of brain activity, making ICA a plausible model for analyzing connectivity in resting state data [Cole et al., 2010, Allen et al., 2012, Aoki et al., 2015, Rashid et al., 2016, Du et al., 2017].

While data decomposition can be used to remove artifacts and identify components of interest from the high dimension image, the returned components may still be quite noisy, potentially making interpretation difficult. This is especially with the case with the standard SVD, which has led to a variety of extensions of the method which enforce smoothness and/or sparsity on the returned components in a data-driven manner [Lee et al., 2010, Hong and Lian, 2013, Zhang et al., 2013]. Given the lack of external stimuli in resting state studies and the lack of a priori information, this data-driven structure is very useful with resting state connectivity analyses. As SVD is generally a pre-processing step done with imaging data due to it's high dimension, representing the data with components which are as close as possible to the underlying signals of interest is important for the rest of the analysis pipeline to produce reliable and useful results [Murphy et al., 2013]. Thus, while these extensions have not been applied regularly to resting state imaging data, given their improvement in de-noising the returned components, they may prove fruitful when combined with other methods such as ICA.

When ICA is used to analyze connectivity, due to the independence assumed between the returned components or networks, between-component connectivity is often estimated based on the mixing matrix. For spatial ICA as an example, the returned mixing matrix is composed of time series for each component. Using these time series, correlations are often computed between them as a measure of between-measure connectivity [Joel et al., 2011]. However, this only models connectivity on the temporal level, with spatial connectivity between the components not being modeled directory in the matrix decomposition. Correlation-based measures in general are often used to measure resting state connectivity, including the use of regression modeling [Erdoğan et al., 2016, Murphy and Fox, 2017]. However, this has a number of significant limitations when used in resting state image data. First, region-based correlation or regression analyses generally require a priori specification of locations of the brain to compare (*regions of interest* or ROIs) [Sohn et al., 2015]. Furthermore, if the number of regions is large (voxel-specific for example), multiple comparison correction becomes more important, which can significantly re-

duce power. There is also evidence to suggest that correlation-based measures are not sufficient to represent functional connectivity [Mohanty et al., 2020].

Other methods have also been developed to analyze connectivity in resting state data, though they are largely highly parametric, in contrast to ICA which is data-driven and uses a more relaxed set of assumptions [Friston et al., 2014, Warnick et al., 2018]. Data-driven methods which do not use an matrix decomposition approach have also been developed, specifically when trying to identify temporally dynamic properties of connectivity, using dynamic time warping, the wavelet transform, and coherence [Sun et al., 2004, Ghuman et al., 2011, Eryilmaz et al., 2011, Meszlényi et al., 2017b].

Reproducing results from previous fMRI resting state connectivity studies has sometimes proven difficult [Chou et al., 2012, Choe et al., 2015, Griffanti et al., 2016]. This could be due to a number of factors, include the use of different pre-processing pipelines, large amount of noise inherent to resting state data, or sub-standard analytic methods which generate results with large amounts of variance. Thus, the continued development of integrated pre-processing and analysis pipelines and reliable analytic methods is still needed to improve upon this reproducibility of resting state connectivity findings.

2.3 Proposed Methods

2.3.1 Discrete Wavelet Transform

Let $S(n)$ denote a discrete-time stochastic process where $n = 0, \ldots, N-1$. The Discrete Fourier Transform (DFT) is used to identify frequency components which characterize the observed process. However, the DFT has some notable shortcomings. The first is that the representation is in terms of sinusoidal waves. This representation is limited and may not be an accurate or useful representation for the signal of interest. Further, due to the constant frequency for each component in the representation over the time course ($n = 0, \ldots, N-1$), the DFT cannot accurately represent signals which change their characteristics over time. Estimating the changing frequency components over time is sometimes referred to as *time-frequency analysis*. One ex-

tension of the DFT which is sometimes used for this is the *short-time DFT*. This process is done by first partitioning the time course into intervals where the signal's properties are assumed to be constant, but between which are assumed to possibly change. The DFT is then run separately within each interval using only the signal values inside the interval's time points. However, this partition must be chosen in some fashion and represents discrete changes in the frequency components where this change might be more continuous. Furthermore, the representation is still limited within each interval to a sum of sinusoidal waves.

An alternative to the DFT for time-frequency analysis is the discrete wavelet transform (DWT). A brief summary of the method is detailed here; further details can be found in Radunović [2009]. First, note that the DFT can be represented in matrix form as $\boldsymbol{\phi}(\omega, S) = \boldsymbol{W}S$ where transformation matrix $\boldsymbol{W}$ can be expressed by $\boldsymbol{W} = (\frac{\omega^{jk}}{\sqrt{N}})_{j,k=0,\ldots,N-1}$ where $\omega = \exp(-2\pi i/N)$. The DWT can also be represented by the transformation $\boldsymbol{W}S$, though $\boldsymbol{W}$ will take a different form to allow a more general representation. A DWT is defined by the function used to convolve with the signal $S(n)$ and the corresponding transformation matrix $\boldsymbol{W}$. For the DFT, there was only a single choice of function, $\exp(-ir_k n)$, which from before is a complex sinusoidal wave.

To motivate the DWT, we first discuss the *continuous-time WT* (CWT). In general, a wavelet function $\psi_{a,b}(x)$ is defined by

$$\psi_{a,b}(x) = \frac{1}{\sqrt{a}}\psi\Big(\frac{x-b}{a}\Big), a > 0$$

where $\psi(x)$ is a referred to as the *mother wavelet*. The scaling (by a) and translation (by b) of the mother wavelet defines the function. There are various forms of $\psi(x)$ that have been developed, all with the characteristics of $\int_{-\infty}^{\infty} |\psi(x)|dx < \infty$, $\int_{-\infty}^{\infty} \psi(x)dx = 0$ and $\int_{-\infty}^{\infty} |\psi(x)|^2 dx = 1$, along with a compact support. The parameters a and b determine the ability of the wavelet to identify areas of the signal with sharp, brief peaks (requiring a high temporal resolution to identify due to the frequent changes) as well as areas smooth across time (can be identified with

a lower resolution). This often referred to as *multi-resolution analysis*. Examples of frequently-used mother wavelets are shown in Figure 2.1 [Lin et al., 2013].

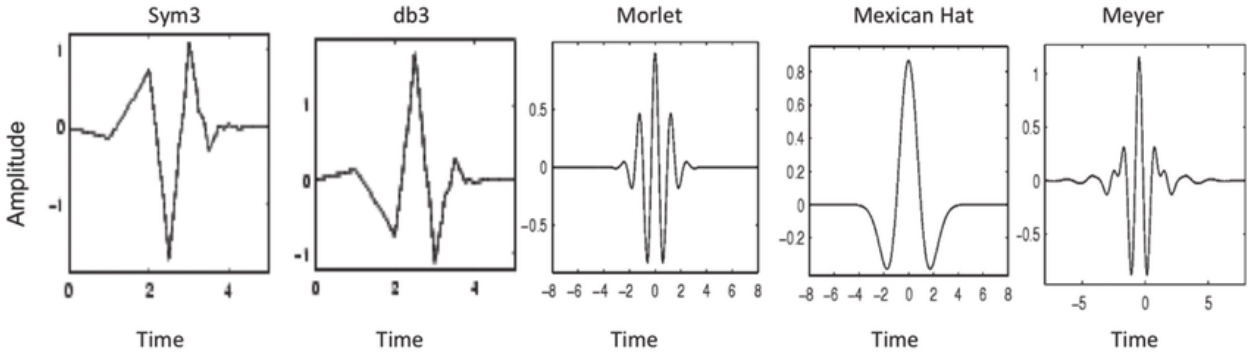

Figure 2.1: Examples of frequently-used mother wavelets in multi-resolution analysis.

.

To transform signal $S(t)$ to the frequency domain, it is convolved with the wavelet function, resulting in the CWT

$$CWT_S(a,b) =< S, \psi_{a,b} >= \frac{1}{\sqrt{a}} \int_{-\infty}^{\infty} S(t) \overline{\psi\Big(\frac{t-b}{a}\Big)} dt$$

where $< x, y >$ denotes the inner product and $\overline{x}$ denotes the complex conjugate.

When used with observed data, since only a discrete set of time points are observed, the DWT is used. With the DWT, a discrete set of scaling and translation parameter values are chosen, using the wavelet function

$$\psi_{j,k}(x) = \frac{1}{\sqrt{a_0^j}} \psi\left(\frac{x - k b_0 a_0^j}{a_0^j}\right), a_0 > 0$$

with $a_0 = 2$ and $b_0 = 1$ commonly used. Parameter a_0 controls the division of the frequency axis (scaling) and b_0 controls the division of the time axis (shifting). This results in

$$\psi_{j,k}(x) = 2^{-j/2} \psi(2^{-j}x - k), \text{ where } \psi_{j,k}(x) \neq 0 \text{ for } x \in [2^j k, 2^j(k+1)] \tag{2.1}$$

creating a time-frequency analysis. The DWT is then defined by

$$DWT_S(j,k) =< S, \psi_{j,k} >= 2^{-j/2} \int_{-\infty}^{\infty} S(t)\overline{\psi(2^{-j}t - k)}dt$$

with various algorithms designed to compute the integral for a discrete signal. For example, the fast wavelet transform (FWT) can be represented by a linear transformation through the matrix $\boldsymbol{W}$ multiplied by observed signal $S(t)$ as a vector. Matrix $\boldsymbol{W}$ depends on the chosen mother wavelet.

Along with multi-resolution analysis, the DWT can also be used as a representation of the time series in the *frequency* domain, instead of the usual time domain. The result of the DWT, when applied as a linear transformation, is a vector of length N, denoted here by $b = \boldsymbol{W}S$, where $\boldsymbol{W}$ is the chosen DWT matrix based on the chosen wavelet function. The inverse transform is denoted by $S = \boldsymbol{W}^{-1}b$, as the DWT matrix is invertible. *Smooth* processes can be represented by a *sparse* DWT (i.e. many of entries in b equal to 0, see Figure 2.2). Thus, DWT can also be used to more easily smooth a noisy process, by making the DWT sparse instead of working with the process in the time domain.

2.3.2 Wavelet-Based Regularized Singular Value Decomposition

When applied to noisy data, the components returned by traditional SVD are often very noisy as well, even if the signal in the data is smooth [Bai et al., 2008, Hong and Lian, 2013, Zhang et al., 2013]. Supervised SVD methods are one way to extract smooth components which may be more representative of the underlying signals of interest [Bai et al., 2008, Li et al., 2016]. These methods could be easily extended or applied to a model in which the frequency is allowed to change at set time points, allowing more dynamic temporal signals to be extracted. While this may be appropriate for simple task-based experiments or physiological processes, more complicated experiments and neural activity may not correspond to such a model. Futhermore, the supervised nature of these methods requires that the frequencies within the components of

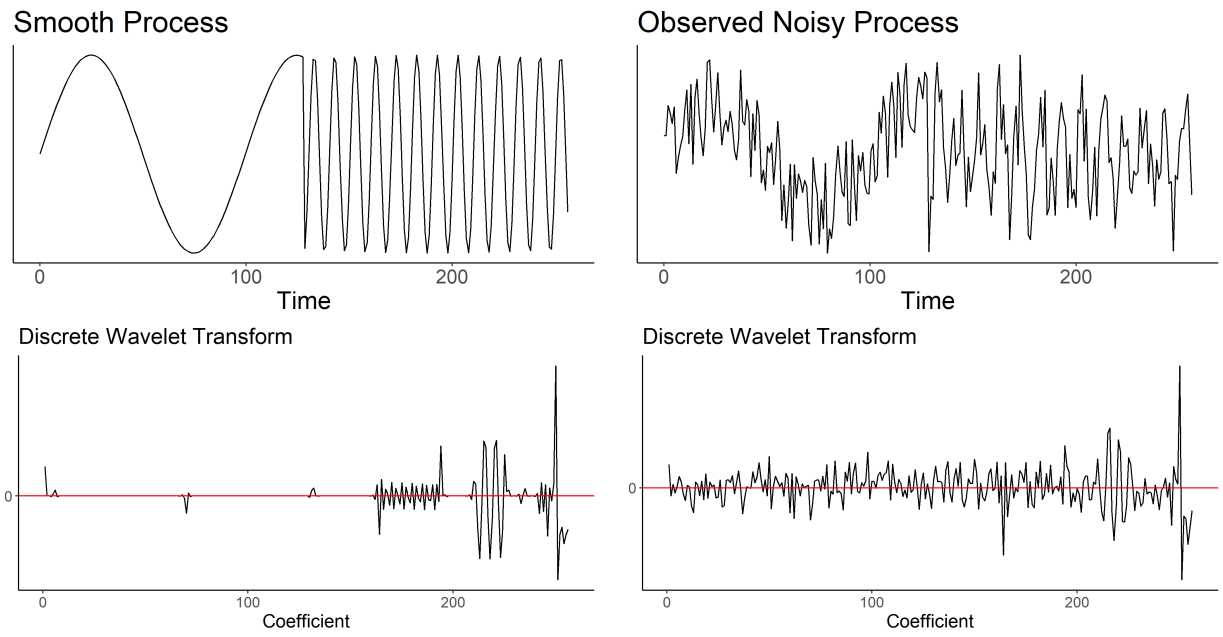

Figure 2.2: Example of DWT for a smooth process and process with additive noise.

.

interest be known a priori. These may not be known for neural activity of interest, especially for resting state data. There is concern with the interpretability of results from resting state data due to the lack of an external stimulus to help separate physiologically-based neural activity from noise [Buckner et al., 2013]. However, given the prevalence of these types of studies with fMRI data as well as the constrained model used with the described SVD procedure, a more data-driven alternative would be useful.

Hong and Lian [2013] developed an extension to SVD for use with noisy spatio-temporal data which identifies components in a data-driven way. For observed data $\boldsymbol{X}$, SVD factorizes the data as $\boldsymbol{X} = \boldsymbol{V}\boldsymbol{D}\boldsymbol{U}^T$. Since $\boldsymbol{D} = \text{Diag}(d_1, \ldots, d_R)$, the decomposition can be expressed by

$$\boldsymbol{X} = \sum_{k=1}^{R} d_k v_k {u_k}^T$$

For a single component, the SVD estimation procedure is defined by the solution to equation

$$\min_{v,u} ||\boldsymbol{X} - vu^T||^2.$$

Regularized SVD is an extension to this formulation, in which penalty terms are used to force smoothness to the components. The optimization problem when introducing regularization becomes $\min_{v,u} Q_1(v, u; \boldsymbol{X})$ where

$$Q_1(v, u; \boldsymbol{X}) = ||\boldsymbol{X} - vu^T||^2 + \lambda_1 v^T \tilde{\boldsymbol{\Omega}} v||u||^2 + \lambda_2 ||v||^2 u^T \tilde{\boldsymbol{\Omega}} u + \lambda_1 \lambda_2 v^T \tilde{\boldsymbol{\Omega}} v u^T \tilde{\boldsymbol{\Omega}} u$$

where λ_1 and λ_2 are regularization parameters and $\tilde{\boldsymbol{\Omega}}$ is a penalty matrix which all encourage smoothness of u and v. These parameters are manually chosen, for example $\tilde{\boldsymbol{\Omega}}$ such that $v^T \tilde{\boldsymbol{\Omega}} v = \sum_{i=2}^{M-1} (v_{i+1} + v_{i-1} - 2u_i)^2$ (and similar for $u^T \tilde{\boldsymbol{\Omega}} u$). While this may be appropriate for temporal components, spatial components may be more sparse then smooth, with specific areas being "inactive".

A second extension to the standard SVD formulation is *sparse SVD*, where the optimization problem instead becomes $\min_{s,||v||=1,||u||=1} Q_2(d, v, u; \boldsymbol{X})$ where

$$Q_2(d, v, u; \boldsymbol{X}) = ||\boldsymbol{X} - dvu^T||^2 + \lambda_1 \sum_{i=1}^{M} |v_i| + \lambda_2 \sum_{j=1}^{N} |v_j|$$

where λ_1 and λ_2 are penalty terms which enforce sparsity on v and u respectively. This sparsity is used to create a component with entries of small magnitude being forced to zero. While this may be appropriate for spatial components where certain areas may be inactive, sparse temporal components are likely not appropriate for temporal components. This is because temporal components, especially in relation to brain activity, are generally smooth and have rhythmic aspects to their behavior Bai et al. [2008].

Building from these extensions, Hong and Lian [2013] developed *penalized SVD* (PSVD), in which the optimization problem becomes $\min_{v,u} Q_3(v, u; \boldsymbol{X})$ where

$$Q_3 = ||\boldsymbol{X} - vu^T||^2 + \lambda_1 P_1(v) + \lambda_2 P_2(v) \tag{2.2}$$

with $P_1(v) = \sum_{i=1}^{M} |v_i|$ and $P_2(u) = {u_1}^2 + \sum_{j=2}^{N-1}(u_{j+1} - 2u_j + u_{j-1})^2 + {u_N}^2$. In all formulations $\lambda_1 > 0$ and $\lambda_2 > 0$. The authors proposed the following optimizers to extract v and u

$$v = \arg\min_{v} ||\boldsymbol{X} - vu^T||^2 + \lambda_1 P_1(v)$$
$$u = \arg\min_{u} ||\boldsymbol{X} - vu^T||^2 + \lambda_2 P_2(u)$$

For penalized SVD, a wavelet function is used as a basis for u. That is, let $b = \boldsymbol{W}u$ be a discrete wavelet transform of u where $\boldsymbol{W}$ is the discrete orthogonal wavelet transform matrix corresponding to a chosen wavelet basis of $L_2([0, 1])$. Then by orthogonality, u is represented by the inverse wavelet transform, $u = \boldsymbol{W}^T b$. This results in the objective function

$$Q_3 = ||\boldsymbol{X} - v(\boldsymbol{W}^T b)^T||^2 + \lambda_1 P_1(v) + \lambda_2 P_2(b) \tag{2.3}$$

with the corresponding optimizer where $P_1(v) = \sum_i |v_i|$ and $P_2(b) = \sum_j |b_j|$. This results in the components given by the solution to

$$(v, b) = \arg\min_{v,b} ||\boldsymbol{X} - v(\boldsymbol{W}^T b)^T||^2 + \lambda_1 \sum_i |v_i| + \lambda_2 \sum_j |b_j| \tag{2.4}$$

where u can be easily solved for using the specified inverse wavelet transform.

The use of the l_1 penalty is used to enforce sparsity on the wavelet representation of the component, also resulting in the smoothing of the wavelet by shrinking a subset of the wavelet coefficients to 0. That is, smoothing of the component is done in the wavelet domain (that is, after transformation) instead of the original (in this case, temporal) domain. As a result, sparsity is enforced on v while smoothness (and not sparsity) is enforced on u due to working in the wavelet domain. This allows for the temporal components of the data to be estimated in a flexible and smooth manner with minimal assumptions placed on its structure, due to the generality of the wavelet representation.

2.3.3 Modeling Connectivity

Let $\boldsymbol{X}$ denote the T by V matrix of voxel-specific time-series of fMRI BOLD signals. In this section, we assume $\boldsymbol{X}$ represents fMRI data, however any spatio-temporal data matrix for which connectivity is of interest may be substituted (for example, EEG data). Assume $\boldsymbol{X}$ can be represented by

$$\boldsymbol{X} = \boldsymbol{U}\boldsymbol{A}\boldsymbol{S}$$

where $\boldsymbol{U} = [U_1, \ldots, U_R]$ is a T by R matrix with columns composed of temporal realizations, $\boldsymbol{A}$ is a R by R matrix and $\boldsymbol{S} = [S_1, \ldots, S_R]^T$ is a matrix with rows composed of spatial realizations with $S_i \perp S_j$ for $i, j = 1, \ldots, R$ and $i \neq j$. From the usual spatial ICA model, $\boldsymbol{A}$ is the mixing matrix and $\boldsymbol{S}$ is the matrix of IC realizations, in this case spatial.

Since $\boldsymbol{A}$ is embedded between both the temporal components in $\boldsymbol{U}$ and spatial components in $\boldsymbol{S}$, traditional two-matrix decomposition tools such as ICA, SVD, and PCA will extract temporal and components contaminated by $\boldsymbol{A}$. This makes $\boldsymbol{A}$ difficult to separate with these methods. Thus, the model estimation procedure is iterative, combining the use of SVD and ICA to estimate all three matrix components.

The temporal components are separated first. To reflect noise in the observe data $\boldsymbol{X}$, we assume $\boldsymbol{U}$ contains temporal components which are a combination of a smooth signal and additive noise. That is, for $i = 1, \ldots, R$, $U_i = \tilde{U}_i + \epsilon_i$ where ϵ_i is a mean-zero, non-Gaussian process and $\tilde{U}_i$ is a fixed and smooth function of time. For $\boldsymbol{A}$, we assume it is of full-rank so that the model is identifiable. Finally, we assume $\boldsymbol{S}$ has a sparse structure of an arbitrary degree (i.e., at least 1 entry is zero).

Following these assumptions, we first separate the temporal component matrix $\boldsymbol{U}$, with the goal of accurately estimating signal $\tilde{\boldsymbol{U}} = [\tilde{U}_1, \ldots, \tilde{U}_r]$. The first step is to identify smoothed estimates of the temporal components in $\boldsymbol{X}$. To do this, we begin with SVD of observed data $\boldsymbol{X}$, denoted by

$$\boldsymbol{X} = \boldsymbol{U_0 D_0 V_0}$$

which provides a noisy initial spatio-temporal decomposition of the data. Matrix $\boldsymbol{U_0 D_0}$ contains the noisy and mixed temporal components in the data. To smooth these, the wavelet-based penalized SVD in Section 2.3.2 is used, with $\lambda_1 = 1$ and λ_2 chosen using BIC with a grid search, as used by Hong and Lian [2013]. The result is denoted by

$$\boldsymbol{U_0 D_0} = \tilde{\boldsymbol{U}}_\mathbf{0} \tilde{\boldsymbol{V}}_\mathbf{0}$$

with BIC defined by

$$BIC = \frac{||\boldsymbol{U_0 D_0} - \tilde{\boldsymbol{U}}_\mathbf{0} \tilde{\boldsymbol{V}}_\mathbf{0}||^2}{T * R * \hat{\sigma}^2} + \frac{\log(T * R)}{T * R} \hat{df}(\lambda_2)$$

as used by Lee et al. [2010] for their sparse SVD method. Finally, ICA is used to de-mix the temporal components present in $\tilde{U}_0$, followed by penalized SVD to additionally smooth the ICA-returned separate temporal components

$\tilde{\boldsymbol{U}}_\mathbf{0} = \boldsymbol{A}_{\hat{\boldsymbol{U}}} \hat{\boldsymbol{U}}$ estimate returned by ICA

$\hat{\boldsymbol{U}} = \hat{\tilde{\boldsymbol{U}}} \boldsymbol{V}_{\hat{\boldsymbol{U}}}$ smoothed estimate returned by PSVD.

with $\boldsymbol{V}_{\hat{\boldsymbol{U}}}$ discarded and $\hat{\tilde{\boldsymbol{U}}}$ as the estimate of the temporal component signals in $\tilde{\boldsymbol{U}}$.

To estimate the mixing matrix and spatial components. Penalized SVD is used, with the temporal matrix fixed at the pre-smoothed estimate $\hat{\boldsymbol{U}}$, $\lambda_2 = 1$ and λ_1 selected using BIC with the above definition with V instead of R (using $\hat{df}(\lambda_1)$).

$$\boldsymbol{X} = \hat{\boldsymbol{U}} \hat{\boldsymbol{V}}$$

The fixing of the temporal matrix is required in order for $\boldsymbol{A}$ to be estimable (as ICA has now separated out the mixed temporal components). This results in the extraction of the mixed, sparse spatial components in the data, contained in $\hat{\boldsymbol{V}}$. Finally, these spatial components are de-mixed using ICA, resulting in

$$\hat{\boldsymbol{V}} = \hat{\boldsymbol{A}}\hat{\boldsymbol{S}}.$$

$\hat{\boldsymbol{U}}, \hat{\tilde{\boldsymbol{U}}}, \hat{\boldsymbol{A}}$, and $\hat{\boldsymbol{S}}$ serve as estimates of $\boldsymbol{U}, \tilde{\boldsymbol{U}}, \boldsymbol{A}$, and $\boldsymbol{S}$ respectively. These steps are summarized in Figure 2.3. The top row describes the process to extract smooth temporal processes; bottom describes the process to extract spatial processes and mixing matrix

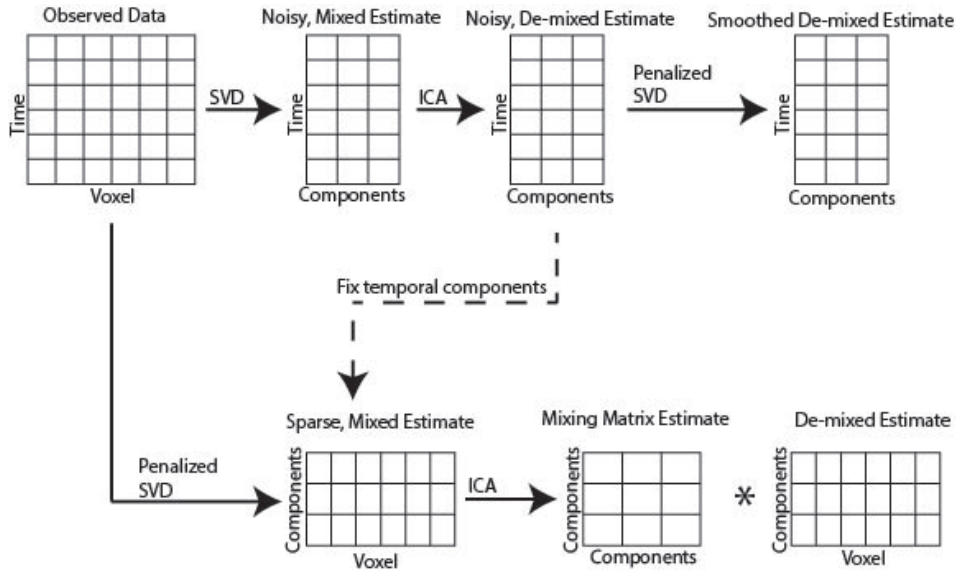

Figure 2.3: Proposed method for connectivity analysis with neural imaging data.

.

2.4 Simulated Data Analysis

To assess the accuracy of the decomposition method proposed in Section 2.3.3, we applied it to simulated spatio-temporal data. We attempt to mimic general experimental design, allowing some temporal component to change their characteristics over the time course. Denote the T by V observed data by $\boldsymbol{X}$. The temporal components of the data are contained in the columns of

$\boldsymbol{U} = [U_1, \ldots, U_R]$ where $R = 5$. For $i = 1, \ldots, 5, U_i = [U_i(1), \ldots, U_i(T)]^T$ where $T = 256$, representing the large temporal dimension generally present in imaging data. A length of 256 was also chosen as it is a power of 2, which is required for the DWT (otherwise, would need to zeropad the data or some other transformation).

The first and second components, U_1 and U_2, were generated as harmonic processes with a single frequency over the entire time course as the signal. Additive noise was included, generated from a Uniform$[-\delta, \delta]$ for $\delta > 0$, with

$$U_1(t) = \sin(2\pi * 0.3t) + \epsilon_1(t)$$

and

$$U_2(t) = \sin(2\pi * 0.4t) + \epsilon_2(t)$$

for $t = 1, \ldots, 256$ with ϵ_i denoting the additive noise for $i = 1, 2$. For the third and fourth components, U_3 and U_4, harmonics with changing frequencies over time were used to represent the dynamic nature of neural activity in resting state or other general imaging study designs. There were defined as

$$U_3(t) = \begin{cases} \sin(2\pi * 0.01t) + \epsilon_3(t) & 1 \leq t \leq 128 \\ \sin(2\pi * 0.1t) + \epsilon_3(t) & t > 128 \end{cases}$$

and

$$U_4(t) = \begin{cases} \sin(2\pi * 0.05t) + \epsilon_4(t) & 1 \leq t \leq 128 \\ \sin(2\pi * 0.2t) + \epsilon_4(t) & t > 128 \end{cases}$$

for $t = 1, \ldots, 256$ with ϵ_i denoting the additive noise for $i = 3, 4$. The fifth temporal component, U_5, was pure noise, generated as T independent values from Uniform$[-1, 1]$. The high range for this noise component was chosen to reflect the potentially high amount of noise often present in imaging datasets. The temporal processes from a single simulation with $\delta = 0.5$ are shown

in Figure 2.4. For each of the first four components, the following are provided (from top to bottom): smoothed periodogram, signal component, component realizations (signal plus noise). The signal temporal components of interest, denoted by $\tilde{\boldsymbol{U}} = [\tilde{U}_1, \ldots, \tilde{U}_4]$ are

$$\tilde{U}_1(t) = \sin(2\pi * 0.3t)$$

$$\tilde{U}_2(t) = \sin(2\pi * 0.4t)$$

$$\tilde{U}_3(t) = \begin{cases} \sin(2\pi * 0.01t) & 1 \leq t \leq 128 \\ \sin(2\pi * 0.1t) & t > 128 \end{cases}$$

and

$$\tilde{U}_4(t) = \begin{cases} \sin(2\pi * 0.05t) & 1 \leq t \leq 128 \\ \sin(2\pi * 0.2t) & t > 128 \end{cases}$$

The first four spatial components ($S_1, \ldots, S_4$) were sparse processes representing localized activation of various parts of the brain. Figure 2.5 visualizes the realized values for each of these four spatial components, from one of the simulations. No noise was added to these processes. The fifth spatial component, S_5, was pure noise, generated as V independent values from Normal[0, 0.1].

To represent between-component spatial connectivity, 5 by 5 mixing matrix $\boldsymbol{A}$ was generated with entries equal to 0 (component deactivated) or 1 (component activated). Values for the entries were selected to represent components 1 and 2 acting on their own, with components 3 and 4 connected to components 1 and 2 respectively. The last row of the matrix indicates that the noise component is not connected with either of the first 4.

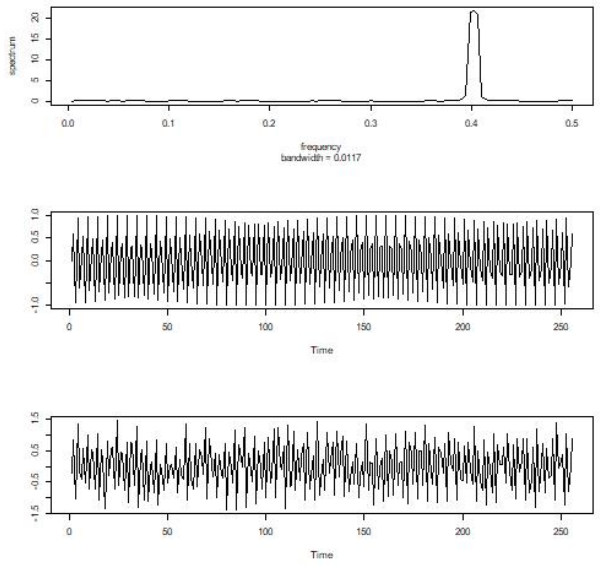

(a) Component 1

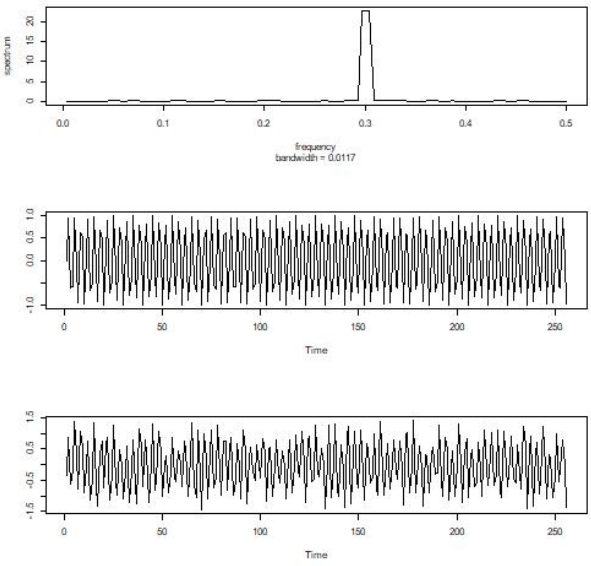

(b) Component 2

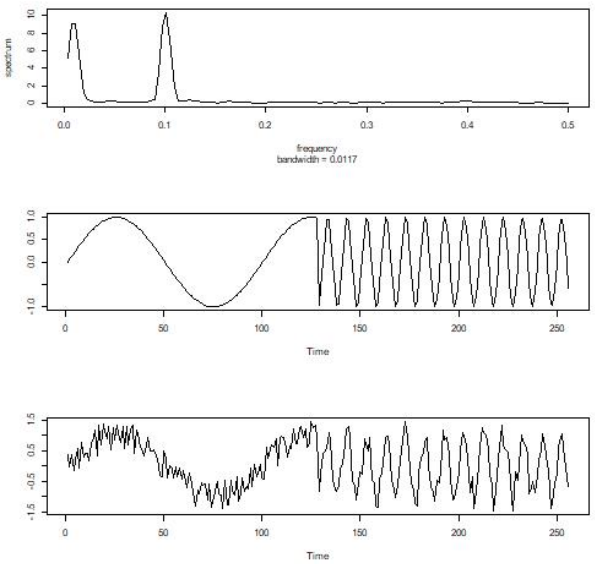

(c) Component 3

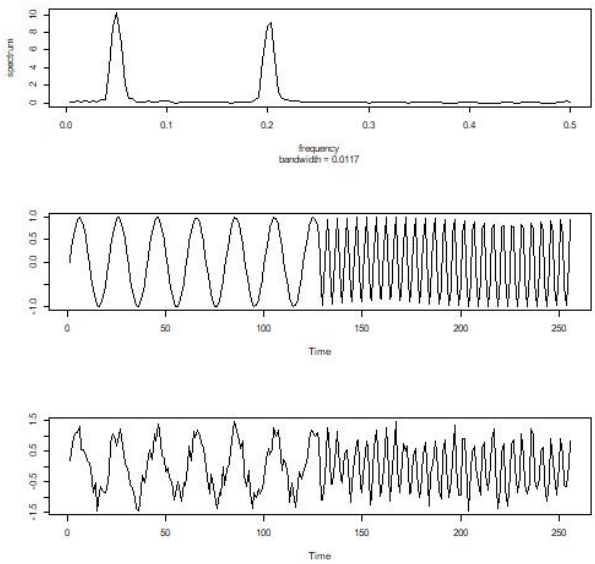

(d) Component 4

Figure 2.4: Temporal components from single simulation with $\delta = 0.5$.

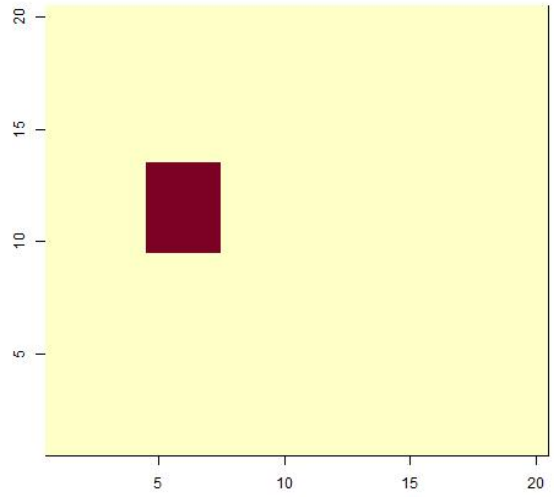

(a) Component 1

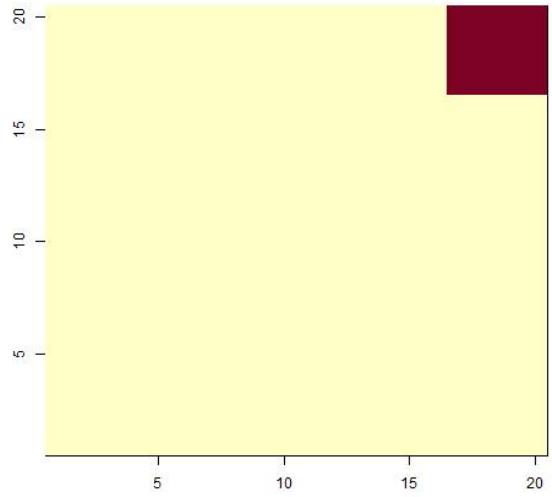

(b) Component 2

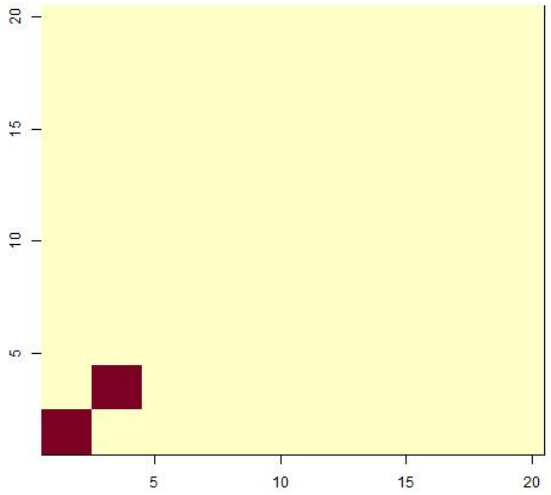

(c) Component 3

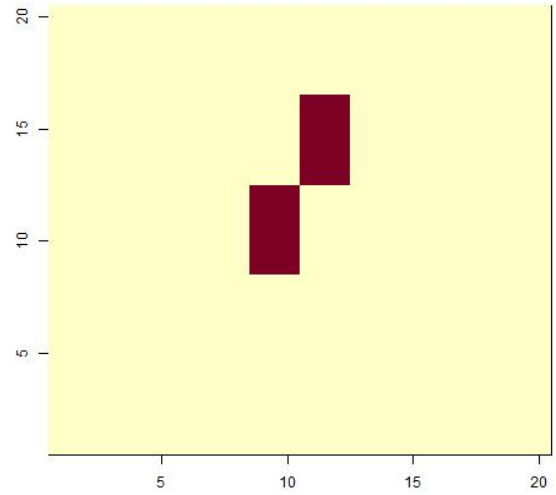

(d) Component 4

Figure 2.5: Spatial components from single simulation without noise.

$$\boldsymbol{A} = \begin{pmatrix} 1 & 0 & 0 & 0 & 0 \\ 0 & 1 & 0 & 0 & 0 \\ 1 & 0 & 1 & 0 & 0 \\ 0 & 1 & 0 & 1 & 0 \\ 0 & 0 & 0 & 0 & 1 \end{pmatrix}$$

These simulated $\boldsymbol{U}$, $\boldsymbol{A}$, $\boldsymbol{S}$ thus represented brain connectivity in separate ways, all of which were of interest to identify in the data. Matrix $\boldsymbol{U}$ represented the temporal activity within each component. This could also be used to model dynamic between-component connectivity, where the temporal patterns in two or more patterns change together. This idea can be seen in simulated components 3 and 4, where both change frequency at the same time midway through the experiment. With resting state or other uncontrolled experiments, it may be difficult to determine if this change is spurious or representing connectivity. Matrix $\boldsymbol{S}$ represented spatial activation in the brain within each component, which also represented within-component spatial connectivity. Thus, the components can be interpreted as "spatial networks", which each network's composition determined by the active regions in the respective row in $\boldsymbol{S}$ [Joel et al., 2011]. Finally, matrix $\boldsymbol{A}$ represented the mixing of each of the 5 components, resulting in the observed data. Thus, this mixing can be interpreted as a form of between-component connectivity with 1 indicating a connection between the respective components and 0 indicating no connection. This can also be interpreted as a thresholded correlation measure between the components (note that $\boldsymbol{A}$ is not symmetric as is the case with correlation matrices as it must be full rank to be estimable).

To analyze the simulated data, two methods were used. The first method was the process described in Section 2.3.3. As a comparison between the proposed method, the second method attempts to extract $\tilde{\boldsymbol{U}}$, $\boldsymbol{A}$, and $\boldsymbol{S}$ using standard SVD and ICA. First, SVD is done on the observed data $\boldsymbol{X}$ for dimension reduction and to extract the temporal and spatial information in the data. This step is again denoted by $\boldsymbol{X} = \boldsymbol{U_0 D_0 V_0^T}$. Then, to de-mix the temporal and spatial components, ICA is run on $\boldsymbol{U_0}$ and $\boldsymbol{D_0 V_0^T}$, resulting in $\boldsymbol{U_0} = \boldsymbol{A_{U_0}} \hat{\tilde{\boldsymbol{U}}}$ and $\boldsymbol{D_0 V_0^T} = \hat{\boldsymbol{A}} \hat{\boldsymbol{S}}$.

Matrices $\hat{\tilde{\boldsymbol{U}}}$, $\hat{\boldsymbol{A}}$, and $\hat{\boldsymbol{S}}$ serve as estimates of $\tilde{\boldsymbol{U}}$, $\boldsymbol{A}$, and $\boldsymbol{S}$ respectively. In both methods, for the steps where ICA is mentioned, colored ICA was applied to the data due to it's incorporation of the temporal and spatial within-component correlation present in the simulated data (see Lee et al. [2011] and Zanini et al. [2016] for details).

First, results from both methods from the simulation referenced in Figures 2.4 and 2.5 for both methods are visualized and discussed. These results are visualized in Figure 2.6, with the matrix compositions from the proposed method in the left column and those from the other method using standard SVD in the right column. Each method's results are in their respective column, with the first four rows of the each column showing the matrix decompositions for the first four components. Each of these four cells contains (from top to bottom) the estimated spatial component, the true temporal component on the left and the estimated temporal component on the right. The fifth row shows the estimated mixing matrix from the designated method.

We see that at this level of additive noise ($\delta = 0.5$), the estimation results for component 3 with the proposed method (denoted *PSVD-cICA*) were noticeably smoother and more reflective of the true signal in the component. This was particularly evident during the period with low frequency activity (see row 3). This improved smoothness was also seen in the low frequency activity in component 4 (though to a less degree, likely because this frequency is higher).

The other major difference was in the estimated mixing matrix, seen in the bottom row of both columns. The PSVD-cICA method correctly identified the mixing matrix, with red values indicating large values (absolute values) for the corresponding entries. Using standard SVD with ICA (denoted *SVD-cICA*) was unable to identify the mixing matrix accurately. This is because the SVD decomposition using PSVD-cICA was done by fixing the temporal components after de-mixing and smoothing them, which allows the mixing matrix to be estimable, unlike the SVD-cICA method. Both methods extracted similar spatial component matrices, likely due to the lack of noise added to these components during the simulation. These differences between the methods were also shown when increasing the additive noise level by setting $\delta = 1$, as shown in simulation results in Figure 2.7.

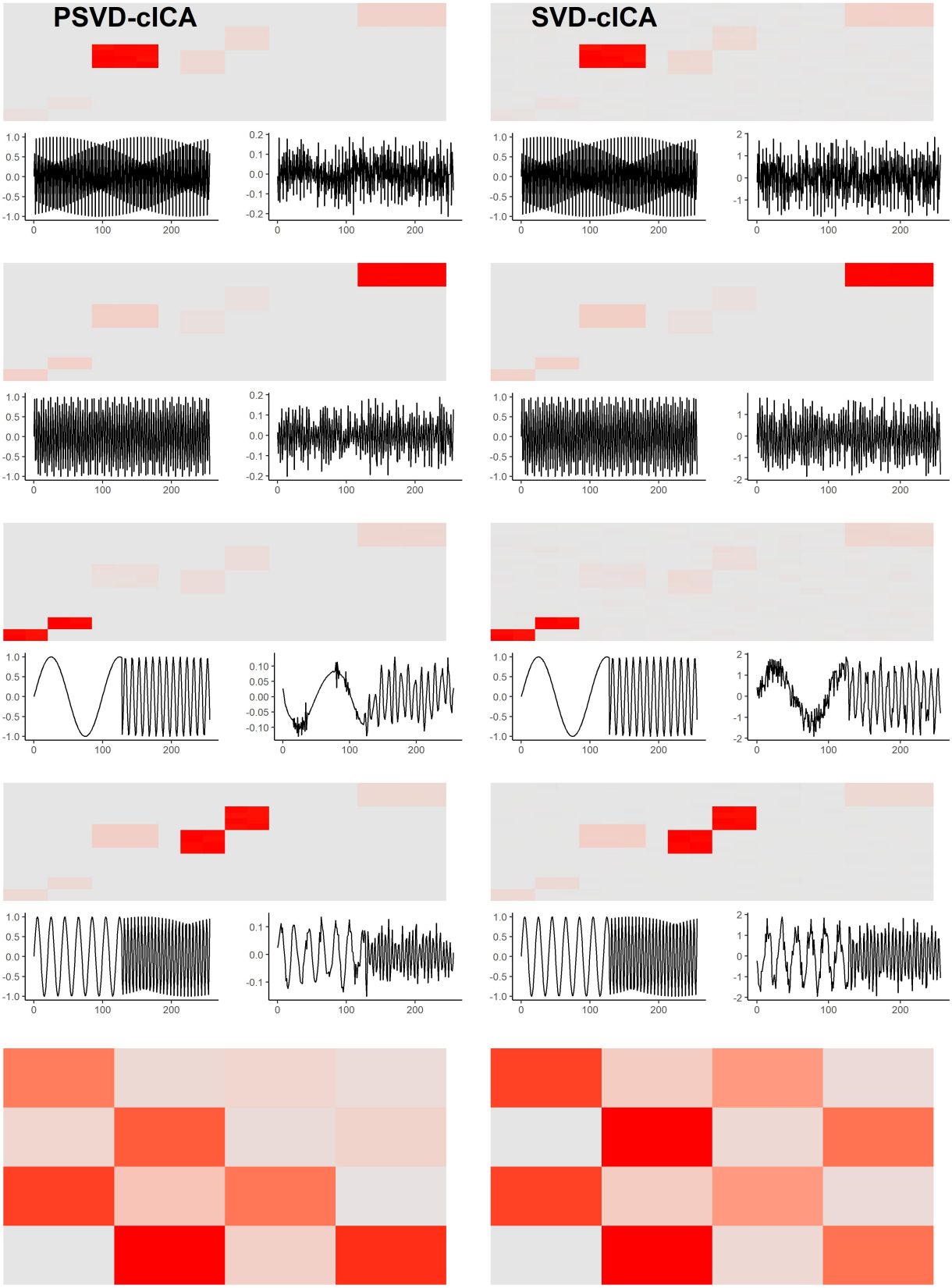

Figure 2.6: Results using proposed and standard SVD-based methods on single simulated dataset with $\delta = 0.5$.

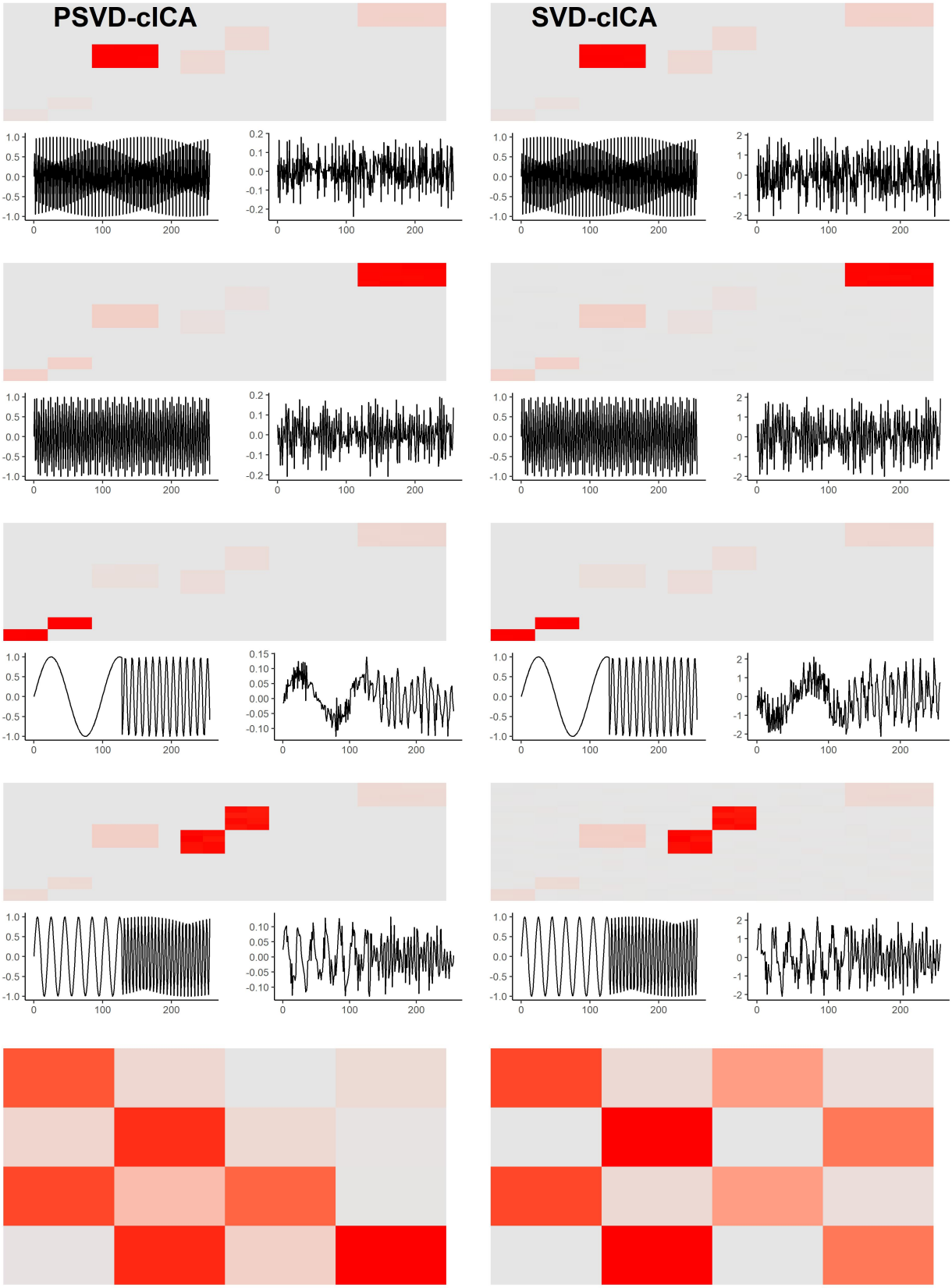

Figure 2.7: Results using proposed and standard SVD-based methods on single simulated dataset with $\delta = 1$.

Second, we considered adding additive spatial noise to the simulations visualized above, to evaluate the proposed method's ability to return sparse spatial components. For each of the first four components (as the fifth is already pure noise), we added noise by generating V independent values from the Uniform[-0.25, 0.25] distribution (as the signal spatial component entries are all 0 or 1). This process was done for both of the $\delta = 0.5$ and $\delta = 1$ simulations above. PSVD-cICA and SVD-cICA were again used to analyze the simulated datasets and extract the temporal and spatial signal components, as well as the mixing matrix.

The results with $\delta = 0.5$ are shown in Figure 2.8. Examining the extracted spatial components, the proposed method PSVD-cICA significantly removed the additive noise, with each individual simulated signal accurately identified. The temporal component smoothing present with the simulation without additive spatial noise was still present, as was the accurately extracted mixing matrix. However, the use of standard SVD in the SVD-cICA method resulted in spatial components which were very noisy and failed to separate two of the independent signals from one another (see rows 1 and 4). Furthermore, the mixing matrix estimate was again inaccurate and the low frequency parts of the returned temporal components were more noisy then those from PSVD-cICA (row 4). These differences in the methods were also seen in Figure 2.9 when $\delta = 1$ and additive spatial noise is added.

Finally, the proposed method was empirically evaluated using the same two scenarios with 1000 simulated datasets for each scenario. That is, the mean spatial component structures, mixing matrices, and noise distributions were the same across a set of 1000 simulations, with the generated temporal and (for the additive spatial noise scenario) spatial noise varying. For each dataset, the same two methods used in the single simulation examples above were used, with the SVD-cICA method again serving as a comparison. Due to the scaling invariance property of ICA, metrics needed to be chosen which are on a standardized scale in order to compare the results across the simulations. The ordering invariance property of ICA also needed to be accounted for. For the temporal components, for each simulation and method used, absolute correlations were computed between each estimated component's and true component's periodogram. The

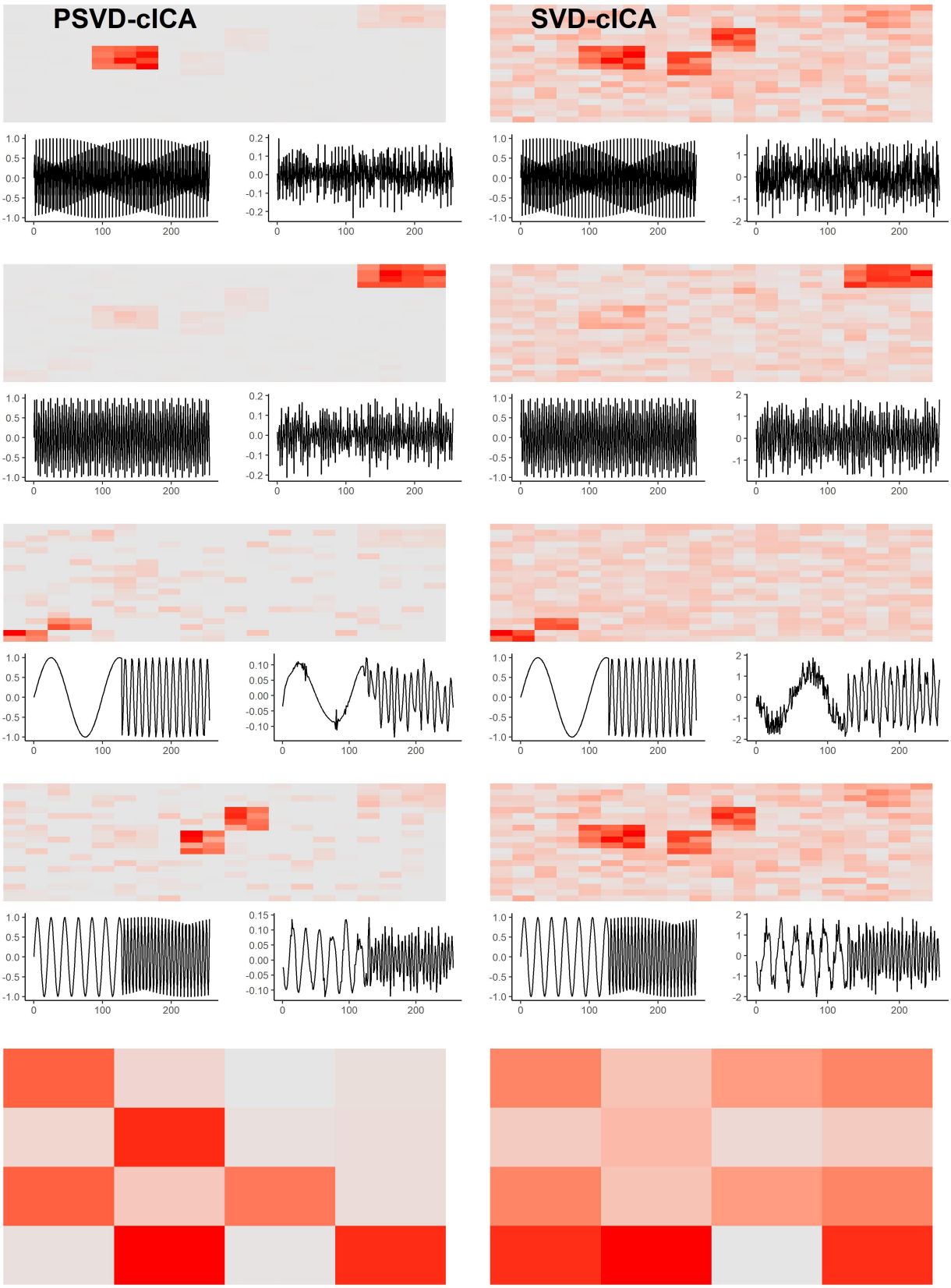

Figure 2.8: Results using proposed and standard SVD-based methods on single simulated dataset with $\delta = 0.5$ and additive spatial noise.

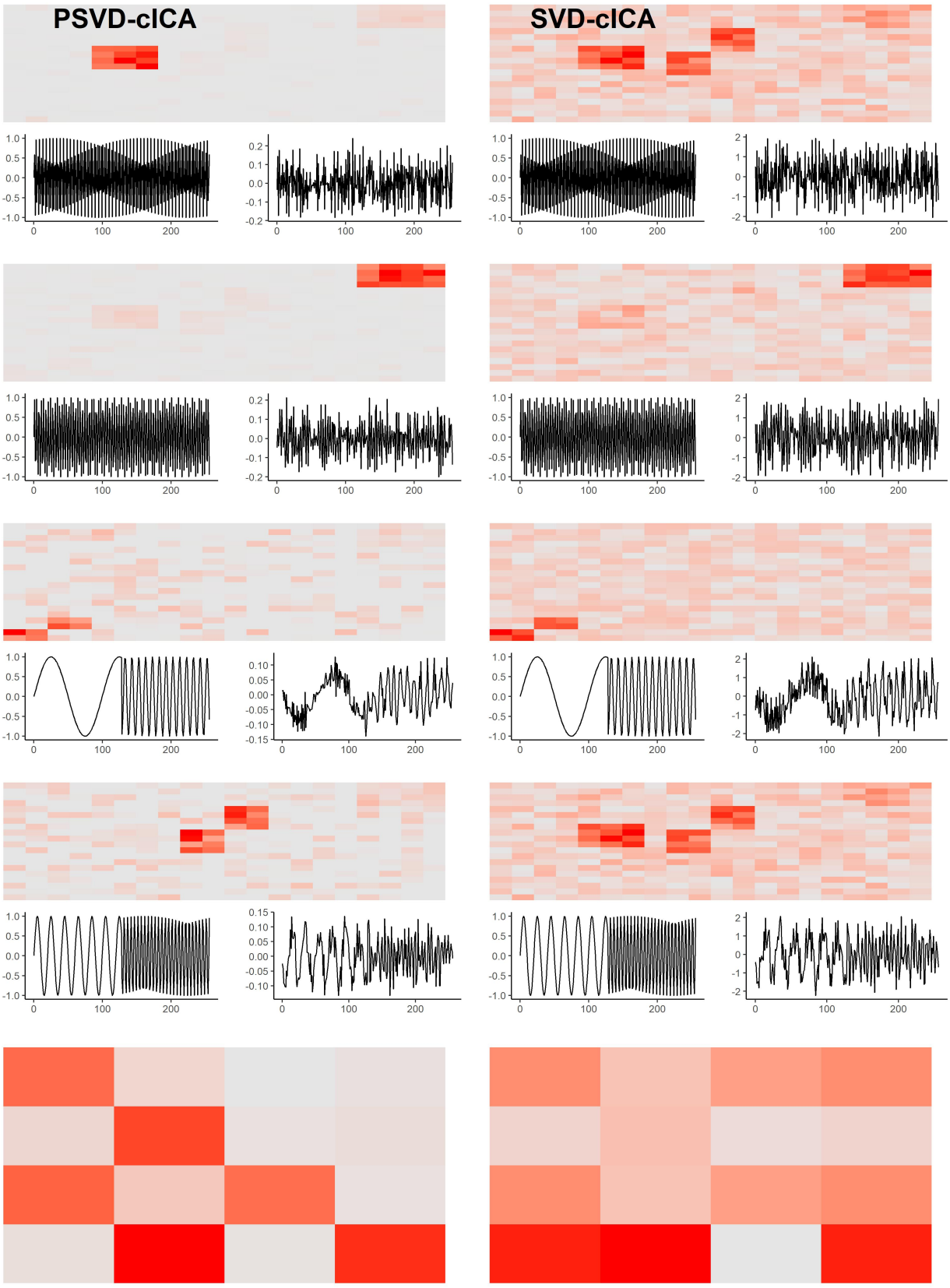

Figure 2.9: Results using proposed and standard SVD-based methods on single simulated dataset with $\delta = 1$ and additive spatial noise.

estimated components were then paired with the true component based on the component with which it had the maximum absolute correlation. This ordering process was also done for the spatial components based on the realizations of the estimated and true components. Finally, for the mixing matrix estimates, the rows and columns were sorted so that the indices matched the re-ordered spatial components. To normalize the mixing matrix entries onto a scale between 0 and 1, the entries were transformed using the following:

$$\tilde{a}_{ij} = \frac{|a_{ij}| - \min(|a_{ij}|)}{\max(|a_{ij}|) - \min(|a_{ij}|)}$$

where a_{ij} indicates the mixing matrix entry at row i and column j. This puts the matrix entries all on the same scale across the simulations, and compares the entries to their minimum value (0) and maximum value (1).

These results are visualized in Figures 2.10-2.15 using boxplots of the absolute correlations for the temporal and spatial components, and of the normalized values for the estimated mixing matrices. Panels where the true and estimated component labels match are colored in red for the temporal and spatial component results. For the estimated mixing matrix results, entries equal to one in the true mixing matrix are colored in red. There were more noticeable differences between the two methods which reflect what was seen in the single simulation results shown above. Most notably, with zero spatial noise, both methods accurately estimated the spatial and temporal components to a similar degree. However, only the proposed PSVD-cICA method was able to consistently identify the non-zero entries of the mixing matrix. With non-zero spatial noise, the proposed method was still able to consistently identify the non-zero entries of the mixing matrix, as well as the spatial and temporal components. However, the comparison SVD-cICA method was not able to estimate the spatial matrix as accurately, with estimated spatial components having notably high correlations between disparate simulated components.

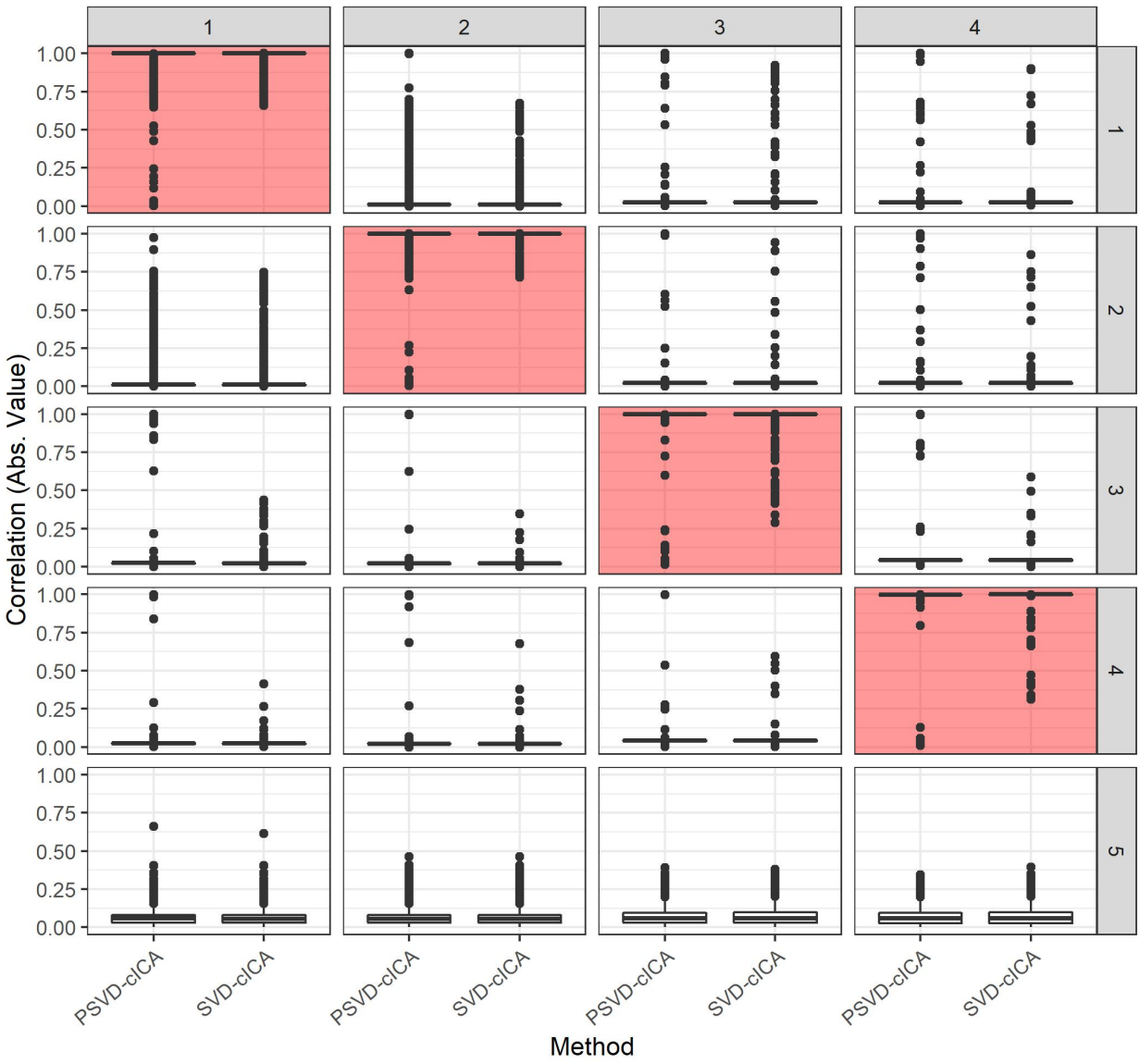

Figure 2.10: Estimation results of the temporal components from the simulated data without additive spatial noise, across 1000 simulations..

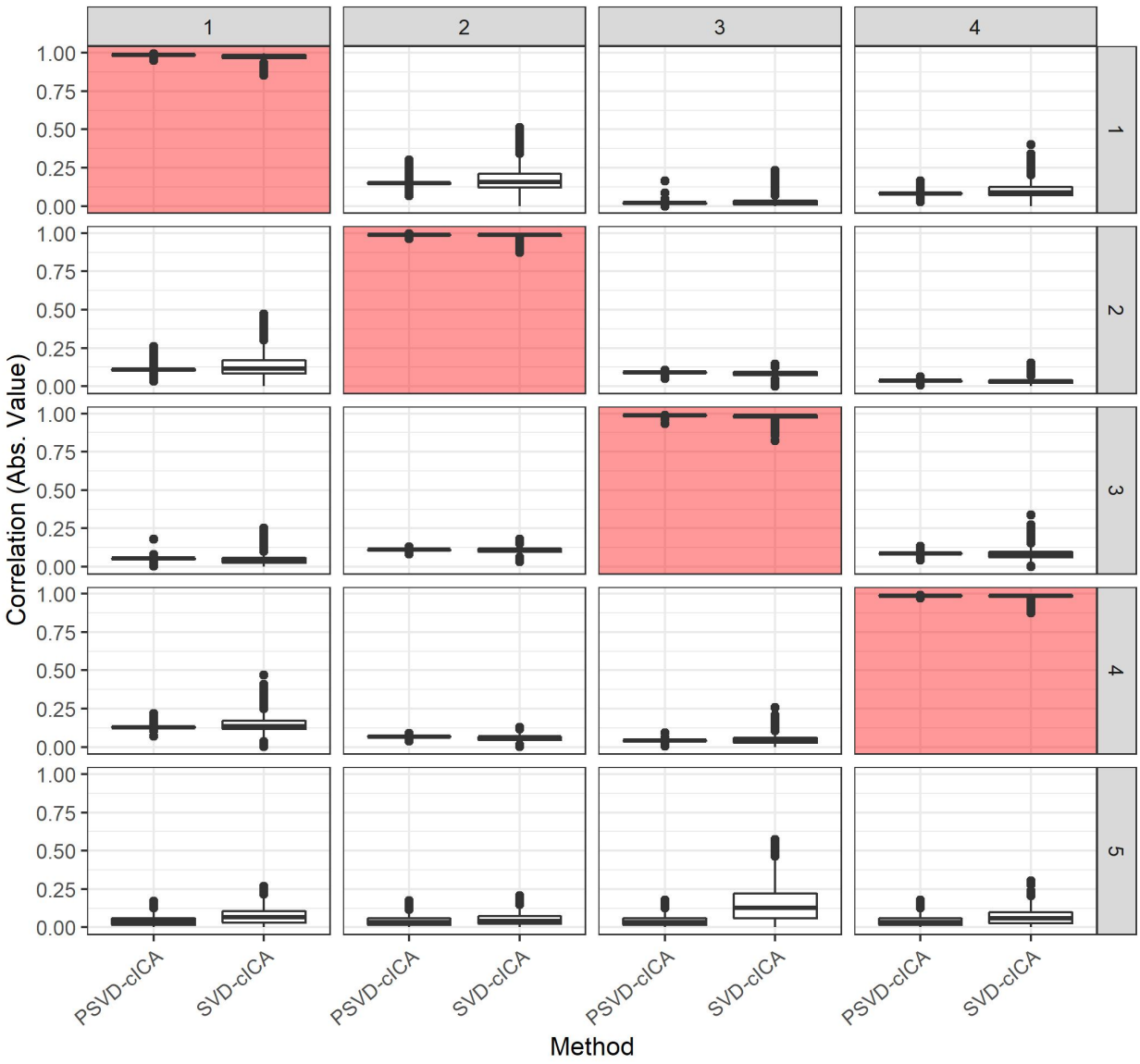

Figure 2.11: Estimation results of the spatial components from the simulated data without additive spatial noise, across 1000 simulations.

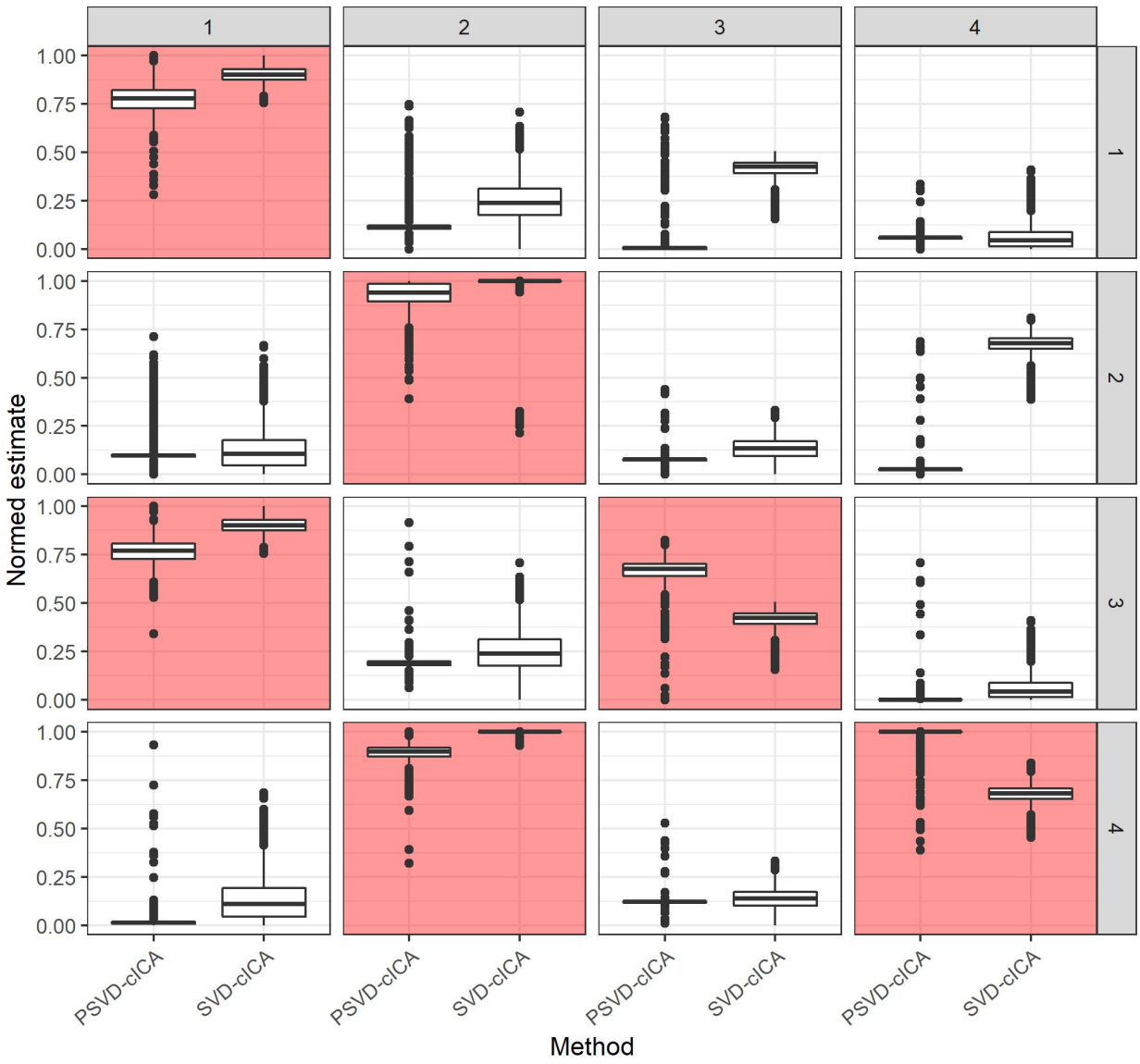

Figure 2.12: Estimation results of the mixing matrices from the simulated data without additive spatial noise, across 1000 simulations.

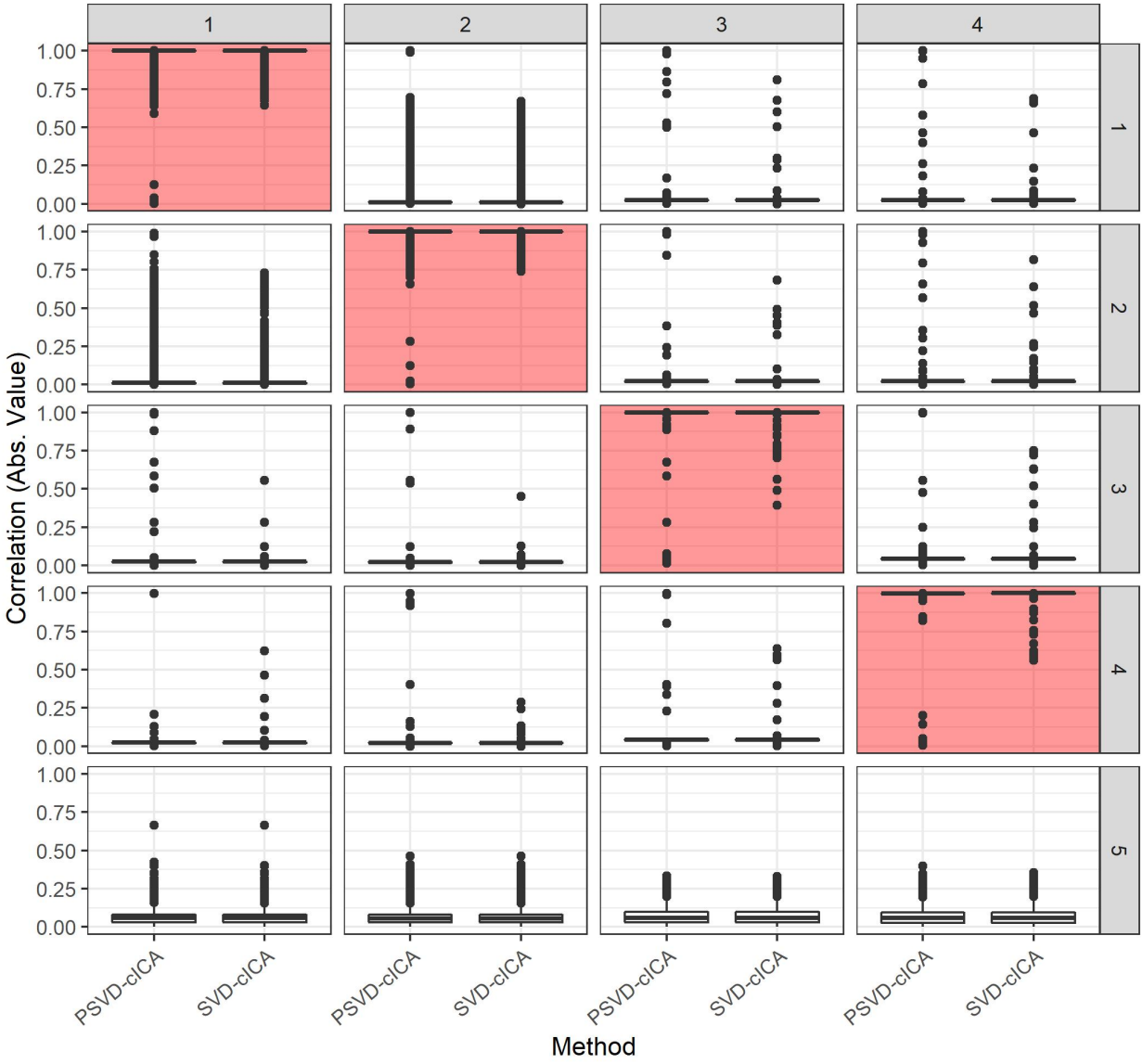

Figure 2.13: Estimation results of the temporal components from the simulated data with additive spatial noise, across 1000 simulations.

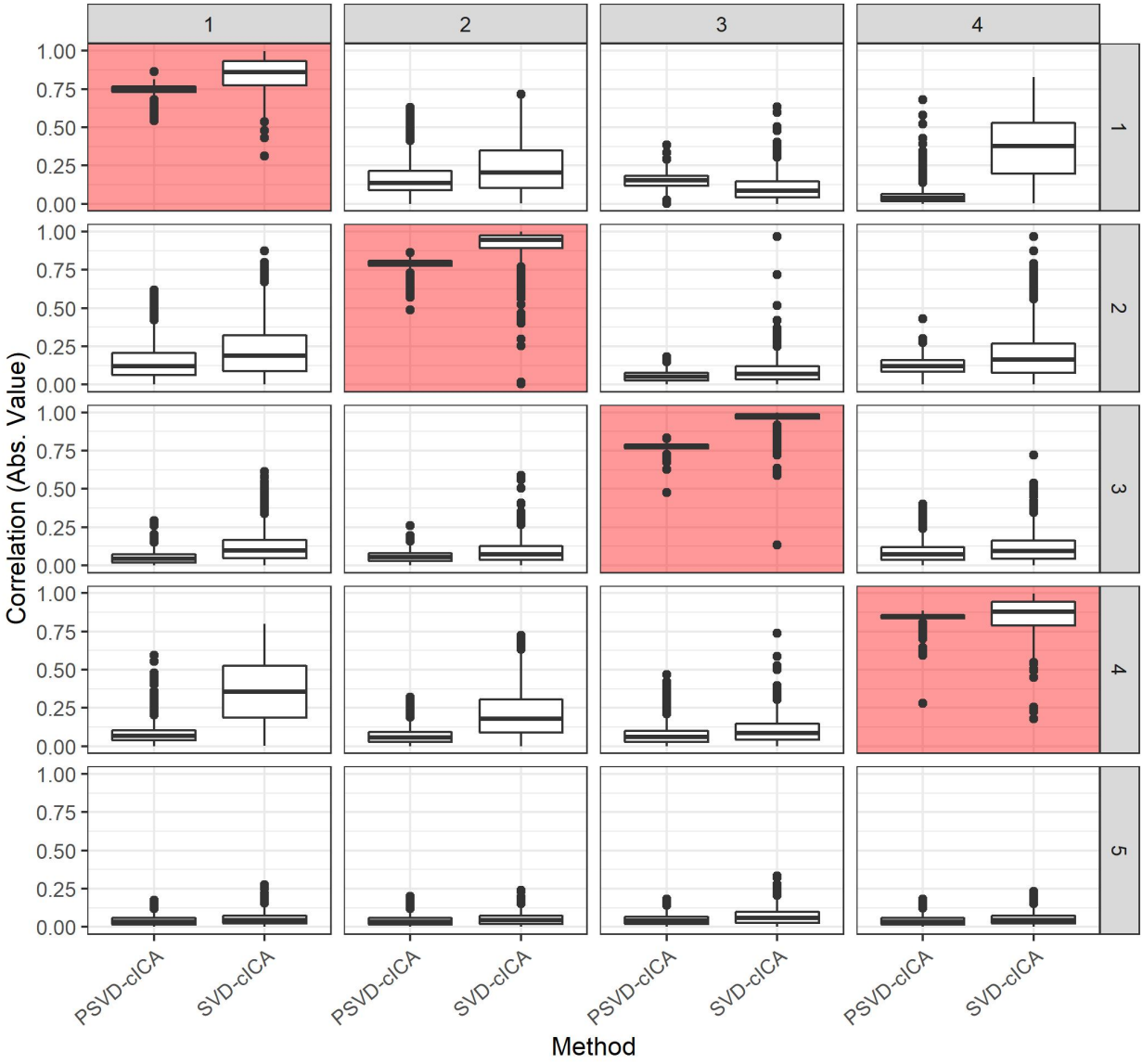

Figure 2.14: Estimation results of the spatial components from the simulated data with additive spatial noise, across 1000 simulations.

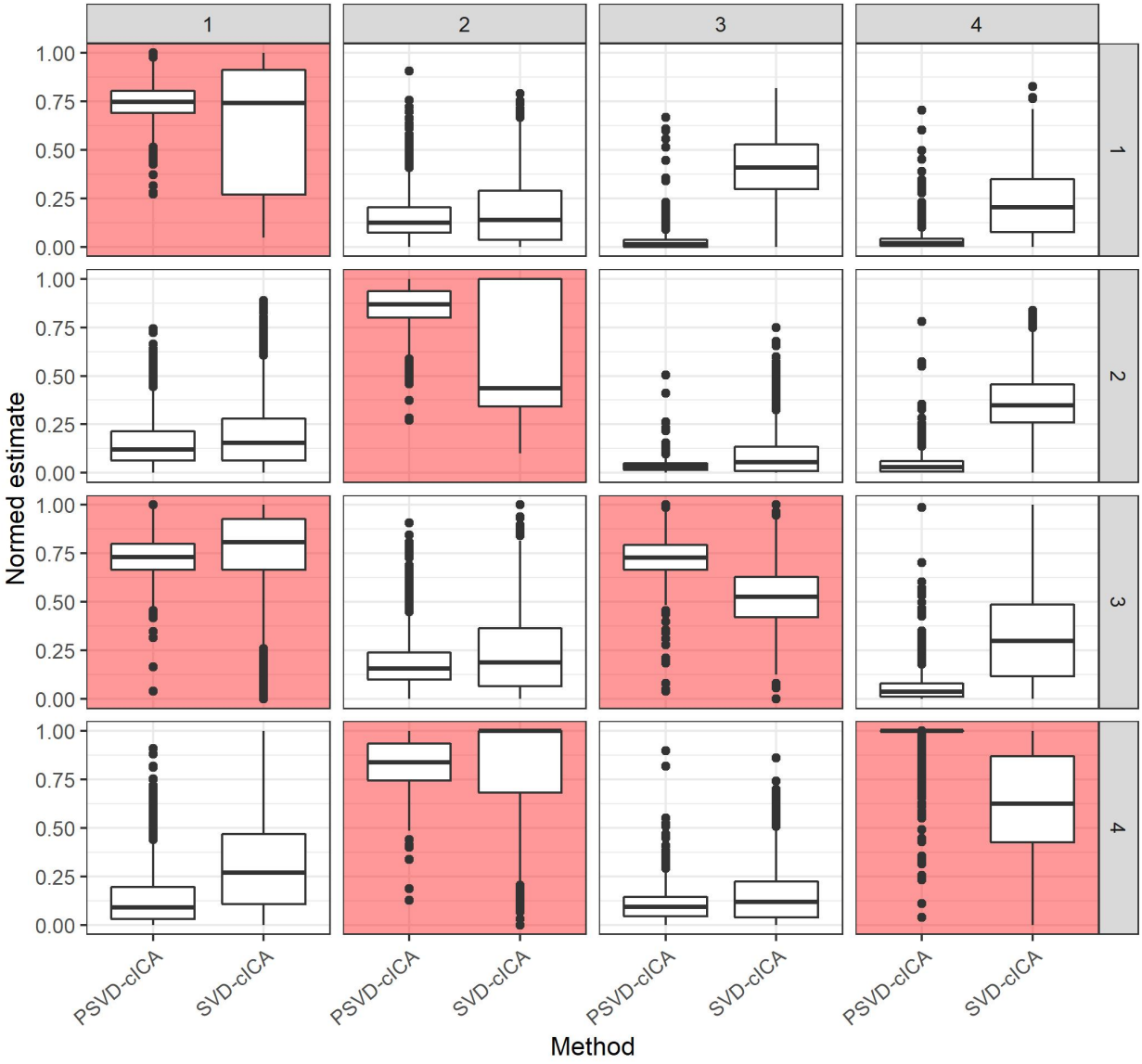

Figure 2.15: Estimation results of the mixing matrices from the simulated data with additive spatial noise, across 1000 simulations.

2.5 Real Data Analysis

The proposed methods were then examined in actual resting state fMRI data from the ABIDE II dataset [Di Martino et al., 2017]. ABIDE is a multi-site study, in which 1114 individuals between 5 and 64 years of age underwent fMRI resting state imaging. The sample consists of 593 controls and 521 individuals diagnosed with Autism Spectrum Disorder (ASD). To illustrate the proposed method, an individual without ASD was selected from the data based on the quality control check report and temporal resolution at the site (subject ID 0050329 from the University of Miami). The minimally pre-processed data for this participant was then selected, with additional pre-processing steps carried out manually in FSL Version 6.0.4 [Jenkinson et al., 2012]. These steps were 1) motion correction using MCFLIRT, 2) BET brain extraction, and 3) spatial smoothing using a Gaussian kernel function with a bandwidth of 5mm as the minimally pre-processed data had already been registered to a standard space [Craddock et al., 2013]. The data was then analyzed using ICA with MELODIC from FSL to select a slice of interest in the Z-dimension to analyze using the proposed methods.

For the Miami site, the fMRI data was scanned using a 3T scanner over a 10 minute session during which the participant was in a resting-state. The data for the chosen ID consisted of 296 time points, which creates a complication with the proposed method as the DWT requires that the time length of the data be of a power of 2 (2^k for positive integer k). Thus, the data must be first zeropadded (zeroes added to the end of the signal to extend it to the desired length). However, zeropadding may impact the spatial components that are returned by SVD and ICA. Thus, the proposed method was slightly altered to accommodate the padding carefully. First, penalized SVD SVD and temporal ICA procedure used to separate the temporal components was done on the zeropadded data, with ICA being run after removing the padding from the returned temporal SVD components. Then, the rank 1 spatial penalized SVD process was altered using the following:

$$v = \arg\min_{v} ||\boldsymbol{X} - vu^T||^2 + \lambda_2 \sum_j |u_j|$$

with temporal component u fixed using the components from the temporal ICA procedure with the zeropadding removed. Spatial ICA was then used on the returned spatial SVD components per usual. Due to the large spatial dimension of the data, the nonparametric cICA method used in the simulations was not feasible. Instead, the cICA implementation described in Lee et al. [2011] was used, which models the independent components in the spectral domain, which was seen to provide similar results in the above simulation studies and is computationally fast. Finally, the temporal ICA components were smoothed per usual after zeropadding each to have a length equal to a power of 2. This avoids the use of zeropadded components and data unless needed to estimate the temporal components using PSVD. This method is compared to the traditional SVD procedure used in the simulation studies. Five components were chosen based on the singular value distribution from running SVD on the observed data, as seen in Figure 2.16.

Figures 2.17 - 2.20 show the decompositions of the data using the proposed and traditional approaches. The spatial components and mixing matrix are combined into a single plot, with each cell showing a different component and the mixing matrix in the last cell. The temporal components are shown in separate rows (5), with each row providing the component realizations on the left and raw periodogram on the right.

The spatial maps were similar in both. Importantly, both methods were able to identify components default mode network (first component in the proposed method, first and second components in the other method) which is commonly present in resting state data. The most noticeable differences were seen when comparing the returned temporal components. The traditional method showed noticeably higher noise in it's low frequency components, evident in both the time course for the component as well as the raw periodogram. This was especially evident for component 4 and 5 from the traditional method, which have a large amount of power across the spectrum. This was less evident in the proposed method, with 4 components dominated by lower

frequency spectra identified and much less visual noise seen in the time courses (see components 1, 2, and 3 from the proposed method).

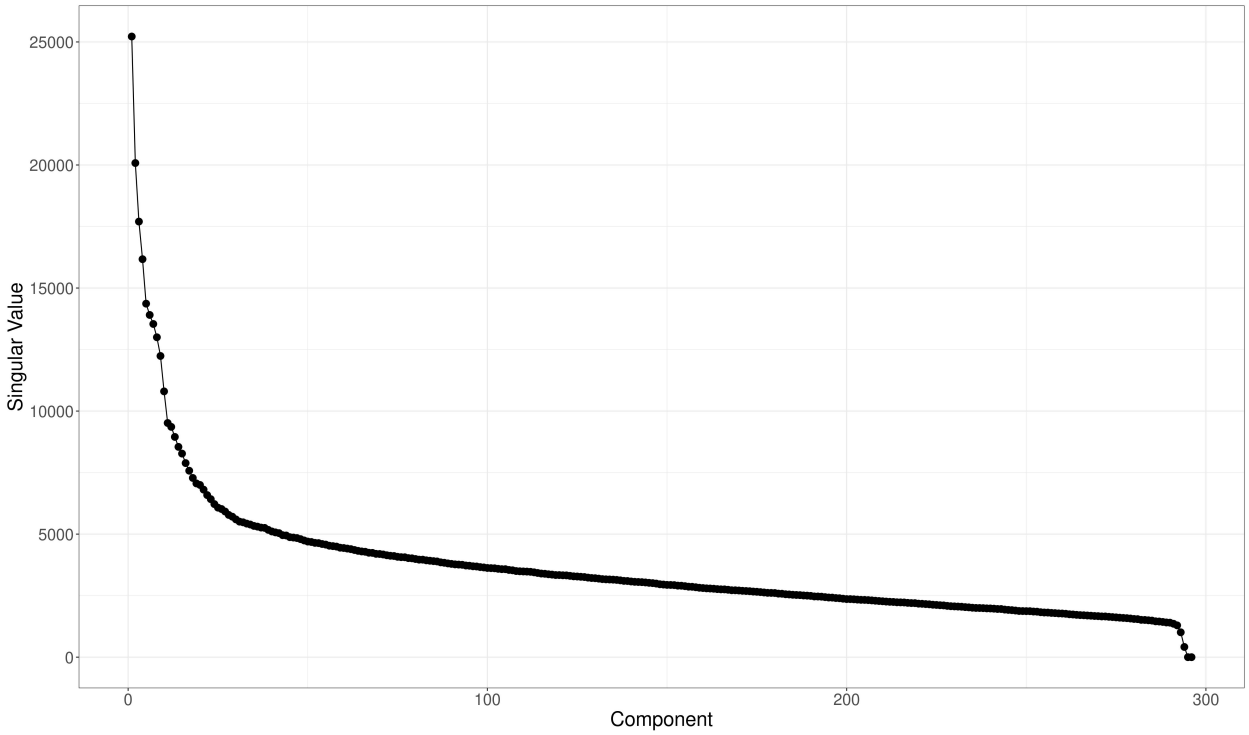

Figure 2.16: Singular values from largest to smallest for ABIDE single-slice data.

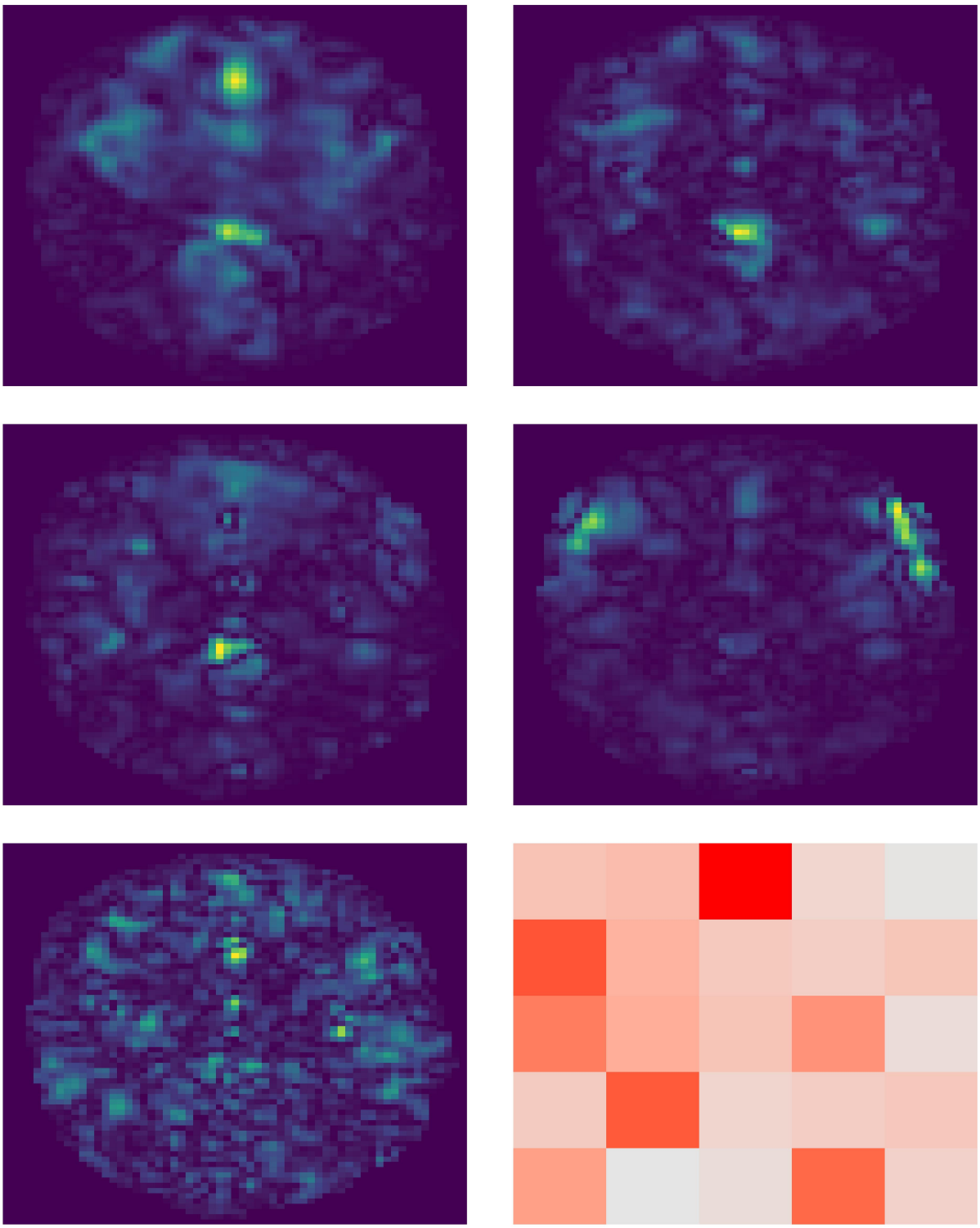

Figure 2.17: Estimated spatial components and mixing matrix from PSVD-cICA method

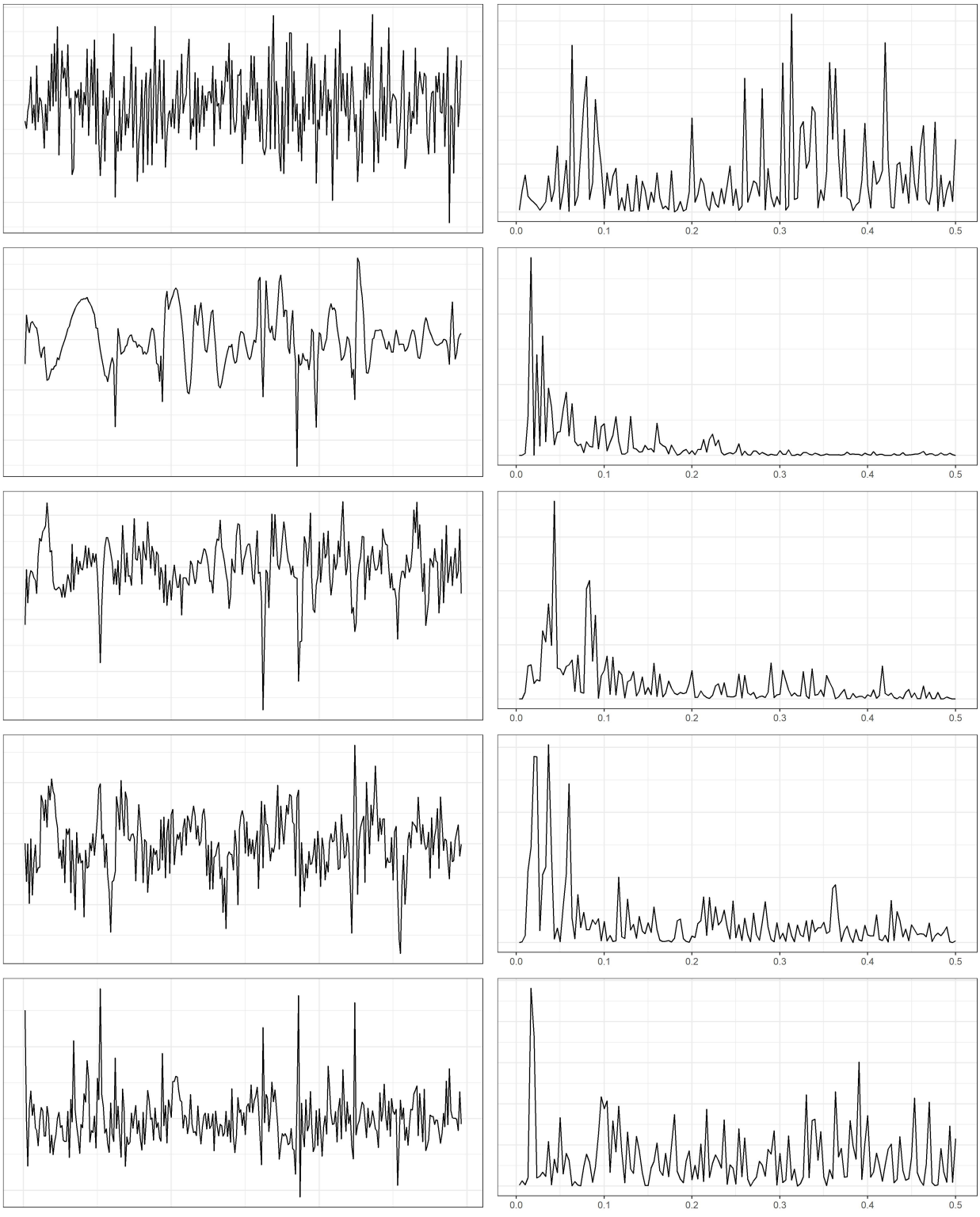

Figure 2.18: Estimated temporal components from PSVD-cICA method

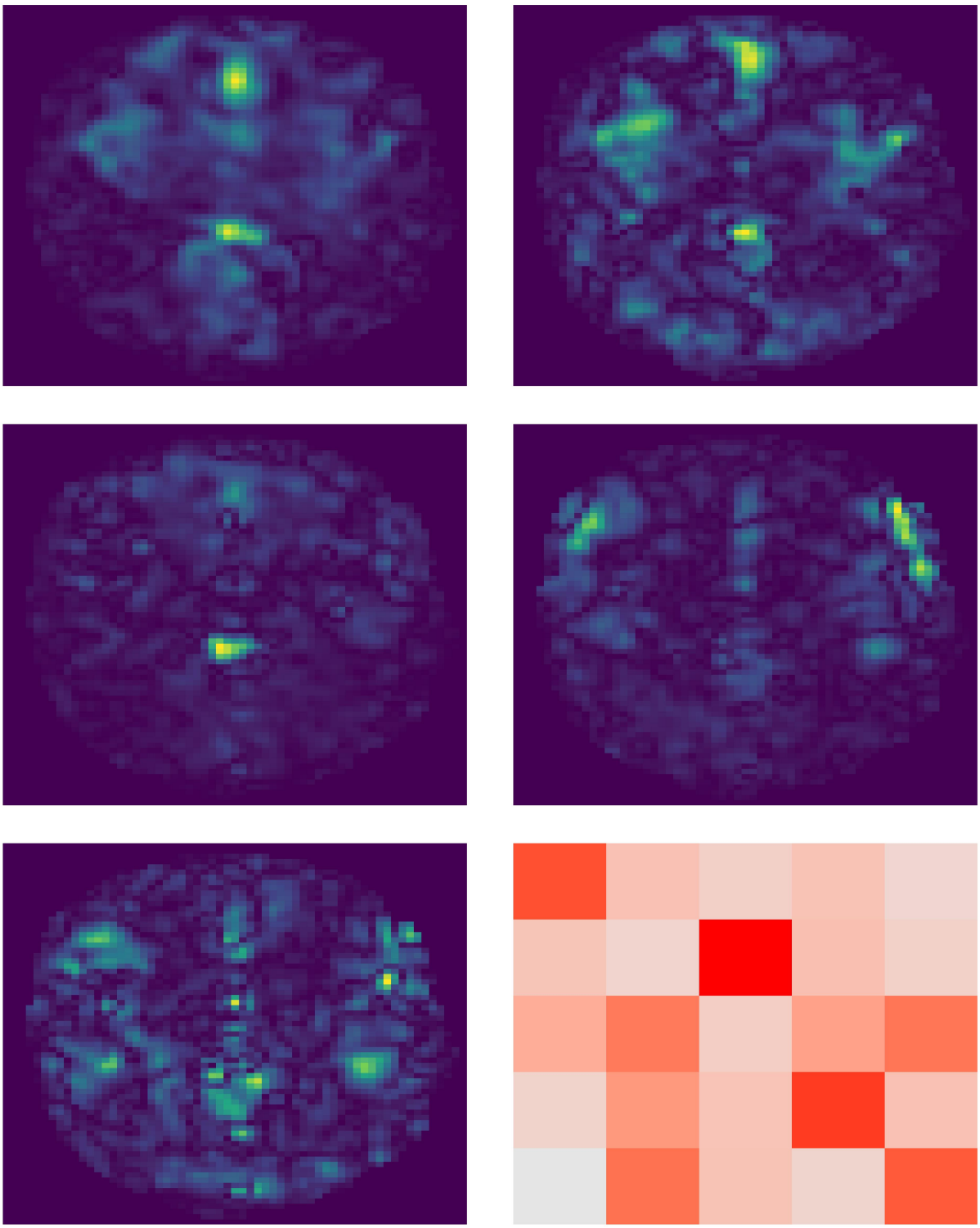

Figure 2.19: Estimated spatial components and mixing matrix from traditional method

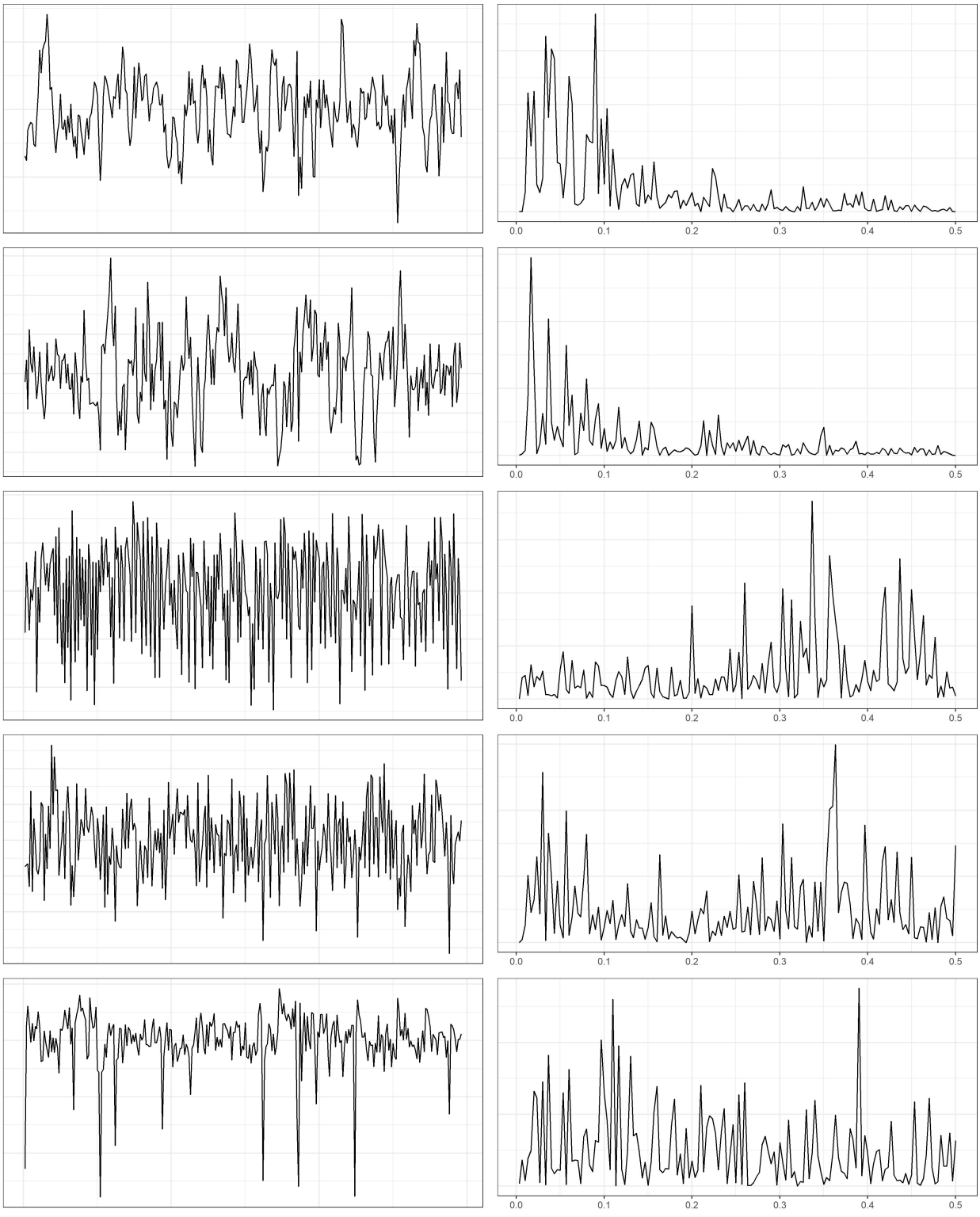

Figure 2.20: Estimated temporal components from traditional method

2.6 Discussion

Brain activity is characterized by dynamic and non-stationary temporal patterns. When combined with the indirect relationship between neuron activity and the BOLD signal, fMRI data often represents a noisy window into the underlying brain activity of interest. This is compounded when a complex stimulus is used in the study, including resting state studies where no stimulus is used. In this work, a flexible model for functional connectivity was presented which makes no assumptions on the temporal or spatial patterns in the underlying activity. This model aims to extract between and within-network connectivity with a higher SNR then traditional methods while also providing smoothed representations of the temporal dynamics of the brain. These properties for the proposed method was evaluated in simulation studies, showing a notable improvement in these areas compared to traditional methods. These properties were also seen when evaluating actual fMRI data from the ABIDE II dataset.

There are some limitations with the proposed methods. The main one is the tuning required for the penalty terms in the regularized SVD method. A grid search is implemented with BIC as the criterion, however this can be computationally costly to carry out. Generally, both penalty terms need to be tuned in some way, with the ranges resulting in significant smoothing being very data-dependent due to the scale invariance of the SVD method. Making this process more efficient and standardized would improve reproducibility of the analysis as well as computational cost. Some ways to accomplish this would be to scale the returned SVD components in some way so that they are comparable across datasets, making the penalty parameter choice less variable from dataset to dataset. Another way to accomplish this would be the implementation of an algorithmic parameter tuning process, such as a Bayesian optimization method which has been used in other contexts (e.g. support vector machine) [Gold et al., 2005]. Furthermore, the restriction of the mixing matrix being full rank may not be optimal for some datasets (for example, means the mixing matrix cannot be symmetric like traditional correlation matrices). Relaxing this restriction may improve computational stability and interpretability. Finally, implementing this model in a

multi-subject setting could be a useful extension, allowing for group differences in the different components and mixing matrix to be identified. This has been implemented in ICA and other matrix decomposition methods (e.g. Group ICA), which could adapted within the framework proposed in this research for single-subject data [Calhoun et al., 2009].

CHAPTER 3: NONPARAMETRIC INDEPENDENT COMPONENT ANALYSIS TO ANALYZE NEURAL SPIKE TRAIN DATA

3.1 Introduction

Neurological activity is characterized by electrical activity within the brain from the transmission of electrical signals between neurons. Neurons generate electrical pulses called *action potentials*, which are voltage spikes that then travel throughout the body using axons. These pulses are generated in response to stimuli (internal and external) in temporal patterns [Strong et al., 1998, Sengupta et al., 2014]. This activity is often measured using non-invasive techniques such as EEG and MRI, which are also indirect measures (EEG due to distance from eletrical signals and MRI through the BOLD response). These action potentials are dichotomous, denoting non-response or response during a brief temporal duration (based on a threshold for the stimulus strength), with the sequence of binary potentials referred to a *spike train* [Gerstner and Kistler, 2002]. For example, sensory and motor neurons follow this "all-or-none" model of response while other specialized neural activity (e.g., from the retina) follows a more continuous electrical response [Kalat, 2015].

Common methods used to measure these action potentials more directly include the use of electrodes directly to specific areas of the brain (*neuronal electrophysiology*) and calcium imaging to infer the electrical activity from changes in calcium concentration in the neuronal cells of interest [Rodriguez-Romaguera et al., 2020]. Typically, these measures suffer from varying degrees of noise which makes identifying the sequence of spikes in the neurons challenging. While many data analysis methods have been developed to estimate the timing of these spikes in a single neuronal cell (*single-channel*), few methods have been developed for this purpose

in multi-cell data (*multi-channel*). In this research, we develop a model to estimate spike trains from multi-cell data as well as the spatial distribution of these spike trains across the cells using ICA. We show it's utility in simulation studies compared to other ICA methods which do not incorporate the spiking structure.

3.2 Literature Review

Techniques have been developed to measure activity from neural spike trains directly and indirectly. Imaging modalities such as EEG and magnetoencephalography (MEG) measure the electrical activity generated by neurons in a non-invasive manner [Cohen, 2014]. However, these suffer from shortcomings such as compromised spatial resolution (EEG and MEG) compared to some other modalities, and volume conduction (EEG) [Cohen, 2014, Mandal et al., 2018]. Furthermore, neural activity far from the scalp can be difficult to measure accurately using these techniques [Cohen, 2014, Mandal et al., 2018]. Since neural spike train activity occurs on a minute spatial scale (individual neuron) within very short time intervals, resolution and noise is an important consideration in the analysis. A commonly-used method of visualizing these spikes over time is by marking the points on the horizontal (time) axis where these spike occur. Sometimes, the cumulative number of spikes as a function of time is plotted on the vertical axis. This is often referred to as a Raster plot; an example is shown in Figure 3.1 [Truong and Lewis, 2016]. The horizontal axis indicates time and vertical axis indicates cumulative number of spikes up to a given time point. Dashes on the horizontal axis indicate a spike has occurred there with the line reflecting the cumulative number of spikes.

Spike trains are commonly modeled as realizations from a point process due to their temporal and integer-valued characteristics. A parametric model is often specified, for example a Poisson process model with a chosen distribution for the spikes, along with Bayesian approaches [Rieke et al., 1999, Brown et al., 2002, Cunningham et al., 2009, Chen, 2013]. ICA has also been used to analyze spike train data due to its high dimensional properties, high degree of noise, and its inherent clustering [Hyvärinen and Oja, 2000, Brown et al., 2001, Savin et al., 2010, Leibig

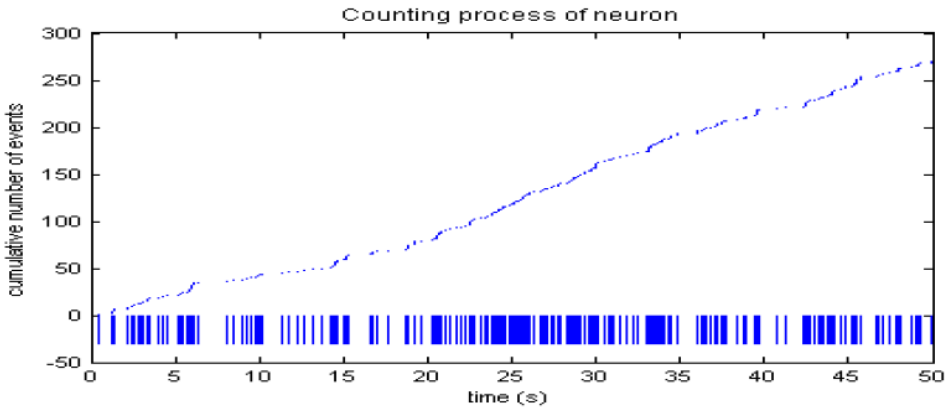

Figure 3.1: Raster plot for single trial of neuron spike train data.

.

et al., 2016]. ICA methods appropriate for spike train data are limited and use heavily parametric models (ex. Poisson process) which may be misspecified when applied to actual data [Reynaud-Bouret et al., 2014, Deepaisarn et al., 2018].

Calcium imaging is a increasingly popular modality for more directly measuring neural spike train activity compared to EEG and similar modalities[Stosiek et al., 2003, Vogelstein et al., 2009, Ahrens et al., 2013]. This technique involves the use of *genetically encode Calcium indicators* (GECIs) that measure the influx of Ca^{2+} ions in electrically activated neurons. The Ca^{2+} influx results in the emission of light (referred to as *fluorescence*) which can be detected through microscopy [Stosiek et al., 2003]. Thus, individual and population-level neural activity can be observed and recorded. The number of neurons which can be recorded simultaneously is continually increasing, allowing whole brain activity to be recorded in certain animal models [Ahrens et al., 2013]. Thus, the spatial resolution is very high, allowing the recording of individual neuronal cells, including those deep within the brain. Though temporal resolution is lower then others (EEG for example) due to the temporal lag in the calcium release after an electrical spike, it is continually improving as the methodology develops [Vogelstein et al., 2009]. Due to its invasive nature, it has currently been exclusively used in animal models, resulting in improved understanding of functional changes on specific neuron populations and networks [Grewe et al., 2010, Mittmann et al., 2011, Ahrens et al., 2013, Rodriguez-Romaguera et al., 2020].

The main benefit of using GECIs compared to invasive electrode-based methods in electrophysiology is that since GECIs are designed to bind to neurons based on their genetic makeup, they can be used to measure activity in a set of cells which contain genetic traits of interest. This allows for the targeting of specific cells of interest which be spatially separate. In contrast, eletrode-based measures can only record activity in neurons near the electrode placement. This makes it very difficult to target specific types of neuronal cells (as all cells near the electrode will be assessed), results in the measured acitvity in the cells being related to its distance from the electrode, and makes it impossible to record the same cell throughout multiple trials [Rodriguez-Romaguera et al., 2020].

Various methods have been developed and utilized in the literature to analyze calcium imaging data. The single-neuron resolution creates additional complications which need to addressed for neuron-specific activity to be accurately analyzed. Major complications include identifying the spatial locations of each neuron in the image, demixing spatially overlapping neurons (as data are analyzed using 2D images of a 3D space), and deconvolving and denoising the underlying neural activity from the observed fluorescence activity [Pnevmatikakis et al., 2016]. This last point is due to the temporal lag between neural activity and the calcium fluctuation (which has a slow decay), resulting in measurement error similar to the BOLD response in fMRI data.

Despite these concerns, some studies have analyzed the observed fluorescence response directly. Correlation analyses of time series between specified spatial ROIs (equal to the mean fluorescence response across the locations for each time point) have been conducted to assess connectivity. Analyzing these ROIs created from means of specified spatial locations for each time point, along with transformation of the observed fluorescence data into more stable measurements (for example, fluorescence change rate or moving averages) have been used to reduce noise [Wang et al., 2003, Tibau et al., 2013, Ahrens et al., 2013, Resendez et al., 2020]. Standard time series analyses have also been used with the fluorescence data, such as estimating the frequency components in the spatial ROI time series [Ahrens et al., 2013, Tibau et al., 2013].

Matrix factorization methods have also been used to address these complications with calcium imaging data, specifically identifying the spatial positions of the individual cells (composed of neurons) in the image. One example is nonnegative matrix factorization (NMF) [Liu et al., 2011, Maruyama et al., 2014]. Let $\boldsymbol{Y}$ denote the observed N by T data matrix of fluorescence responses where N denotes the number of spatial locations and T denotes the number of time points. Let K denote the number of cells in the image. Assume that $\boldsymbol{Y}$ can be represented by

$$\boldsymbol{Y} = \boldsymbol{S}\boldsymbol{A} + \boldsymbol{s_b}\boldsymbol{a_b} + \boldsymbol{\epsilon}$$

where $\boldsymbol{S}$ is a N by K spatial component matrix, $\boldsymbol{A}$ is a K by T temporal component matrix and $\boldsymbol{\epsilon}$ is a N by T matrix of error terms. Component vectors $\boldsymbol{s_b}$ (N by 1) and $\boldsymbol{a_b}$ (1 by T) represent the spatial and temporal distributions of the background fluorescence intensity respectively. matrices $\boldsymbol{S}$ and $\boldsymbol{A}$ represent the spatial and temporal fluorescence intensity fluctuations in the cells (column-wise for $\boldsymbol{S}$ and row-wise for $\boldsymbol{A}$) respectively. Background fluorescence refers to activity that is observed in the image but not related to cell activity of interest. Fluorescence is a measure of light intensity and is constrained to take positive values, so a non-negative matrix constraint is imposed on $\boldsymbol{S}$, $\boldsymbol{A}$, $\boldsymbol{s_b}$, and $\boldsymbol{a_b}$ (all elements of the matrices must be non-negative). The entries in matrix ϵ are assumed to be independent and Normally distributed with mean 0 and equal variance across space and time. Estimation is done by maximizing the corresponding log-likelihood, with $\boldsymbol{a_b}$ fixed and assumed known [Maruyama et al., 2014]. This method was designed to identify spatially separate neuronal cells, which is an important step in the analysis pipeline (as it is not explicit in the image which areas represent distinct cells).

Another common factorization method combines PCA and ICA [Mukamel et al., 2009]. First, each location's data is normalized spatially by dividing the location's mean across time for each timepoint. It is then normalized temporally by subtracting the mean across the locations for each time point from each location's data. This done to transform the spatial and temporal means to 0, and remove thus theoretically remove the background fluorescence. As a dimension reduc-

tion technique, PCA is done on this transformed data (denoted $\tilde{\boldsymbol{Y}}$) where $\boldsymbol{Y} \approx \tilde{\boldsymbol{Y}} = \boldsymbol{U}\boldsymbol{D}\boldsymbol{V}^T$ using a chosen number of principal components (PCs), denoted N_{PC}. Matrix $\boldsymbol{D}$ is a N_{PC} by N_{PC} diagonal matrix containing the eigenvalues of $\boldsymbol{Y}^T\boldsymbol{Y}$ (sample covariance matrix), reflecting the magnitude of each PC. N by N_{PC} matrix $\boldsymbol{U}$ consists of the temporal PC realizations and N_{PC} by V matrix $\boldsymbol{V}$ consists of the spatial PC realizations. Then ICA is used to separate the underlying cells from the dimension-reduced fluorescence data, modeling $\tilde{\boldsymbol{Y}} = \boldsymbol{A}\boldsymbol{S}$. N by K matrix $\boldsymbol{A}$ denotes the K spatial component realizations and K by T matrix $\boldsymbol{S}$ denotes the K temporal component realizations, where K is chosen a priori. ICA assumes the data is composed of a chosen number (K) of latent variables, in this case reflecting the cellular activity. Maruyama et al. [2014] compared the methods, finding both approaches performing similarly in some simulated scenarios and NMF performing better in others (depending on model parameters such as N_{PC}).

More advanced decoupling and denoising methods have been developed at the single-neuron scale (analyzing one-dimensional time series data from each neuronal cell, one at a time), using supervised learning [Theis et al., 2015] and Markov chain Monte Carlo/Bayesian methods [Pnevmatikakis et al., 2013, Deneux et al., 2016]. Pnevmatikakis et al. [2016] address the deconvolution of the neural activity from the recorded fluorescence time series using a parametric modeling approach. The relationship of the fluorescence response evoked by the spikes from a neuron population is modeled as an autoregressive (AR) process of order $p > 0$ (p small). It is further assumed that the spikes from the neurons follow a stationary Poisson process across the time series. The underlying spiking signal is then estimated using a non-negative sparse constrained deconvolution method. This method identifies the neural activity signal which best fits the data according to the following constraints: 1) fluorescence response and underlying neural spiking follow above parametric model, 2) signal is non-negative, 3) signal has level of noise no greater then a specific level. That is, the underlying neural activity is predicted based on the observed fluorescence data and the parametric model specifications. This AR relationship has also been used in combination with a penalty term to filter out which observed spikes in the fluo-

rescence represent electrical spikes and which are noise, similar to a penalized regression model [Jewell et al., 2020].

Pnevmatikakis et al. [2016] used an adjusted version of NMF called contrained nonnegative matrix factorization (CNMF), as a spatialtemporal demixing process to identify activity at the neural level. For $t = 1, \ldots, T$ let $F(t)$ be a N by 1 vector such that

$$F(t) = \sum_{i=1}^{K} a_i c_i(t) + B(t)$$

where a_i is a N by 1 vector containing the spatial component for cell i across time, $c_i(t)$ denotes the calcium activity of cell i at time t and $B(t)$ is a N by 1 vector for each time point t denoting the time-varying baseline calcium activity at each location. Vector $F(t)$ denotes the calcium activity at each location at time t with the K cells as latent variables. This formulation is very similar to the mixing model in NMF and ICA. Finally, model the observed fluorescence data at time t by

$$Y(t) = F(t) + \epsilon(t)$$

for $t = 1, \ldots, T$ where matrix $\boldsymbol{Y} = [Y(1), \ldots, Y(T)]$, matrix $\boldsymbol{F} = [F(1), \ldots, F(T)]$, and $\epsilon(t) \sim N(0, \boldsymbol{\Sigma})$ where $\boldsymbol{\Sigma}$ is diagonal.

Denoting the K by T matrix of cell spiking activity by $\boldsymbol{S}$, where $\boldsymbol{S}$, $\boldsymbol{F}$ and $\boldsymbol{Y}$ are identified by estimating the model parameters (including those from the previously detailed deconvolution step). Sparsity is implemented into the fitting algorithm for the various parameter matrices by specifying constraints based on the L_1 norm along with a chosen noise threshold. Choosing the number of components K is generally difficult to do a priori and an ad hoc procedure is used based on the maximum level of temporal and spatial activity in the components after fitting. The procedure is then redone with the "weaker" components removed by reducing K. The authors compare their method to the PCA-ICA procedure, showing an improved detection of overlapping neurons in simulation studies. However, the parametric models for the relationship between the fluorescence response and neural calcium activity, as well as the neuron spike activity, may

be misspecified, impacting the accuracy of the purposed method. Furthermore, none of these methods for deconvolution are designed for multi-channel analysis. That is, they do not model the spike trains of multiple neuronal cells jointly. This can be limiting, as it prevents the direct modeling of the interactions between different cells, as well as the additional power that may be gained by leveraging multiple neurons' data.

Traditional ICA assumes that the latent independent components are continuous [Hyvärinen and Oja, 2000] and does not take within-component correlation (across time or space, for example) into account during estimation. Both of these assumptions are problematic for fluorescence imaging analysis, especially when the temporal autocorrelation within a neuron population is of interest. Lee et al. [2011] developed an ICA model which accounts for and conducts inference on the autocorrelation structure within the latent components, however it assumes an AR model for these. Given that the latent components of interest are neuron spikes, these realizations are nonnegative integers, and thus an AR model may not be appropriate. Deepaisarn et al. [2018] developed an extension to ICA referred to as linear Poisson ICA. This method models the latent components as having Poisson-distributed errors (instead of the normally distributed errors traditionally assumed) with the same $\boldsymbol{AS}$ formulation and interpretation as in traditional ICA, with estimation done using maximum likelihood through the EM algorthim. However, the Poisson distributional assumption may result in the model being misspecified (especially given the equal mean and variance assumption of Poisson noise). Further, it assumed that the noises components are independent within each component. Thus autocorrelation within the latent components is not being considered, causing the model to potentially be misspecified.

3.3 Proposed Methods

3.3.1 Point Processes

The proposed ICA model for neural spike train data incorporates some standard concepts and notation from survival analysis and point processes, which we describe here, adapted from Truong and Lewis [2016]. Neural spike trains can be formulated statistically as examples of a

point process. Let T denote the length of time the spike train is observed and define the ith spike time as τ_i for $i = 1, \ldots, n$ where $0 < \tau_1, \ldots, \tau_n \leq T$. The τ_i are assumed to be random and thus unknown a priori. For $t \in (0, T]$, define the point process

$$S(t) = \sum_{i=1}^{n} \delta(t - \tau_i)$$

where $\delta(x) = 1$ if $x = 0$ and 0 otherwise. Process $S(t)$ reflects a firing neuron where τ_i represent the firing times and firing is considered binary (recall "all-or-none" model of spike trains). To represent the total amount of firings up to time t, define $N(t) = \sum_{i=1}^{n} I(\tau_i \leq t)$ for $0 < t \leq T$ where $I(.)$ denotes the indicator function. This is an example of a *counting process*. This process has the following properties: i) $N(t) \geq 0$ for all t, ii) $N(t)$ is an integer-valued function, iii) if $s < t$, then $N(s) \leq N(t)$.

A counting process has *independent increments* if $N(t_0) - N(s_0) \perp N(t_1) - N(s_1)$ where $[s_0, t_0]$ and $[s_1, t_1]$ are disjoint intervals. The process has *stationary increments* if $N(t) - N(s) = f(t - s)$ for some function $f(.)$ and $0 \leq s \leq t$. That is, if the number of neuron spikes during a time interval is only dependent on the length of the interval. For spike trains, these assumptions may not hold. For example, the number of firings in the past may impact the distribution of later spikes. This violates the independent increments assumption. Some methods for spike train analysis specify a homogeneous Poisson process model for the spike train distribution [Pnevmatikakis et al., 2016]. This model assumes independent and stationary increments, along with assuming $\Pr(N(t) = k) = \exp(-\lambda t)(\lambda t)^k / k!$ for $t \geq 0$ where $\lambda > 0$ is a rate parameter. These two increment assumptions plus the specific distributional form are subject to misspecfification.

A further assumption with a Poisson process is that the number of spikes at time t is independent of the number of spikes at time s for $0 < s < t \leq T$. Then can be seen by computing the

corresponding conditional density

$$\Pr(N(t) = x | N(s) = y) =$$
$$\Pr(N(t) - N(s) = x - y | N(s) - N(0) = y) =$$
$$\Pr(N(t) - N(s) = x - y) \text{ due to independent increments}$$

as $(s, t]$ and $(0, s]$ are disjoint intervals. This is called the *memoryless property* and is a further assumption of a Poisson process model which may be misspecified for neural spike train processes. The distribution of spikes at a time point given the past activity can be defined using the *conditional intensity function*, denoted $\lambda(t|H_t)$, where H_t is the "history" of the spike train up to time t. The "history" is composed of all spiking activity before time t, i.e. function $N(s)$ such that $0 < s \leq t$, including how this activity is correlated along $(0, t]$. This function is defined by

$$\lambda(t|H_t) = \lim_{\Delta \to 0} \frac{\Pr[N(t + \Delta) - N(t) = 1 | H_t]}{\Delta} \tag{3.1}$$

which denotes the probability of a spike on $(t, t + \Delta)$ where Δ is a small increment decreasing towards zero, given the past activity in the spike train. That is, the conditional intensity function denotes the probability of a spike instantaneously after time t given all of the activity at and before time t. In survival analysis where only a single spike can occur during the entire time course of the process, $\lambda(t|H_t)$ is referred to as the *conditional hazard function*, where H_t contains no spikes (no events up to time t).

Recall the time until spike i is given by τ_i for $i = 1, \ldots, N$. Define the *interspike interval* (ISI) by $u_i = \tau_i - \tau_{i-1}$ for $i = 1, \ldots, n$ where $\tau_0 \equiv 0$. This refers to the time between each spike which is random. We can define the conditional ISI density by

$$p(t|H_t) = \lim_{\Delta \to 0} \frac{Pr(t < U < t + \Delta | H_t)}{\Delta}$$

where U denotes the ISI as a random variable and H_t denotes the "history" as defined before, up to the last spike. Per the relationship between the hazard, density, and survival functions in survival analysis, we can express the conditional hazard function as a function of the conditional ISI density with

$$\lambda(t|H_t) = \frac{p(t|H_t)}{1 - \int_0^t p(t|H_t)dt}.$$

Then the conditional ISI density can be expressed as

$$p(t|H_t) = \lambda(t|H_t) \exp\Big\{ - \int_0^t p(s|H_s)ds \Big\}. \tag{3.2}$$

The joint distribution of the ISIs from a series of spikes can then be formed by

$$\begin{aligned} f(u_1, \ldots, u_n|N(T) = n) &= p(u_1)p(u_2|u_1) \ldots p(u_n|u_1, \ldots, u_{n-1}) \\ &= \prod_{k=1}^{n} \lambda(u_k|H_{u_k}) \exp\Big\{ - \int_0^{u_k} \lambda(s|H_s)ds \Big\} \\ &= \prod_{k=1}^{n} \exp\{\alpha(u_k|H_{u_k})\} \exp\Big\{ - \int_0^{u_k} \exp\{\alpha(s|H_s)\}ds \Big\}. \end{aligned} \tag{3.3}$$

where $\alpha(u_k|H_{u_k}) = \log[\lambda(u_k|H_{u_k})]$. Thus, we can estimate the joint density of a point process through the ISIs and by estimating the log conditional intensity function instead.

3.3.2 Hazard Estimation with Flexible Tails (HEFT)

We now turn to the nonparametric estimation of the log conditional intensity function, hereafter referred to as the log-hazard function, using the HEFT method [Kooperberg et al., 1995]. The estimation of the log-hazard removes any positive constraints from the procedure. First, we define a cubic spline, which will be used to model the log-hazard. Function $S(t)$ defined on $[a, b]$ is a cubic spline if 1) S, S', and S'' are all continuous functions on $[a, b]$ and 2) for *knots* t_i such that $a = t_0 < t_1, \ldots, t_p = b$, S is a polynomial of degree at most 3 on each subinterval $[t_j, t_{j+t}]$ for $j = 0, \ldots, p - 1$. The degree of smoothness of the spline is determined the continuity of

its derivatives; in this case the first and second derivatives (higher order continuous derivatives implies greater smoothness). The spline $S(t)$ can be constructed using a set of basis functions, with the ***B spline*** method being a common method of defining the set. A B spline of order $k \geq 0$ is defined by

$$B_i^k(t) = \frac{t - t_i}{t_{i+k} - t_i} B_i^{k-1}(t) + \frac{t_{i+k+1} - t}{t_{i+k+1} - t_{i+1}} B_{i+1}^{k-1}(t) \text{ for } k \geq 1 \tag{3.4}$$

$$B_i^0(t) = \begin{cases} 1 & t_i \leq t < t_{i+1} \\ 0 & \text{else} \end{cases}$$

which implies $B_i^k = 0$ for $t \notin [t_i, t_{i+1})$ and $B_i^k > 0$ else. The spline then is defined by the linear combination $S(t) = \sum_{i=0}^{p-1} C_i^3 B_i^3(t)$ where C_i^3 is a weight for the basis and p denotes the number of knots. Using this recursive definition, weights C_i^3 and basis functions $B_i^3(t)$ can be created, defining $S(t)$ with the previously defined cubic spline properties [De Boor et al., 2001, Cheney and Kincaid, 2012].

For fixed p, the log-hazard function $\alpha(t|H_t)$ is modeled using

$$\alpha(t|H_t) = \sum_{j=1}^{p} \beta_j B_j(t), \text{ for } t \geq 0 \tag{3.5}$$

where $1 \leq p < \infty$, $\beta_1, \ldots, \beta_p$ are fixed coefficients and $B_1, \ldots, B_p$ are chosen basis functions of functional space G. Since $t \geq 0$, G is a p-dimensional linear space of functions on $[0, \infty)$. The flexibility of the model is determined by the form and number of the basis functions, which changes the space G to encompass more general log-hazard functions. The authors examine two different formulations, each of which uses cubic splines, though one of which includes two additional basis functions. These two functions are $B_{-1}(t) = \log[t/(t + c)]$ and $B_0 = \log(t + c)$ for $t > 0$ and 0 otherwise, where $c > 0$ is fixed. The corresponding functions form a basis for $G \cup \{B_{-1}, B_0\}$, where $\{B_{-1}, B_0\}$ is the 2-dimensional linear space of functions spanned by $B_{-1}(t)$ and $B_0(t)$. Setting the number of cubic splines to $p = K - 2$, using the basis set $\{B_{-1}, \ldots, B_{K-2}\}$

results in the family of log-hazard functions encompassed by the model to be defined by ϑ. The collection of linear spaces spanned by $G \cup \{B_{-1}, B_0\}$ defines ϑ.

The inclusion of the two log basis functions expands the family of log-hazard functions to include those from commonly used distributions in point process analysis, such as the Weibull and Pareto distributions. Specifically, these two functions better model heavy-tailed distributions in relation to the commonly used exponential distribution.

The main parameters to select are p and the "knot" locations for the basis functions, with β_i for $i = -1, 0, \ldots, p$ and c to be estimated from the data. Define knots t_i such $0 < t_1 < \ldots < t_{p-1} < \infty$. Functions B_j for $j = 1, \ldots, p$ denote the B spline functions for a cubic spline with knots $\{0, t_1, \ldots, t_{p-1}\}$. The weights $\beta_1, \ldots, \beta_p$ represent the B spline weights from Equation 3.4, which are to estimated based on the observed data and selected knots.

The authors specify an algorithm to select the knots based on the observed data. An initial set of three knots are placed at the three quartiles of the set of times where a spike occurs. Then the following stepwise process is used to determine the optimal set of knots and their locations. Suppose m knots are selected in the current iteration (after the inital iteration, $m = 3$ for example) denoted $0 < t_1 < \ldots < t_m < \infty$. Let $l_i = 6 + \max_{1 \le j \le n} \tau_j \le t_i$ for $i = 1 \ldots, m$, $u_i = -6 + \min_{1 \le j \le n} \tau_j \ge t_i$ for $i = 1 \ldots, m-1$, $l_0 = 1$ and $u_k = n$. For $i = 0, \ldots, m$ such that $u_i \ge l_i$ compute the Rao statistic r_i for the model with $(t - \tau_{j_i})_+$ as the added basis function with $j_i = [(l_i + u_i)/2]$. If there is no such i, no knot is added. The Rao statistic $r_i = [S(\hat{\beta})]_m \sqrt{[\boldsymbol{I}^{-1}(\hat{\beta})]_{mm}}$, where $\hat{\beta}$ indicates the estimate of β from the log-hazard function in equation 3.5 and $S(.)$ and $\boldsymbol{I}(.)$ are the score vector and information matrix respectively.

If such an i exists, a new knot in the interval $[\tau_{(l_i^*)}, \tau_{(u_i^*)}]$ where $i^* = \arg\max_i |r_i|$. Then Rao statistic r_l is computed for the model with $(t - \tau_l)_+$ with $l = [(l_{i^*} + j_{i^*}/2]$ as the added basis function, and statistic r_u for the model with $(t - \tau_u)_+$ with $u = [(j_{i^*} + u_{i^*})/2]$ as the added basis function. These Rao statistics are then compared to decide if the knot location search is finished or if it continues in the same recursive partitioning format. If $|r_{i^*}| \ge |r_l|$ and $|r_{i^*}| \ge |r_u|$, the new knot is placed at τ_{i^*}. Otherwise, the search continues based on the comparison of these two

statistics. The algorithm continues until 1) iteration occurs where no i such that $u_i \geq l_i$ exist, or 2) the number of basis functions $p = p_{max}$ where $p_{max} = (4n^{1/5}, n/4, 30)$. Please see Kooperberg et al. [1995] for more details. Once the knots and basis functions are fixed, an iterative procedure using an adjusted form of the Newton-Raphson algorithm is done to estimate β and c (if flexible tail basis functions are used).

3.3.3 Colored ICA with HEFT

Consider the latent variable model $\boldsymbol{X} = h(\boldsymbol{S})$ where $\boldsymbol{X}$ denotes the observed data matrix and R by N matrix $\boldsymbol{S}$ which contains the latent variable realizations. The objective is to estimate the properties of transformation $h(.)$ and predict $\boldsymbol{S}$ from $\boldsymbol{X}$; this is often referred to as *blind source separation* in signal processing [Hyvärinen and Oja, 1997]. We assume the number of spatial locations $V = R$ and drop V from the rest of the section. Assuming $\boldsymbol{X}$ denotes a spatio-temporal matrix, $\boldsymbol{S}$ denotes the realizations of temporal *latent components*, with each row reflecting a separate component. Following the notation in sections 3.3.2 and 3.3.1, we define these temporal components in terms of the *latent spike times* $\tau_{i,j}$, which denote the time of the j^{th} event (*latent spike*) for source i for $i = 1, \ldots, R$. Correspondingly, the j^{th} ISI in the i^{th} component is denoted by $u_{i,j} = \tau_{i,j} - \tau_{i,j-1}$ where $\tau_{i,0} \equiv 0$.

3.3.3.1 Preliminary Model

First, we assume all sources have the same number N of latent spikes to simplify the notation. This restriction is lifted later in this section. Thus, matrix $\boldsymbol{S} = [S_1, \ldots, S_R]^T$ is R by N, where $S_i = (\tau_{i,1}, \ldots, \tau_{i,N})$ with $\tau_{i,j} < \tau_{i,j+1}$ for $i = 1, \ldots, R$ and $j = 1, \ldots, N-1$. The components are assumed to be independent, with $S_i \perp S_j$ for $i, j = 1, \ldots, R$ and $i \neq j$. Since each component is a point process, realizations within a given component are statistically dependent. The temporal source matrix $\boldsymbol{S}$ can also be represented in terms of sequences of spikes (0 and 1), spike times, or ISIs, as the transformation between any of these domains is one-to-one, with T denoting the end of study.

By independence, the joint distribution of $\boldsymbol{S}$ is $f(s_1, \ldots, s_R) = \prod_{i=1}^{R} f_{S_i}(s_i)$ where s_i is a fixed vector of length N, and $f_{S_i}(s_i)$ is the joint distribution of S_i evaluated at s_i for $i = 1, \ldots, R$. The joint distribution of the entries of S_i can be written in terms of the joint distribution of the ISIs, where $f_{S_i}(s_i) = f_{u_i}(u_i|N_i(T) = N)$, where $u_i = (u_{i,1}, \ldots, u_{i,N})$ and $N_i(T)$ denotes the random variable of the number of spikes in latent component i by time T. This can be expressed as a function of the log conditional intensity function for $u_i|N_i(T) = n_i$, as seen in Equation 3.3. By independence of the latent components

$$\begin{aligned} f(s_1, \ldots, s_R) &= \prod_{i=1}^{R} f_{S_i}(s_i) \\ &= \prod_{i=1}^{R} f_{u_i}(u_i|N_i(T) = N) \\ &= f(u_1, \ldots, u_R|N). \end{aligned} \tag{3.6}$$

From this formulation, we can now write the likelihood as a function of observed data $\boldsymbol{X}$.

From dimensions defined above, observed data $\boldsymbol{X}$ is V by T. To map $\boldsymbol{S}$ to $\boldsymbol{X}$, transformation $h(.)$ has to be defined and the two temporal domains between $\boldsymbol{X}$ (T) and $\boldsymbol{S}$ (N) need to harmonized. To simplify notation, $\left\{\{\tau_{i,j}\}_{j=1}^{N}\right\}_{i=1}^{R} \subset Z_+$ (positive integers) is assumed. First, the temporal indices are expressed in terms of the source spike times $\{\tau_i\}_{i=1}^{R}$ as follows:

$$\boldsymbol{X} = \begin{pmatrix} x_{1,1} & \ldots & x_{1,\tau_{1,1}} & x_{1,[\tau_{1,1}+1]} & \ldots & x_{1,\tau_{1,2}} & \ldots & x_{1,\tau_{1,N}} & \ldots & x_{1,T} \\ x_{2,1} & \ldots & x_{2,\tau_{2,1}} & x_{2,[\tau_{2,1}+1]} & \ldots & x_{1,\tau_{2,2}} & \ldots & x_{1,\tau_{2,N}} & \ldots & x_{2,T} \\ \vdots & \vdots & \vdots & \vdots & \vdots & \vdots & \vdots & \vdots & \vdots & \vdots \\ x_{R,1} & \ldots & x_{R,\tau_{R,1}} & x_{R,[\tau_{R,1}+1]} & \ldots & x_{R,\tau_{R,2}} & \ldots & x_{R,\tau_{R,N}} & \ldots & x_{R,T} \end{pmatrix}$$

First, the temporal dimensions between $\boldsymbol{X}$ and $\boldsymbol{S}$ are harmonized by transforming $\boldsymbol{X}$ to $\widetilde{\boldsymbol{X}}$. Matrix is defined as

$$\widetilde{\boldsymbol{X}} = \begin{pmatrix} \tilde{x}_{1,1} & \tilde{x}_{1,2} & \dots & \tilde{x}_{1,N} \\ \tilde{x}_{2,1} & \tilde{x}_{2,2} & \dots & \tilde{x}_{2,N} \\ \vdots & \vdots & \vdots & \vdots \\ \tilde{x}_{R,1} & \tilde{x}_{R,2} & \dots & \tilde{x}_{R,N} \end{pmatrix}$$

where $\tilde{x}_{i,j} = \sum_{t \in \Theta_{i,j}} \gamma_{i,t}(x_{i,t}) * t$ where $\Theta_{i,j} = \{t\text{: } \tilde{\tau}_{i,[j-1]} < t \leq \tilde{\tau}_{i,j}\}$, for $i = 1, \dots, R$ and $j = 1, \dots, N$. Starting time $\tau_{i,0} \equiv 0$. Times $\left\{ \{\tilde{\tau}_{i,j}\}_{j=1}^{N} \right\}_{i=1}^{R} \subset Z_+$ denote spikes in the *observed data* $\boldsymbol{X}$, which may not be the same times as the source spikes of interest. That is, $\widetilde{\boldsymbol{X}}$ aggregates the data in each row of $\boldsymbol{X}$ by computing weighted averages across the time span. These averages are computed by partitioning the time span, starting at a given *observed* spike time and then ending at the next observed spike time. The weights are defined by $\left\{ \{\gamma_{i,t}(x_{i,t})\}_{t=1}^{T} \right\}_{i=1}^{R} \subset R_{0+}$ (non-zero real numbers) which may depend on the observed values $\{x_{i,t}\}$.

Finally, we can define the ISIs for the observed spikes and latent source spikes by $\tilde{u}_{i,j} = \tilde{\tau}_{i,j} - \tilde{\tau}_{i,j-1}$ and $u_{i,j} = \tau_{i,j} - \tau_{i,j-1}$ respectively. Using the ISI formulation, we define the matrices $\widetilde{\boldsymbol{U}}$ and $\boldsymbol{U}$ by

$$\widetilde{\boldsymbol{U}} = \begin{pmatrix} \tilde{u}_{1,1} & \tilde{u}_{1,2} & \dots & \tilde{u}_{1,N} \\ \tilde{u}_{2,1} & \tilde{u}_{2,2} & \dots & \tilde{u}_{2,N} \\ \vdots & \vdots & \vdots & \vdots \\ \tilde{u}_{R,1} & \tilde{u}_{R,2} & \dots & \tilde{u}_{R,N} \end{pmatrix}$$

and

$$\boldsymbol{U} = \begin{pmatrix} u_{1,1} & u_{1,2} & \dots & u_{1,N} \\ u_{2,1} & u_{2,2} & \dots & u_{2,N} \\ \vdots & \vdots & \vdots & \vdots \\ u_{R,1} & u_{R,2} & \dots & u_{R,N} \end{pmatrix}$$

respectively. We can model the relationship between the two by the usual ICA model $\widetilde{\boldsymbol{U}} = \boldsymbol{A}\boldsymbol{U}$ where matrix $\boldsymbol{A}$ is R by R. This matrix mixes the latent source ISIs found in $\boldsymbol{U}$ and is referred to as the *mixing matrix*. Following the usual ICA conventions, it is assumed that $\boldsymbol{A}$ is an orthogonal matrix, i.e. $\boldsymbol{A}^{-1} = \boldsymbol{A}^T \equiv \boldsymbol{W}$, where $\boldsymbol{W}$ is referred to the *unmixing matrix*.

Using the Jacobian method for the joint distribution of the transformation of a set of random variables, the joint distribution of $\widetilde{\boldsymbol{U}}$, denoted $f_{\widetilde{\boldsymbol{U}}}(x)$, is

$$f_{\widetilde{\boldsymbol{U}}}(\tilde{u}) = \prod_{i=1}^{R} f_{U_i}(u_i)|J_{h^{-1}}(\tilde{u}_{11}, \ldots, \tilde{u}_{R*N})|^{-1}$$

where x is a $R * N$ long vector of fixed values and $J_{h^{-1}}(\tilde{u}_{11}, \ldots, \tilde{u}_{R*N})$ denotes the Jacobian matrix for inverse transform $h^{-1}(\widetilde{\boldsymbol{U}})$. Since the inverse transform is linear using matrix $\boldsymbol{W}$, the Jacobian is $\det(\boldsymbol{W})$. Since $\boldsymbol{W}$ is orthogonal, $|\det(\boldsymbol{W})| = 1$ and can be dropped. This implies

$$\prod_{i=1}^{R} f_{U_i}(u_i)|J_{h^{-1}}(\tilde{u}_{11}, \ldots, \tilde{u}_{R*N})|^{-1} = \prod_{i=1}^{R} f_{U_i}(u_i)$$

Next, we express the densities of the latent components in terms of their ISIs using Equation 3.3. Under the HEFT model, the log-hazard function for U_i at time t is given by $\alpha_i(t) = \sum_{j=-1}^{p} \beta_{i,j} B_{i,j}(t)$ from Equation 3.5, using the added basis functions for flexible tail modeling (history H_t is dropped for simplicity). Then from Equation 3.3, the joint density of $\widetilde{\boldsymbol{U}}$ can be written as

$$f_{\widetilde{\boldsymbol{U}}}(\tilde{u}) = \prod_{i=1}^{R}\prod_{k=1}^{N} \exp\{\alpha_i(u_{i,k})\} \exp\Big\{ - \int_0^{u_{i,k}} \exp\{\alpha_i(s)\} ds \Big\}. \tag{3.7}$$

To express Equation 3.7 as a log-likelihood, $\{u_{i,k}\}$ need to be expressed in terms of $\widetilde{\boldsymbol{U}}$ and parameters $\boldsymbol{W}$, $\{B_{i,j}(t)\}$, and $\{\beta_{i,j}\}$. This can be done using the unmixing transformation $\boldsymbol{U} = \boldsymbol{W}\widetilde{\boldsymbol{U}}$, with $u_{i,k} = \sum_{l=1}^{R} W_{i,l}\tilde{u}_{l,k}$ where $W_{i,j}$ denotes the corresponding entry in $\boldsymbol{W}$. This results in the

following log-likelihood

$$L(\boldsymbol{W}|\alpha_1,\ldots,\alpha_R,u_1,\ldots,u_R) = \tag{3.8}$$
$$\sum_{i=1}^{R}\sum_{k=1}^{N}\left[\alpha_i(\Sigma_{l=1}^{R}w_{i,l}\tilde{u}_{l,k}) - \int_0^{w_{i,l}\tilde{u}_{l,k}}\exp\{\alpha_i(s)\}ds\right]$$

where log intensity functions $\alpha_1,\ldots,\alpha_R$ are defined as functions of $\boldsymbol{W}$, $\widetilde{\boldsymbol{X}}$, parameters $\left\{\{\beta_{i,j}\}_{j=-1}^{p_i}\right\}_{i=1}^{R}$, and fixed basis functions $\left\{\{B_{i,j}(t)\}_{j=-1}^{p_i}\right\}_{i=1}^{R}$.

To estimate these parameters in the model, we minimize the negative log-likelihood while ensuring the unmixing matrix is orthogonal. This is done in an iterative manner as done by Lee et al. [2011], alternating between updating the ICA unmixing matrix and estimating the log-intensity function using HEFT for a fixed unmixing matrix. Beginning with an initial value for the unmixing matrix $\boldsymbol{W_0}$, the corresponding initial latent ISIs can be computed as $\boldsymbol{U_0} = \boldsymbol{W_0}\widetilde{\boldsymbol{U}}$ along with the corresponding ISIs $u_{0,1},\ldots,u_{0,R}$, resulting in the initial step's estimate of the log-intensity function using HEFT.

To update $\boldsymbol{W}$ based on the estimated log-intensity function, the function in Equation 3.8 is minimized. Note the unmixing matrix is embedded in the log-intensity function domain where this function is fixed in this step following HEFT. Since this function is modeled using cubic splines, the objective function 3.8 in this minimization step is nonlinear with respect to $\boldsymbol{W}$. We use the optimization method from Hastie and Tibshirani [2002] for the estimation. For a single ISI in component i, the likelihood as a function of ISIS t can be defined by

$$L_i(t|\alpha_i) = \alpha_i(t) - \int_0^t \exp\{\alpha_i(s)\}ds.$$

Denote the first and second derivatives of $L_i(t|\alpha_1,\ldots,\alpha_R)$ with respect to t, evaluated at $t = (u_{0,i})$ as $\dot{L}_i(u_{0,i}|\alpha_i)$ and $\ddot{L}_i(u_{0,i}|\alpha_i)$ respectively. Note since $u_{0,i}$ is a vector, from Equation 3.8, $L_i(u_{0,i}|\alpha_i)$ is a sum across j from 1 to N of $L_i(u_{0,i}(j)|\alpha_i$ where $u_{0,i}(j)$ denotes the jth ISI for the

ith component. Then, the one-step update for $\boldsymbol{W_i}$, the i^{th} row of is $\boldsymbol{W}$, is

$$\widehat{\boldsymbol{W_i}} = ave\{\widetilde{\boldsymbol{U}}\dot{L}_i(u_{0,i}|\alpha_1, \ldots, \alpha_R)\} - ave\{\ddot{L}_i(u_{0,i}|\alpha_1, \ldots, \alpha_R)\}W_{0,i} \tag{3.9}$$

where $W_{0,i}$ denotes i^{th} row of the previous iteration's estimate for the unmixing matrix, and $\tilde{\alpha}_i$ denotes the current iteration's estimate for for the i^{th} component's log-intensity function from HEFT. The derivatives of $L_i(t|\alpha_i)$ are evaluated at the initial estimates for the latent source ISIs, denoted by $u_{0,i}$ for source $i = 1, \ldots, R$. The first and second derivatives are averaged across their ISIs (N of them), as denoted by ave, resulting in a scalar.

Since $\alpha_i(t)$ are cubic splines, their derivatives can be shown to be quadratic splines from the following relationship: [De Boor et al., 2001]

$$\frac{d}{dt}B_i^k(t) = k\left(\frac{B_i^{k-1}(t)}{t_{i+k} - t_i} - \frac{B_{i+1}^{k-1}(t)}{t_{i+k+1} - t_{i+1}}\right) \text{ for } k \geq 2.$$

The second derivative can then be found using this relationship. This holds for the polynomial part of the HEFT formulations, with the derivatives of the two additional log basis functions in Equation 3.5 done separately. The derivative of the integral in Equation 3.8 with respect to t can be found using the Fundamental Theorem of Calculus.

Following Lee et al. [2011], this iterative process continues until a maximum number of iterations or a convergence criterion based on Amari's distance has been reached. For two R by R matrices $\boldsymbol{W_1}$ and $\boldsymbol{W_2}$, Amari's distance is defined as

$$d_{\text{Amari}}(\boldsymbol{W_1}, \boldsymbol{W_2}) = \frac{1}{R}\sum_{i=1}^{M}\left(\frac{\sum_{j=1}^{R}|a_{ij}|}{\max_j|a_{ij}|} - 1\right) + \frac{1}{R}\sum_{j=1}^{M}\left(\frac{\sum_{i=1}^{R}|a_{ij}|}{\max_i|a_{ij}|} - 1\right) \tag{3.10}$$

where a_{ij} is the ijth element of $\boldsymbol{W_1}\boldsymbol{W_2}^{-1}$. The convergence criterion is satisfied once this metric reaches a chosen threshold. The complete iterative algorithm is summarized as follows:

Algorithm The cICA-HEFT Algorithm

1. Determine weights $\left\{\{\gamma_{i,t}(x_{i,t})\}_{t=1}^{T}\right\}_{i=1}^{R}$, corresponding observed spike times $\left\{\{\tilde{\tau}_{i,j}\}_{j=1}^{N}\right\}_{i=1}^{R}$, and matrix $\tilde{\boldsymbol{X}}$

Initialize $\tilde{\boldsymbol{W}}$.

While the Amari distance (Equation 3.10) between $\tilde{\boldsymbol{W}}$ and $\hat{\boldsymbol{W}}$ is greater than the convergence threshold,

1. Estimate the latent components $\boldsymbol{S}$ by $\tilde{\boldsymbol{S}} = \tilde{\boldsymbol{W}}\tilde{\boldsymbol{X}}$
2. Estimate log-intensity functions $\tilde{\alpha}_1, \ldots, \tilde{\alpha}_R$ for each component using HEFT with $\tilde{\boldsymbol{S}}$
3. Update $\tilde{\boldsymbol{W}}$ (denoted $\widehat{\boldsymbol{W}}$) via updating step in 3.9 with log-intensity functions $\tilde{\alpha}_1, \ldots, \tilde{\alpha}_R$ fixed
4. Orthogonalize $\widehat{\boldsymbol{W}}$: Compute its SVD, $\widehat{\boldsymbol{W}} = \boldsymbol{U_W D V}^T$ and replace $\widehat{\boldsymbol{W}} \to \boldsymbol{U_W V}^T$

The spikes in the observed data $\left\{\{\tilde{\tau}_{i,j}\}_{j=1}^{N}\right\}_{i=1}^{R}$ as well as the weights $\left\{\{\gamma_{i,t}(x_{i,t})\}_{t=1}^{T}\right\}_{i=1}^{R}$ need to determined. The observed data spike times will be determined by thresholding the observed values in $\boldsymbol{X}$, that is $\tilde{\tau}_{i,j} = \{t : |x_{i,t}| > \delta_i\}$ where $\{\delta_i\}_{i=1}^{R} \subset R_+$ (positive real numbers) denote the per-row thresholds. If components have different numbers of spikes, the ISIs can be zeropadded at the end for each component so that $\boldsymbol{U}$ follows the convention of a matrix, witht the number of columns equal to the largest number of spikes among the components.

For simplicity, $\delta_1 = \ldots = \delta_R = \delta > 0$. The observed ISIs immediately follow. We discuss various models for the weights which reflect the relationship between the observed data spikes and the underlying ICA model containing latent spikes of interest (e.g. spikes in neuron populations).

3.3.3.2 Model 1: Maximum Observed Value

We begin with the simplest model, where $\tilde{x}_{i,k} = \tilde{\tau}_{i,j}$ for $i = 1, \ldots, R$ and $j = 1, \ldots, N$. That is,

$$\widetilde{\boldsymbol{X}} = \begin{pmatrix} \tilde{\tau}_{1,1} & \tilde{\tau}_{1,2} & \dots & \tilde{\tau}_{1,N} \\ \tilde{\tau}_{2,1} & \tilde{\tau}_{2,2} & \dots & \tilde{\tau}_{2,N} \\ \vdots & \vdots & \vdots & \vdots \\ \tilde{\tau}_{R,1} & \tilde{\tau}_{R,2} & \dots & \tilde{\tau}_{R,N} \end{pmatrix}$$

which from the ICA models implies $\tilde{\tau}_{i,j} = \sum_{l=1}^{R} A_{i,l}\tau_{l,j}$ where $A_{i,j}$ denotes the corresponding entry in $\boldsymbol{A}$. After thresholding, the model can then fit directly using the observed spike times contained in $\widetilde{\boldsymbol{X}}$ using the cICA-HEFT algorithm defined in Section 3.3.3.1.

3.3.3.3 Model 2: Auto-Regressive Model

A more realistic model would be to model the observed fluorescence signal using an auto-regression (AR) model. This is often used in the literature to model the relationship between fluorescence and underlying calcium when analyzing calcium imaging data [Jewell et al., 2020]. In the framework presented above, the observed data $\boldsymbol{X}$ could be modeled using

$$X_{i,t} = \gamma_i X_{i,t-1} + \epsilon_t \tag{3.11}$$

for $i = 1, \dots, R$ and $t = 2, \dots, N$ with ϵ_t denoting the residual (also called innovation). Using this model, the trend in the fluorescence could be extracted by $\hat{X}_{i,t} = \hat{\gamma}_i \hat{X}_{i,t-1}$ where $\hat{\gamma}_i$ denotes the estimated parameter and $\hat{X}_{i,t}$ denotes the predicted fluorescence. Using the corresponding matrix of predicted values from the AR model $\widehat{\boldsymbol{X}}$, the same thresholding process used before could be done to estimate the locations of the calcium spikes related to the underlying neural spikes $\widetilde{\boldsymbol{X}}$ and $\{\tilde{\tau}_{i,j}\}$. The cICA-HEFT model would then be fit to this matrix to estimate the independent components containing the estimated neural spike times and to estimate the mixing matrix.

3.4 Simulation Studies

The proposed model was evaluated in a set of simulation studies, reflecting the simple model described in Section 3.3.3.2, where the aim was to disentangle mixtures of latent spikes. The data were simulated as follows. We considered an observed data matrix, whose entries consist of times between observed spikes (for example, fluorescence spikes). That is, observed data $\boldsymbol{X} = \boldsymbol{AS}$ where $\boldsymbol{X}$ was R by N, with R denoting the number of channels and N denoting the number of observed spikes, assuming an equal number of observed spikes in each channel for simplicity. Mixing matrix $\boldsymbol{A}$ was R by R, with $R = 2$. Matrix $\boldsymbol{S}$ is R by N, with each row's entries denoting the times between the the N spikes for the respective channel, with $N = 200$. The primary goal was to accurately estimate the mixing matrix in order to identify the multi-channel properties of the data. As stated in Section 3.3.3.1, it was assumed that $\boldsymbol{A}$ is orthogonal, implying unmixing matrix $\boldsymbol{W} = \boldsymbol{A}^T$.

To generate $\boldsymbol{A}$, R^2 entries were generated independently from the Uniform[1,2] distribution, which were then converted into a R by R matrix. This matrix was then orthogonalized using SVD [Hastie and Tibshirani, 2002]. To generate the latent ISIs in $\boldsymbol{S}$, R such independent ISIs of length N were generated. Two sets of distributions were considered when generating these intervals. The first was an exponential distribution, with a mean of 30 used for the first set (first row of $\boldsymbol{S}$) and a mean of 10 for the second set (second row of $\boldsymbol{S}$). The second was a gamma distribution, with a shape parameter of 30 used for the first set and 10 used for the second set, and a rate parameter of 2 used for both to differentiate it from the exponential distribution. In all cases, the N intervals within a set were generated independently, as were the R sets. This process was repeated 1000 times, with $\boldsymbol{S}$ fixed across the simulations and mixing matrix $\boldsymbol{A}$ randomly varying, as the main aim to evaluate the accuracy of the mixing matrix estimation with the proposed method. For comparison, two standard ICA methods not explicitly designed for identifying latent time intervals, cICA [Lee et al., 2011] and fastICA Hyvärinen and Oja [2000], were also used on

each simulated dataset. All three methods were evaluated based on the Amari distance between the estimated mixing matrix and corresponding simulated mixing matrix.

The results for both scenarios are provided in Figure 3.2. Boxplots of the Amari distances across the 1000 simulated datasets, from each of the three considered methods were created. The plot consists of two panels, with the left showing the Amari distance distributions for each of the three methods across the simulations under the specified exponential distribution for the latent spike ISIs. The right panel shows the same, but under the specified gamma distribution. The accuracies of $\boldsymbol{S}$ were not examined as the accuracy of the independent components is directly related to the accuracy of the mixing matrix (due to $\boldsymbol{S} = \boldsymbol{W}\boldsymbol{X}$) and since the multi-channel estimation of the method was the main trait of interest.

The proposed method showed an Amari distance distribution shifted towards zero compared to the other two methods (especially fastICA) under the exponential distribution scenario, with the median error below 0.10. The proposed method performed similarly in both the exponential and gamma distribution scenario, with cICA showing a very similar Amari distance distribution in the gamma scenario, but fastICA again having noticeably higher Amari distance. Note that the additional log terms for the HEFT model fit described in Section 3.3.2 were not used for simplicity, which lowers the ability for the model to reflect heavier tailed distributions (such as the gamma distribution).

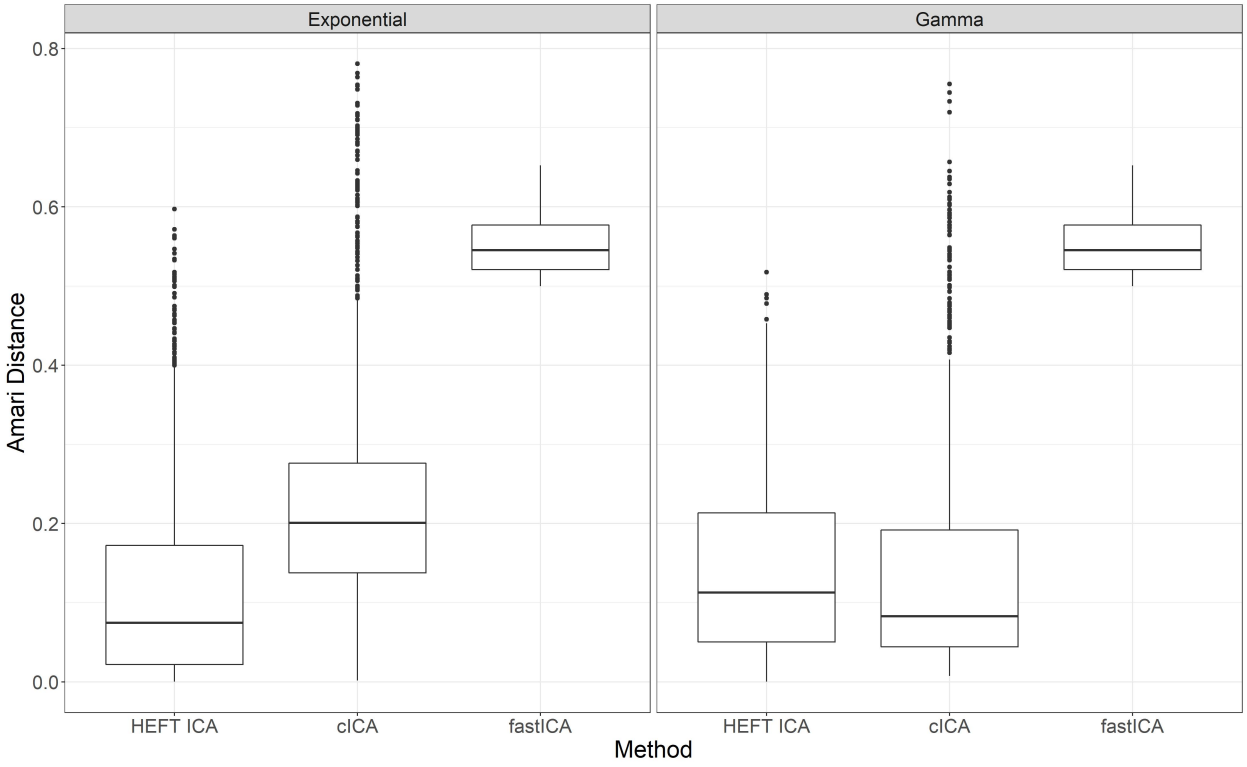

Figure 3.2: Estimation results of the mixing matrices from simulated data, across 1000 simulations.

3.5 Discussion and Future Research

Neural imaging data pose a number of unique challenges for statistical analysis due to its high dimension, high degree of noise, nonstationarity, and complex dependency structure in time and space. As a result, methods which can accurately filter out the meaningful relationships in the data despite these challenges are required. Parametric modeling is often used to simplify the complex structure of the data, though that opens up the results to bias due to model misspecification. Nonparametric methods are optimal due to these complixities to reduce this bias, though these methods need to provide interpretable results and high accuracy which can be difficult due to the discussed complications without resorting to modeling.

Neural spike train analyses are highly susceptible to these complications due to their high temporal resolution and large amount of noise. Inferring which observed spikes in the fluorescence reflect underlying spikes in neural activity is challenging due to the noise-related spikes in the fluorescence, the nonlinear relationship between the calcium concentration and the chosen GECI, and the relatively small amount of calcium released by isolated spikes. A further challenge is jointly estimating activity from multiple neurons. This joint modeling would 1) provide a framework for estimating and testing relationships between neuron cell populations and also 2) perhaps improve single-neuron activity estimation accuracy by leveraging information from nearby neurons. Methods developed in literature to this point generally focus on the single-neuron problem.

Various statistical methods have been developed to analyze this data, including CNMF, parametric modeling of the underlying point process, Bayesian methods, and penalized latent variable models. Beyond the single-neuron limitation of many of these methods, the parametric models used for many of the matrix factorization methods impose assumptions which may be too limiting to accurately reflect calcium imaging data (e.g. Normal distribution, Poisson processes, etc.). To avoid the use of parametric modeling while still reflecting the point process structure of the underlying neuronal spiking, we propose an extension to ICA which uses a nonparametric spline-

based model for estimation of the log-hazard function. This log-hazard represents the pattern in the timing of the neural spikes underlying the fluorescence signal. This allows underlying components of neural spiking to be identified from the calcium image using the ICA model formulation, estimated in a nonparametric fashion. The use of ICA also allows multiple neuron populations to be analyzed jointly in the model, potentially providing previous discussed benefits. Furthermore, this represents the first model found in the literature for ICA designed for nonnegative integers which is does not assume a parametric form for the latent components.

There are a number of areas for future research based on the method and results presented in this research. First, the method was only evaluated in the case where a dataset of observed spikes is available, with the goal of inferring the latent spikes of interest from those that are observed. Often, these observed spikes need to be defined or inferred based on observations in the data on a continuous scale. One example is calcium imaging data, where a set of spikes is not explicitly, but instead a continuous fluorescence signal. This research proposes models to transform from this continuous signal to a set of observed spikes, however they need to be evaluated and perhaps expanded on to be suitable for use in calcium imaging data in its raw form. Finally, the proposed method was only evaluated in a small set of simulated scenarios, and not in any real imaging data. The simulation studies done here need to expanded to confidently establish the method's properties empirically, along with exploring its utility in real imaging data.

REFERENCES

A. Abou Elseoud, H. Littow, J. Remes, T. Starck, J. Nikkinen, J. Nissilä, O. Tervonen, M. Timonen, and V. J. Kiviniemi. Group-ica model order highlights patterns of functional brain connectivity. *Frontiers in Systems Neuroscience*, 5:37, 2011.

M. B. Ahrens, M. B. Orger, D. N. Robson, J. M. Li, and P. J. Keller. Whole-brain functional imaging at cellular resolution using light-sheet microscopy. *Nature Methods*, 10(5):413–420, 2013.

E. A. Allen, E. Damaraju, S. M. Plis, E. B. Erhardt, T. Eichele, and V. D. Calhoun. Tracking Whole-Brain Connectivity Dynamics in the Resting State. *Cerebral Cortex*, 24(3), 2012. doi: 10.1093/cercor/bhs352. URL `https://dx.doi.org/10.1093/cercor/bhs352`.

Y. Aoki, R. Ishii, R. D. Pascual-Marqui, L. Canuet, S. Ikeda, M. Hata, K. Imajo, H. Matsuzaki, T. Musha, T. Asada, et al. Detection of eeg-resting state independent networks by eloreta-ica method. *Frontiers in human neuroscience*, 9:31, 2015.

P. Bai, H. Shen, X. Huang, and Y. Truong. A supervised singular value decomposition for independent component analysis of fmri. *Statistica Sinica*, pages 1233–1252, 2008.

E. Barshan, A. Ghodsi, Z. Azimifar, and M. Z. Jahromi. Supervised principal component analysis: Visualization, classification and regression on subspaces and submanifolds. *Pattern Recognition*, 44(7):1357–1371, 2011.

C. F. Beckmann and S. M. Smith. Probabilistic independent component analysis for functional magnetic resonance imaging. *IEEE Transactions on Medical Imaging*, 23(2):137–152, 2004.

B. Biswal, F. Zerrin Yetkin, V. M. Haughton, and J. S. Hyde. Functional connectivity in the motor cortex of resting human brain using echo-planar mri. *Magnetic Resonance in Medicine*, 34 (4):537–541, 1995.

K. A. Bollen. *Structural Equations with Latent Variables*. Wiley, 1989.

C. Bordier, M. Dojat, and P. Lafaye de Micheaux. Temporal and spatial independent component analysis for fmri data sets embedded in the analyzefmri r package. *Journal of Statistical Software*, 44, 2010. doi: 10.18637/jss.v044.i09.

D. R. Brillinger. *Time Series: Data Analysis and Theory*. SIAM, 2001.

P. J. Brockwell, R. A. Davis, and S. E. Fienberg. *Time Series: Theory and Methods*. Springer Science & Business Media, 1991.

E. N. Brown, R. Barbieri, V. Ventura, R. E. Kass, and L. M. Frank. The time-rescaling theorem and its application to neural spike train data analysis. *Neural Computation*, 14(2):325–346, 2002.

G. D. Brown, S. Yamada, and T. J. Sejnowski. Independent component analysis at the neural cocktail party. *Trends in Neurosciences*, 24(1):54–63, 2001.

R. L. Buckner, F. M. Krienen, and B. T. Yeo. Opportunities and limitations of intrinsic functional connectivity mri. *Nature Neuroscience*, 16(7):832–837, 2013.

G. Buzsáki and A. Draguhn. Neuronal oscillations in cortical networks. *Science*, 304(5679): 1926–1929, 2004.

V. D. Calhoun and T. Adali. Unmixing fmri with independent component analysis. *IEEE Engineering in Medicine and Biology Magazine*, 25(2):79–90, 2006.

V. D. Calhoun, J. Liu, and T. Adalı. A review of group ica for fmri data and ica for joint inference of imaging, genetic, and erp data. *Neuroimage*, 45(1):S163–S172, 2009.

A. Catarino, A. Andrade, O. Churches, A. P. Wagner, S. Baron-Cohen, and H. Ring. Task-related functional connectivity in autism spectrum conditions: an eeg study using wavelet transform coherence. *Molecular Autism*, 4(1):1, 2013.

C. Chang and G. H. Glover. Time–frequency dynamics of resting-state brain connectivity measured with fmri. *Neuroimage*, 50(1):81–98, 2010.

M. Chawla. Pca and ica processing methods for removal of artifacts and noise in electrocardiograms: A survey and comparison. *Applied Soft Computing*, 11(2):2216–2226, 2011.

J.-L. Chen, T. Ros, and J. H. Gruzelier. Dynamic changes of ica-derived eeg functional connectivity in the resting state. *Human Brain Mapping*, 34(4):852–868, 2013.

Z. Chen. An overview of bayesian methods for neural spike train analysis. *Computational Intelligence and Neuroscience*, 2013, 2013.

E. W. Cheney and D. R. Kincaid. *Numerical Mathematics and Computing*. Cengage Learning, 2012.

A. S. Choe, C. K. Jones, S. E. Joel, J. Muschelli, V. Belegu, B. S. Caffo, M. A. Lindquist, P. C. van Zijl, and J. J. Pekar. Reproducibility and temporal structure in weekly resting-state fmri over a period of 3.5 years. *PloS one*, 10(10):e0140134, 2015.

Y.-h. Chou, L. P. Panych, C. C. Dickey, J. R. Petrella, and N.-K. Chen. Investigation of long-term reproducibility of intrinsic connectivity network mapping: a resting-state fmri study. *American Journal of Neuroradiology*, 33(5):833–838, 2012.

N. W. Churchill, G. Yourganov, A. Oder, F. Tam, S. J. Graham, and S. C. Strother. Optimizing preprocessing and analysis pipelines for single-subject fmri: 2. interactions with ica, pca, task contrast and inter-subject heterogeneity. *PloS One*, 7(2):e31147, 2012.

M. X. Cohen. *Analyzing Neural Time Series Data: Theory and Practice*. MIT Press, 2014.

D. M. Cole, S. M. Smith, and C. F. Beckmann. Advances and pitfalls in the analysis and interpretation of resting-state fmri data. *Frontiers in systems neuroscience*, 4:8, 2010.

C. Craddock, Y. Benhajali, C. Chu, F. Chouinard, A. Evans, A. Jakab, B. S. Khundrakpam, J. D. Lewis, Q. Li, M. Milham, et al. The neuro bureau preprocessing initiative: open sharing of preprocessed neuroimaging data and derivatives. *Frontiers in Neuroinformatics*, 7, 2013.

J. P. Cunningham, V. Gilja, S. I. Ryu, and K. V. Shenoy. Methods for estimating neural firing rates, and their application to brain–machine interfaces. *Neural Networks*, 22(9):1235–1246, 2009.

R. Dahlhaus. Locally stationary processes. In *Handbook of Statistics*, volume 30, pages 351–413. Elsevier, 2012.

C. De Boor, C. De Boor, E.-U. Mathématicien, C. De Boor, and C. De Boor. *A Practical Guide to Splines: Revised Edition*, volume 27. springer-verlag New York, 2001.

B. Deen, K. A. Pelphrey, and N. B. Pitskel. Three Systems of Insular Functional Connectivity Identified with Cluster Analysis. *Cerebral Cortex*, 21(7), 2010. doi: 10.1093/cercor/bhq186.

S. Deepaisarn, P. D. Tar, N. A. Thacker, A. Seepujak, and A. McMahon. Quantifying biological samples using linear poisson independent component analysis for maldi-tof mass spectra. *Bioinformatics*, 34(6):1001–1008, 2018.

T. Deneux, A. Kaszas, G. Szalay, G. Katona, T. Lakner, A. Grinvald, B. Rózsa, and I. Vanzetta. Accurate spike estimation from noisy calcium signals for ultrafast three-dimensional imaging of large neuronal populations in vivo. *Nature communications*, 7(1):1–17, 2016.

A. Di Martino, D. Oconnor, B. Chen, K. Alaerts, J. S. Anderson, M. Assaf, J. H. Balsters, L. Baxter, A. Beggiato, S. Bernaerts, et al. Enhancing studies of the connectome in autism using the autism brain imaging data exchange ii. *Scientific data*, 4(1):1–15, 2017.

Y. Du, G. D. Pearlson, D. Lin, J. Sui, J. Chen, M. Salman, C. A. Tamminga, E. I. Ivleva, J. A. Sweeney, M. S. Keshavan, et al. Identifying dynamic functional connectivity biomarkers using gig-ica: Application to schizophrenia, schizoaffective disorder, and psychotic bipolar disorder. *Human brain mapping*, 38(5):2683–2708, 2017.

K. Dzhaparidze. *Parameter Estimation and Hypothesis Testing in Spectral Analysis of Stationary Time Series*. Springer Science & Business Media, 1986.

S. B. Erdoğan, Y. Tong, L. M. Hocke, K. P. Lindsey, and B. deB Frederick. Correcting for blood arrival time in global mean regression enhances functional connectivity analysis of resting state fmri-bold signals. *Frontiers in human neuroscience*, 10:311, 2016.

H. Eryilmaz, D. Van De Ville, S. Schwartz, and P. Vuilleumier. Impact of transient emotions on functional connectivity during subsequent resting state: a wavelet correlation approach. *Neuroimage*, 54(3):2481–2491, 2011.

C. Euán, Y. Sun, H. Ombao, et al. Coherence-based time series clustering for statistical inference and visualization of brain connectivity. *Annals of Applied Statistics*, 13(2):990–1015, 2019.

M. Fox and M. Raichle. Spontaneous fluctuations in brain activity observed with functional magnetic resonance imaging. *Nature Reviews Neuroscience*, 8, 2007. doi: 10.1038/nrn2201.

M. D. Fox and M. Greicius. Clinical applications of resting state functional connectivity. *Frontiers in Systems Neuroscience*, 4:19, 2010.

P. Fransson, B. Skiöld, M. Engström, B. Hallberg, M. Mosskin, U. Åden, H. Lagercrantz, and M. Blennow. Spontaneous brain activity in the newborn brain during natural sleepan fmri study in infants born at full term. *Pediatric research*, 66(3):301–305, 2009.

K. J. Friston. Functional and effective connectivity in neuroimaging: a synthesis. *Human Brain Mapping*, 2(1-2):56–78, 1994.

K. J. Friston, S. Williams, R. Howard, R. S. Frackowiak, and R. Turner. Movement-related effects in fmri time-series. *Magnetic Resonance in Medicine*, 35(3):346–355, 1996.

K. J. Friston, L. Harrison, and W. Penny. Dynamic causal modelling. *Neuroimage*, 19(4):1273–1302, 2003.

K. J. Friston, J. Kahan, B. Biswal, and A. Razi. A dcm for resting state fmri. *Neuroimage*, 94: 396–407, 2014.

W. A. Gardner. A unifying view of coherence in signal processing. *Signal Processing*, 29(2): 113–140, 1992.

W. Gerstner and W. M. Kistler. *Spiking Neuron Models: Single Neurons, Populations, Plasticity*. Cambridge University Press, 2002.

A. S. Ghuman, J. R. McDaniel, and A. Martin. A wavelet-based method for measuring the oscillatory dynamics of resting-state functional connectivity in meg. *Neuroimage*, 56(1): 69–77, 2011.

K. Glomb, A. Ponce-Alvarez, M. Gilson, P. Ritter, and G. Deco. Resting state networks in empirical and simulated dynamic functional connectivity. *Neuroimage*, 159:388–402, 2017.

C. Gold, A. Holub, and P. Sollich. Bayesian approach to feature selection and parameter tuning for support vector machine classifiers. *Neural Networks*, 18(5-6):693–701, 2005.

E. M. Gordon, T. O. Laumann, A. W. Gilmore, D. J. Newbold, D. J. Greene, J. J. Berg, M. Ortega, C. Hoyt-Drazen, C. Gratton, H. Sun, et al. Precision functional mapping of individual human brains. *Neuron*, 95(4):791–807, 2017.

E. M. Gordon, T. O. Laumann, A. W. Gilmore, D. J. Newbold, D. J. Greene, J. J. Berg, M. Ortega, C. Hoyt-Drazen, C. Gratton, H. Sun, J. M. Hampton, R. S. Coalson, A. Nguyen, K. B. McDermott, J. S. Shimony, A. Z. Snyder, B. L. Schlaggar, S. E. Petersen, S. M. Nelson, and N. U. Dosenbach. The Midnight Scan Club (MSC) dataset, 2020.

C. W. Granger. Investigating causal relations by econometric models and cross-spectral methods. *Econometrica: Journal of the Econometric Society*, pages 424–438, 1969.

M. D. Greicius, K. Supekar, V. Menon, and R. F. Dougherty. Resting-state functional connectivity reflects structural connectivity in the default mode network. *Cerebral Cortex*, 19(1):72–78, 2009.

B. F. Grewe, D. Langer, H. Kasper, B. M. Kampa, and F. Helmchen. High-speed in vivo calcium imaging reveals neuronal network activity with near-millisecond precision. *Nature Methods*, 7(5):399, 2010.

L. Griffanti, G. Salimi-Khorshidi, C. F. Beckmann, E. J. Auerbach, G. Douaud, C. E. Sexton, E. Zsoldos, K. P. Ebmeier, N. Filippini, C. E. Mackay, et al. Ica-based artefact removal and accelerated fmri acquisition for improved resting state network imaging. *Neuroimage*, 95: 232–247, 2014.

L. Griffanti, M. Rolinski, K. Szewczyk-Krolikowski, R. A. Menke, N. Filippini, G. Zamboni, M. Jenkinson, M. T. Hu, and C. E. Mackay. Challenges in the reproducibility of clinical studies with resting state fmri: An example in early parkinson's disease. *Neuroimage*, 124: 704–713, 2016.

J. Guàrdia-Olmos, M. Peró-Cebollero, and E. Gudayol-Ferré. Meta-analysis of the structural equation models' parameters for the estimation of brain connectivity with fmri. *Frontiers in Behavioral Neuroscience*, 12:19, 2018.

T. Hastie and R. Tibshirani. Independent components analysis through product density estimation. *Advances in neural information processing systems*, 15:665–672, 2002.

B. He, L. Yang, C. Wilke, and H. Yuan. Electrophysiological imaging of brain activity and connectivitychallenges and opportunities. *IEEE Transactions on Biomedical Engineering*, 58 (7):1918–1931, 2011.

C. J. Honey, O. Sporns, L. Cammoun, X. Gigandet, J.-P. Thiran, R. Meuli, and P. Hagmann. Predicting human resting-state functional connectivity from structural connectivity. *Proceedings of the National Academy of Sciences*, 106(6):2035–2040, 2009.

Z. Hong and H. Lian. Sparse-smooth regularized singular value decomposition. *Journal of Multivariate Analysis*, 117:163–174, 2013.

R. M. Hutchison, T. Womelsdorf, E. A. Allen, P. A. Bandettini, V. D. Calhoun, M. Corbetta, S. Della Penna, J. H. Duyn, G. H. Glover, J. Gonzalez-Castillo, et al. Dynamic functional connectivity: promise, issues, and interpretations. *Neuroimage*, 80:360–378, 2013.

A. Hyvärinen and E. Oja. A fast fixed-point algorithm for independent component analysis. *Neural Comput.*, 9(7), 1997. doi: 10.1162/neco.1997.9.7.1483.

A. Hyvärinen and E. Oja. Independent component analysis: algorithms and applications. *Neural Networks*, 13(4-5):411–430, 2000.

M. Jenkinson, C. F. Beckmann, T. E. Behrens, M. W. Woolrich, and S. M. Smith. FSL. *Neuroimage*, 62(2):782–790, 2012.

S. W. Jewell, T. D. Hocking, P. Fearnhead, and D. M. Witten. Fast nonconvex deconvolution of calcium imaging data. *Biostatistics*, 21(4):709–726, 2020.

S. Joel, B. S Caffo, P. van zijl, and J. J Pekar. On the relationship between seed-based and ica-based measures of functional connectivity. *Magnetic resonance in medicine : official journal of the Society of Magnetic Resonance in Medicine / Society of Magnetic Resonance in Medicine*, 66, 2011. doi: 10.1002/mrm.22818.

T. Johnstone, K. S. Ores Walsh, L. L. Greischar, A. L. Alexander, A. S. Fox, R. J. Davidson, and T. R. Oakes. Motion correction and the use of motion covariates in multiple-subject fmri analysis. *Human Brain Mapping*, 27(10):779–788, 2006.

M. Kaiser. A tutorial in connectome analysis: topological and spatial features of brain networks. *Neuroimage*, 57(3):892–907, 2011.

J. W. Kalat. *Biological Psychology*. Nelson Education, 2015.

A. Kazeminejad and R. C. Sotero. Topological properties of resting-state fmri functional networks improve machine learning-based autism classification. *Frontiers in neuroscience*, 12:1018, 2019.

V. Kiviniemi, T. Vire, J. Remes, A. A. Elseoud, T. Starck, O. Tervonen, and J. Nikkinen. A sliding time-window ica reveals spatial variability of the default mode network in time. *Brain Connectivity*, 1(4):339–347, 2011.

C. Kooperberg, C. J. Stone, and Y. K. Truong. Hazard regression. *Journal of the American Statistical Association*, 90(429):78–94, 1995.

Y. Koush, M. J. Rosa, F. Robineau, K. Heinen, S. W. Rieger, N. Weiskopf, P. Vuilleumier, D. Van De Ville, and F. Scharnowski. Connectivity-based neurofeedback: dynamic causal modeling for real-time fmri. *Neuroimage*, 81:422–430, 2013.

S. LaConte, J. Anderson, S. Muley, J. Ashe, S. Frutiger, K. Rehm, L. K. Hansen, E. Yacoub, X. Hu, D. Rottenberg, et al. The evaluation of preprocessing choices in single-subject bold fmri using npairs performance metrics. *Neuroimage*, 18(1):10–27, 2003.

H.-L. Lee, B. Zahneisen, T. Hugger, P. LeVan, and J. Hennig. Tracking dynamic resting-state networks at higher frequencies using mr-encephalography. *Neuroimage*, 65:216–222, 2013a.

M. Lee, H. Shen, J. Z. Huang, and J. Marron. Biclustering via sparse singular value decomposition. *Biometrics*, 66(4):1087–1095, 2010.

M. H. Lee, C. D. Smyser, and J. S. Shimony. Resting-state fmri: a review of methods and clinical applications. *American Journal of neuroradiology*, 34(10):1866–1872, 2013b.

S. Lee, H. Shen, Y. Truong, M. Lewis, and X. Huang. Independent component analysis involving autocorrelated sources with an application to functional magnetic resonance imaging. *Journal of the American Statistical Association*, 106, 2011. doi: 10.1198/jasa.2011.tm10332.

C. Leibig, T. Wachtler, and G. Zeck. Unsupervised neural spike sorting for high-density microelectrode arrays with convolutive independent component analysis. *Journal of Neuroscience Methods*, 271:1–13, 2016.

N. Leonardi, J. Richiardi, M. Gschwind, S. Simioni, J.-M. Annoni, M. Schluep, P. Vuilleumier, and D. V. D. Ville. Principal components of functional connectivity: A new approach to study dynamic brain connectivity during rest. *Neuroimage*, 83, 2013. doi: https://doi.org/10.1016/j.neuroimage.2013.07.019.

G. Li, D. Yang, A. B. Nobel, and H. Shen. Supervised singular value decomposition and its asymptotic properties. *Journal of Multivariate Analysis*, 146:7–17, 2016.

Z. Lin, P. J. Kahrilas, Y. Xiao, F. Nicodème, N. Gonsalves, I. Hirano, and J. E. Pandolfino. Functional luminal imaging probe topography: an improved method for characterizing esophageal distensibility in eosinophilic esophagitis. *Therapeutic Advances in Gastroenterology*, 6(2):97–107, 2013.

M. A. Lindquist, Y. Xu, M. B. Nebel, and B. S. Caffo. Evaluating dynamic bivariate correlations in resting-state fmri: a comparison study and a new approach. *Neuroimage*, 101:531–546, 2014.

H. Liu, Z. Wu, X. Li, D. Cai, and T. S. Huang. Constrained nonnegative matrix factorization for image representation. *IEEE Transactions on Pattern Analysis and Machine Intelligence*, 34 (7):1299–1311, 2011.

X. Liu, X.-H. Zhu, P. Qiu, and W. Chen. A correlation-matrix-based hierarchical clustering method for functional connectivity analysis. *Journal of Neuroscience Methods*, 211(1):94–102, 2012.

P. K. Mandal, A. Banerjee, M. Tripathi, and A. Sharma. A comprehensive review of magnetoencephalography (meg) studies for brain functionality in healthy aging and alzheimer's disease (ad). *Frontiers in Computational Neuroscience*, 12:60, 2018.

G. Marrelec and P. Fransson. Assessing the influence of different roi selection strategies on functional connectivity analyses of fmri data acquired during steady-state conditions. *PloS one*, 6(4):e14788, 2011.

H. A. Marusak, V. D. Calhoun, S. Brown, L. M. Crespo, K. Sala-Hamrick, I. H. Gotlib, and M. E. Thomason. Dynamic functional connectivity of neurocognitive networks in children. *Human Brain Mapping*, 38(1), 2017.

R. Maruyama, K. Maeda, H. Moroda, I. Kato, M. Inoue, H. Miyakawa, and T. Aonishi. Detecting cells using non-negative matrix factorization on calcium imaging data. *Neural Networks*, 55: 11–19, 2014.

A. Mclntosh and F. Gonzalez-Lima. Structural equation modeling and its application to network analysis in functional brain imaging. *Human Brain Mapping*, 2(1-2):2–22, 1994.

R. J. Meszlényi, K. Buza, and Z. Vidnyánszky. Resting state fmri functional connectivity-based classification using a convolutional neural network architecture. *Frontiers in neuroinformatics*, 11:61, 2017a.

R. J. Meszlényi, P. Hermann, K. Buza, V. Gál, and Z. Vidnyánszky. Resting state fmri functional connectivity analysis using dynamic time warping. *Frontiers in neuroscience*, 11:75, 2017b.

W. Mittmann, D. J. Wallace, U. Czubayko, J. T. Herb, A. T. Schaefer, L. L. Looger, W. Denk, and J. N. Kerr. Two-photon calcium imaging of evoked activity from l5 somatosensory neurons in vivo. *Nature Neuroscience*, 14(8):1089–1093, 2011.

R. Mohanty, W. A. Sethares, V. A. Nair, and V. Prabhakaran. Rethinking measures of functional connectivity via feature extraction. *Scientific reports*, 10(1):1–17, 2020.

E. A. Mukamel, A. Nimmerjahn, and M. J. Schnitzer. Automated analysis of cellular signals from large-scale calcium imaging data. *Neuron*, 63(6):747–760, 2009.

K. Murphy and M. D. Fox. Towards a consensus regarding global signal regression for resting state functional connectivity mri. *Neuroimage*, 154:169–173, 2017.

K. Murphy, R. M. Birn, and P. A. Bandettini. Resting-state fmri confounds and cleanup. *Neuroimage*, 80:349–359, 2013.

J. Muschelli, M. B. Nebel, B. S. Caffo, A. D. Barber, J. J. Pekar, and S. H. Mostofsky. Reduction of motion-related artifacts in resting state fmri using acompcor. *Neuroimage*, 96:22–35, 2014.

J.-J. Paakki, J. Rahko, X. Long, I. Moilanen, O. Tervonen, J. Nikkinen, T. Starck, J. Remes, T. Hurtig, H. Haapsamo, et al. Alterations in regional homogeneity of resting-state brain activity in autism spectrum disorders. *Brain research*, 1321:169–179, 2010.

L. Parkes, B. Fulcher, M. Yücel, and A. Fornito. An evaluation of the efficacy, reliability, and sensitivity of motion correction strategies for resting-state functional mri. *Neuroimage*, 171: 415–436, 2018.

T. B. Parrish, D. R. Gitelman, K. S. LaBar, and M.-M. Mesulam. Impact of signal-to-noise on functional mri. *Magnetic Resonance in Medicine*, 44(6):925–932, 2000.

A. X. Patel, P. Kundu, M. Rubinov, P. S. Jones, P. E. Vértes, K. D. Ersche, J. Suckling, and E. T. Bullmore. A wavelet method for modeling and despiking motion artifacts from resting-state fmri time series. *Neuroimage*, 95:287–304, 2014.

K. M. Petersson, T. E. Nichols, J.-B. Poline, and A. P. Holmes. Statistical limitations in functional neuroimaging ii. signal detection and statistical inference. *Philosophical Transactions of the Royal Society of London. Series B: Biological Sciences*, 354(1387):1261–1281, 1999.

E. A. Pnevmatikakis, J. Merel, A. Pakman, and L. Paninski. Bayesian spike inference from calcium imaging data. In *2013 Asilomar Conference on Signals, Systems and Computers*, pages 349–353. IEEE, 2013.

E. A. Pnevmatikakis, D. Soudry, Y. Gao, T. A. Machado, J. Merel, D. Pfau, T. Reardon, Y. Mu, C. Lacefield, W. Yang, et al. Simultaneous denoising, deconvolution, and demixing of calcium imaging data. *Neuron*, 89(2):285–299, 2016.

J. D. Power, K. A. Barnes, A. Z. Snyder, B. L. Schlaggar, and S. E. Petersen. Spurious but systematic correlations in functional connectivity mri networks arise from subject motion. *Neuroimage*, 59(3):2142–2154, 2012.

R. H. Pruim, M. Mennes, D. van Rooij, A. Llera, J. K. Buitelaar, and C. F. Beckmann. Ica-aroma: A robust ica-based strategy for removing motion artifacts from fmri data. *Neuroimage*, 112: 267–277, 2015.

D. P. Radunović. *Wavelets From Math to Practice*. Springer Berlin Heidelberg, 2009.

N. Ramnani, T. E. Behrens, W. Penny, and P. M. Matthews. New approaches for exploring anatomical and functional connectivity in the human brain. *Biological Psychiatry*, 56(9):613–619, 2004.

J. D. Ramsey, S. J. Hanson, C. Hanson, Y. O. Halchenko, R. A. Poldrack, and C. Glymour. Six problems for causal inference from fmri. *Neuroimage*, 49(2):1545–1558, 2010.

B. Rashid, M. R. Arbabshirani, E. Damaraju, M. S. Cetin, R. Miller, G. D. Pearlson, and V. D. Calhoun. Classification of schizophrenia and bipolar patients using static and dynamic resting-state fmri brain connectivity. *Neuroimage*, 134:645–657, 2016.

S. L. Resendez, V. M. K. Namboodiri, J. M. Otis, L. E. Eckman, J. Rodriguez-Romaguera, R. L. Ung, M. L. Basiri, O. Kosyk, M. A. Rossi, G. S. Dichter, et al. Social stimuli induce activation of oxytocin neurons within the paraventricular nucleus of the hypothalamus to promote social behavior in male mice. *Journal of Neuroscience*, 40(11):2282–2295, 2020.

P. Reynaud-Bouret, V. Rivoirard, F. Grammont, and C. Tuleau-Malot. Goodness-of-fit tests and nonparametric adaptive estimation for spike train analysis. *The Journal of Mathematical Neuroscience*, 4(1):3, 2014.

F. Rieke, D. Warland, R. D. R. Van Steveninck, W. S. Bialek, et al. *Spikes: Exploring the Neural Code*, volume 7. MIT Press Cambridge, 1999.

J. Rodriguez-Romaguera, R. Ung, H. Nomura, J. Otis, M. Basiri, V. Namboodiri, X. Zhu, E. Robinson, J. McHenry, O. Kosyk, et al. Prepronociceptin expressing neurons in the extended amygdala encode and promote rapid arousal responses to motivationally salient stimuli. *bioRxiv*, 2020.

B. P. Rogers, V. L. Morgan, A. T. Newton, and J. C. Gore. Assessing functional connectivity in the human brain by fmri. *Magnetic Resonance Imaging*, 25(10), 2007. doi: https://doi.org/10.1016/j.mri.2007.03.007.

I. Romero. Pca and ica applied to noise reduction in multi-lead ecg. In *2011 Computing in Cardiology*, pages 613–616. IEEE, 2011.

A. K. Roy, Z. Shehzad, D. S. Margulies, A. C. Kelly, L. Q. Uddin, K. Gotimer, B. B. Biswal, F. X. Castellanos, and M. P. Milham. Functional connectivity of the human amygdala using resting state fmri. *Neuroimage*, 45(2):614–626, 2009.

M. Rubinov and O. Sporns. Complex network measures of brain connectivity: uses and interpretations. *Neuroimage*, 52(3):1059–1069, 2010.

T. D. Satterthwaite, M. A. Elliott, R. T. Gerraty, K. Ruparel, J. Loughead, M. E. Calkins, S. B. Eickhoff, H. Hakonarson, R. C. Gur, R. E. Gur, et al. An improved framework for confound regression and filtering for control of motion artifact in the preprocessing of resting-state functional connectivity data. *Neuroimage*, 64:240–256, 2013.

C. Savin, P. Joshi, and J. Triesch. Independent component analysis in spiking neurons. *PLoS Computational Biology*, 6(4):e1000757, 2010.

B. Sengupta, S. B. Laughlin, and J. E. Niven. Consequences of converting graded to action potentials upon neural information coding and energy efficiency. *PLoS Computational Biology*, 10(1):e1003439, 2014.

A. K. Seth, A. B. Barrett, and L. Barnett. Granger causality analysis in neuroscience and neuroimaging. *Journal of Neuroscience*, 35(8):3293–3297, 2015.

S. Shakil, C.-H. Lee, and S. D. Keilholz. Evaluation of sliding window correlation performance for characterizing dynamic functional connectivity and brain states. *Neuroimage*, 133:111–128, 2016.

Y. I. Sheline and M. E. Raichle. Resting state functional connectivity in preclinical alzheimers disease. *Biological psychiatry*, 74(5):340–347, 2013.

H. Shen. Independent component analysis for spatial stochastic processes on a lattice. In *Joint Statistical Meeting*, 2015.

S. M. Smith, K. L. Miller, G. Salimi-Khorshidi, M. Webster, C. F. Beckmann, T. E. Nichols, J. D. Ramsey, and M. W. Woolrich. Network modelling methods for fmri. *Neuroimage*, 54(2): 875–891, 2011.

S. M. Smith, A. Hyvärinen, G. Varoquaux, K. L. Miller, and C. F. Beckmann. Group-pca for very large fmri datasets. *Neuroimage*, 101:738–749, 2014.

W. Sohn, K. Yoo, Y.-B. Lee, S. Seo, D. Na, and Y. Jeong. Influence of roi selection on resting state functional connectivity: an individualized approach for resting state fmri analysis. *Frontiers in Neuroscience*, 9, 2015. doi: 10.3389/fnins.2015.00280.

R. Srinivasan, W. R. Winter, J. Ding, and P. L. Nunez. Eeg and meg coherence: measures of functional connectivity at distinct spatial scales of neocortical dynamics. *Journal of Neuroscience Methods*, 166(1):41–52, 2007.

C. Sripada, S. Rutherford, M. Angstadt, W. K. Thompson, M. Luciana, A. Weigard, L. H. Hyde, and M. Heitzeg. Prediction of neurocognition in youth from resting state fmri. *Molecular psychiatry*, pages 1–9, 2019.

C. Stam. Brain dynamics in theta and alpha frequency bands and working memory performance in humans. *Neuroscience Letters*, 286(2):115–118, 2000.

C. Stosiek, O. Garaschuk, K. Holthoff, and A. Konnerth. In vivo two-photon calcium imaging of neuronal networks. *Proceedings of the National Academy of Sciences*, 100(12):7319–7324, 2003.

S. P. Strong, R. Koberle, R. R. D. R. Van Steveninck, and W. Bialek. Entropy and information in neural spike trains. *Physical Review Letters*, 80(1):197, 1998.

F. T. Sun, L. M. Miller, and M. D'Esposito. Measuring interregional functional connectivity using coherence and partial coherence analyses of fmri data. *Neuroimage*, 21(2):647–658, 2004.

D. Sundararajan. *The Discrete Fourier Transform: Theory, Algorithms and Applications*. World Scientific, 2001.

L. Theis, P. Berens, E. Froudarakis, J. Reimer, M. R. Rosón, T. Baden, T. Euler, A. Tolias, and M. Bethge. Supervised learning sets benchmark for robust spike detection from calcium imaging signals. *arXiv preprint arXiv:1503.00135*, 2015.

E. Tibau, M. Valencia, and J. Soriano. Identification of neuronal network properties from the spectral analysis of calcium imaging signals in neuronal cultures. *Frontiers in Neural Circuits*, 7:199, 2013.

C. Triantafyllou, R. D. Hoge, and L. L. Wald. Effect of spatial smoothing on physiological noise in high-resolution fmri. *Neuroimage*, 32(2):551–557, 2006.

Y. K. Truong and M. M. Lewis. *Statistical Techniques for Neuroscientists*. CRC Press, 2016.

V. G. van de Ven, E. Formisano, D. Prvulovic, C. H. Roeder, and D. E. Linden. Functional connectivity as revealed by spatial independent component analysis of fmri measurements during rest. *Human Brain Mapping*, 22(3), 2004. doi: 10.1002/hbm.20022.

M. van den Heuvel, C. Stam, M. Boersma, and H. H. Pol. Small-world and scale-free organization of voxel-based resting-state functional connectivity in the human brain. *Neuroimage*, 43(3), 2008. doi: https://doi.org/10.1016/j.neuroimage.2008.08.010.

M. P. van den Heuvel and H. E. H. Pol. Exploring the brain network: A review on resting-state fmri functional connectivity. *European Neuropsychopharmacology*, 20(8), 2010. doi: https://doi.org/10.1016/j.euroneuro.2010.03.008.

B. D. Van Veen, W. Van Drongelen, M. Yuchtman, and A. Suzuki. Localization of brain electrical activity via linearly constrained minimum variance spatial filtering. *IEEE Transactions on Biomedical Engineering*, 44(9):867–880, 1997.

J. T. Vogelstein, B. O. Watson, A. M. Packer, R. Yuste, B. Jedynak, and L. Paninski. Spike inference from calcium imaging using sequential monte carlo methods. *Biophysical Journal*, 97 (2):636–655, 2009.

J. Wang, X. Zuo, and Y. He. Graph-based network analysis of resting-state functional mri. *Frontiers in Systems Neuroscience*, 4, 2010. doi: 10.3389/fnsys.2010.00016.

J. W. Wang, A. M. Wong, J. Flores, L. B. Vosshall, and R. Axel. Two-photon calcium imaging reveals an odor-evoked map of activity in the fly brain. *Cell*, 112(2):271–282, 2003.

R. Warnick, M. Guindani, E. Erhardt, E. Allen, V. Calhoun, and M. Vannucci. A bayesian approach for estimating dynamic functional network connectivity in fmri data. *Journal of the American Statistical Association*, 113(521), 2018. doi: 10.1080/01621459.2017.1379404.

A. Weissenbacher, C. Kasess, F. Gerstl, R. Lanzenberger, E. Moser, and C. Windischberger. Correlations and anticorrelations in resting-state functional connectivity mri: a quantitative comparison of preprocessing strategies. *Neuroimage*, 47(4):1408–1416, 2009.

M. Welvaert and Y. Rosseel. On the definition of signal-to-noise ratio and contrast-to-noise ratio for fmri data. *PloS One*, 8(11):e77089, 2013.

P. Whittle. *Hypothesis Testing in Time Series Analysis*, volume 4. Almqvist & Wiksells boktr., 1951.

K. J. Worsley, J.-I. Chen, J. Lerch, and A. C. Evans. Comparing functional connectivity via thresholding correlations and singular value decomposition. *Philosophical Transactions of the Royal Society B: Biological Sciences*, 360(1457):913–920, 2005.

C. W. Wu, H. Gu, H. Lu, E. A. Stein, J.-H. Chen, and Y. Yang. Frequency specificity of functional connectivity in brain networks. *Neuroimage*, 42(3):1047–1055, 2008.

S.-y. Xie, R. Guo, N.-f. Li, G. Wang, and H.-t. Zhao. Brain fmri processing and classification based on combination of pca and svm. In *2009 International Joint Conference on Neural Networks*, pages 3384–3389. IEEE, 2009.

Y. Xu and M. Lindquist. Dynamic connectivity detection: an algorithm for determining functional connectivity change points in fmri data. *Frontiers in Neuroscience*, 9, 2015. doi: 10.3389/fnins.2015.00285.

Z. Xue, J. Li, S. Li, and B. Wan. Using ica to remove eye blink and power line artifacts in eeg. In *First International Conference on Innovative Computing, Information and Control-Volume I (ICICIC'06)*, volume 3, pages 107–110. IEEE, 2006.

W. Yan, D. Rangaprakash, and G. Deshpande. Aberrant hemodynamic responses in autism: implications for resting state fmri functional connectivity studies. *NeuroImage: Clinical*, 19: 320–330, 2018.

P. Zanini, H. Shen, Y. Truong, et al. Understanding resident mobility in milan through independent component analysis of telecom italia mobile usage data. *Annals of Applied Statistics*, 10(2): 812–833, 2016.

L. Zhang, H. Shen, and J. Z. Huang. Robust regularized singular value decomposition with application to mortality data. *The Annals of Applied Statistics*, pages 1540–1561, 2013.

Y. Zhong, H. Wang, G. Lu, Z. Zhang, Q. Jiao, and Y. Liu. Detecting functional connectivity in fmri using pca and regression analysis. *Brain Topography*, 22, 2009. doi: 10.1007/s10548-009-0095-4.